



TECHNISCHE UNIVERSITÄT
CHEMNITZ

Medical Imaging of Magnetic Micromotors Through Scattering Tissues

der Fakultät für Naturwissenschaften der
Technischen Universität Chemnitz
genehmigte

Dissertation

zur Erlangung des akademischen Grades

doctor rerum naturalium

(Dr. rer. nat.)

vorgelegt

von: M.Sc. Azaam Aziz
geboren am: 10. Dezember 1988 in Gujrat, Pakistan
Tag der Einreichung: 14. August 2020

Gutachter: Prof. Dr. Oliver G. Schmidt
Prof. Dr.-Ing. habil. Jürgen W. Czarske

Tag der Verteidigung 11. Dezember 2020

The results presented in this thesis have been performed at the Institute for Integrative Nanosciences (IIN) at the Leibniz Institute for Solid State and Materials Research (IFW) Dresden, iThera Medical Munich and VisualSonics Amsterdam between 09/2016 and 03/2020.

Parts of this thesis have been published in the following peer reviewed journal articles, conference proceedings and online pre-print version (bioRxiv). Reprinted figures are copyrighted by the respective publisher as indicated and reuse is in accordance with the author rights granted in the Copyright Transfer Agreements.

A. Aziz, M. Medina-Sánchez, J. Claussen, and O. G. Schmidt, “Real-Time Optoacoustic Tracking of Single Moving Micro-objects in Deep Phantom and Ex Vivo Tissues” **Nano Lett.**, 19 (9), 6612–6620, 2019.

A. Aziz, M. Medina-Sánchez, N. Koukourakis, J. Wang, R. Kuschmierz, H. Radner, J. W. Czarske and O. G. Schmidt, “Real-time IR tracking of single reflective micromotors through scattering tissues” **Adv. Funct. Mater.**, 29 (51) 2019.

A. Aziz, M. Medina-Sánchez, J. Claussen, and O. G. Schmidt, “Optoacoustic detection of 3D microstructures in deep tissue-mimicking phantoms” Int. Conf. Manip. Autom. Robot. Small Scales (MARSS), July 1-5, 2019, Helsinki/Finland, 2019.

A. Aziz, S. Pane, V. Iacovacci, N. Koukourakis, J. W. Czarske, A. Menciassi, M. Medina-Sánchez and O. G. Schmidt, “Medical Imaging of Microrobots: Toward In Vivo Applications” **ACS Nano**, 14 (9), 10865-10893, 2020.

A. Aziz, J. Holthof, S. Meyer, O. G. Schmidt, M. Medina-Sánchez, “In Vivo Imaging of Swimming Micromotors Using Hybrid High-Frequency Ultrasound and Photoacoustic Imaging” **bioRxiv**, 2020. doi: 10.1101/2020.06.15.148791.

Bibliographic Record

Aziz, Azaam

Medical Imaging of Magnetic Micromotors Through Scattering Tissues

Dissertation, 2020

116 pages, 49 figures, 242 citations

ABSTRACT

Micro- and nanorobots (MNRs) are small autonomous devices capable of performing complex tasks and have been demonstrated for a variety of non-invasive biomedical applications, such as tissue engineering, drug delivery or assisted fertilization. However, translating such approaches to an *in vivo* environment is critical. Current imaging techniques do not allow localization and tracking of single or few micromotors at high spatiotemporal resolution in deep tissue.

This thesis addresses some of these limitations, by exploring the use of two optical-based techniques (IR and photoacoustic imaging (PAI)) and a combination of both US and PAI. First, we employ an IR imaging setup to visualize mobile reflective micromotors under scattering phantoms and *ex vivo* mouse skull tissues, without using any labels. The reflective micromotor reflects more than tenfold the light intensity of a simple particle. However, the achieved penetration depth was ca. 100 μm (when using *ex vivo* tissues), limiting this technique to superficial biomedical applications. In this regard, PAI plays a role that combines the advantages of US such as penetration depth and real-time imaging with the molecular specificity of optics. For the first time, in this thesis, this method is evaluated for dynamic process monitoring, in particular for tracking single micromotor in real-time below ~ 1 cm deep phantom and *ex vivo* tissue.

However, the precise function control of MNRs in living organisms, demand the combination of both anatomical and functional imaging methods. Therefore, in the end, we report the use of a hybrid US and PA system for the real-time tracking of magnetically driven micromotors (single and swarms) in phantoms, *ex vivo*, and *in vivo* (in mice bladder and uterus), envisioning their application for targeted drug-delivery. This achievement is of great importance and opens the possibilities to employ medical micromotors in a living organism and perform a medical task while being externally controlled and monitored.

KEYWORDS: medical imaging, micromotor, real-time tracking, hybrid imaging, deep tissue, *in vivo* imaging, microrobotics, photoacoustics, ultrasound

Table of Contents

ABSTRACT	1
1 INTRODUCTION.....	5
1.1 Motivation.....	5
1.2 Background	7
1.2.1 Microrobotics.....	7
1.2.2 Medical Imaging.....	9
1.3 Objectives and Structure of Thesis	12
2 FUNDAMENTALS.....	15
2.1 Optical Imaging.....	15
2.1.1. Reflection-based Imaging	17
2.1.2. Fluorescence-based Imaging	18
2.1.1 Light-Tissue Interaction	20
2.2 Photoacoustic Imaging.....	23
2.2.1 Theory	23
2.2.2 Implementation	25
2.3 Ultrasound Imaging.....	26
2.3.1 Theory	26
2.3.2 Implementation	28
3 MATERIALS AND METHODS.....	30
3.1 Fabrication of Magnetic Micropropellers	30
3.1.1 3D Laser Lithography of Polymeric Resin	30
3.1.2 Self-assembly of SiO ₂ Particles	31
3.1.3 Electron Beam Evaporation.....	32
3.1.4 Surface Functionalization	33
3.2 Fabrication of Phantom Tissue and Microfluidic Channels	34
3.2.1 Fabrication of PDMS-Glycerol Phantom.....	34
3.2.2 Fabrication of Agarose Phantom.....	35
3.2.3 Phantom based on <i>Ex vivo</i> Tissues (Chicken Breast and Mice Skull)....	36
3.2.4 Microfluidic Channel Platform.....	37
3.3 Sample Characterization	38
3.3.1 Optical Microscopy	38
3.3.2 Scanning Electron Microscopy	38
3.4 Magnetic Actuation	39
3.4.1 Magnetic Force	39
3.4.2 Magnetic Torque	39
3.5 Ethic Statement for Mice Experiments.....	41

4	OPTICAL IMAGING OF MICROROBOTS	42
4.1	Concept of Reflective Micromotors	42
4.2	Fabrication of Reflective Micromotors	44
4.3	IR Imaging Actuation Setup	45
4.4	Actuation and Propulsion Performance below Phantom	47
4.5	Actuation and Propulsion Performance below <i>Ex Vivo</i> Skull Tissue	50
4.6	Actuation and Propulsion Performance in Blood	51
5	PHOTOACOUSTIC IMAGING OF MICROROBOTS	55
5.1	Absorbers for Deep Tissue Imaging	55
5.2	Absorber Micromotor Design and Fabrication	56
5.3	Photoacoustic Imaging Setup	58
5.4	Actuation Performance below Phantom Tissue	60
5.5	Actuation Performance below <i>Ex Vivo</i> Tissue	65
6	HYBRID ULTRASOUND AND PHOTOACOUSTIC IMAGING	67
6.1	Hybrid Ultrasound/Photoacoustic System	68
6.2	Fabrication and Characterization of Micromotors	69
6.3	Actuation and Propulsion Performance below Phantom	69
6.4	Actuation and Propulsion Performance below <i>Ex Vivo</i> Tissues	71
6.5	Actuation and Propulsion Performance in Mice	72
6.5.1	Swimming of Micromotors in Bladder	72
6.5.2	Actuation of Micromotors in Uterus	74
6.5.3	3D Multispectral Imaging	76
6.5.4	Towards Targeted Drug Delivery	77
7	SUMMARY AND PERSPECTIVES	80
7.1	Summary	80
7.2	Future Perspectives	83
7.2.1	Contrasts Enhancing Labels	84
7.2.2	Novel Imaging Concepts	85
8	REFERENCES	88
9	APPENDIX	105
	List of Figures	105
	List of Tables	107
	Abbreviations	108
	List of Publications	109
	Acknowledgements	110
	Selbstständigkeitserklärung	111
	Curriculum Vitae	112

1 INTRODUCTION

1.1 Motivation

The visionary idea by Richard Feynman¹ in 1959 from his classic lecture “There is a plenty of room at the bottom”, at the California Institute of Technology has fascinated humans since ever, where a tiny doctor moves inside the body to perform a surgery. He described a fantasy of his student Albert Hibbs that a patient should be able to “swallow the surgeon”. Later on, in 1966, this visionary concept of miniaturization inspired science fiction, with movies such as ‘Fantastic Voyage, 1966’, where a medical crew with a submarine is miniaturized so that it can navigate through the human blood vessel to repair brain damage.

To accomplish this ‘Dream idea’, scientists around the world have proposed and produced many types of microscopic devices that can be maneuvered and controlled inside the human body to aid doctors in identifying and treating diseases. The progress achieved over the last 15 years in engineered MNRs has certainly reached limits beyond those imagined and the wild idea is not considered science fiction anymore but instead becoming a reality.

To see the vision of miniaturization and bring this technology close to the clinic, a huge effort is being made by the microrobotics research community worldwide. Such tiny machines (rods, tubes, helices, or spheres) or more sophisticated ones as the recently reported electrobots² can be sent into the body (bloodstream, liver, stomach, or reproductive tract) to perform several functions like disease diagnosis, targeted drug delivery, biosensing or microsurgery. However, most of these applications have been carried out by the use of optical microscopy in *in vitro* conditions different from the human body, and translating such approaches to an *in vivo* environment is not straightforward. To translate this technology to humans and despite all the ethical discussions around the employment of medical microrobots that will arise in the next years, there are some technical limitations that need to be solved such as toxicity and material biodegradability.³ Several MNRs rely on toxic fuels (e.g. H_2O_2) and are not suitable for *in vivo* applications. For instance, MNRs powered by H_2O_2 are not suitable for human body due to its toxic nature. This issue can be addressed by using bodily fluids such as water, urea, glucose or gastric acid as fuels for chemical MNRs. Biodegradability and biocompatibility are other prerequisites related to the fabrication

of MNRs. It is necessary to develop MNRs based on biocompatible and biodegradable materials such as gelatin, magnesium, or alginate. There have been few attempts of biocompatible micromotors for *in vivo* drug-delivery applications.^{4,5} Furthermore, challenges of actuation or navigation of MNRs in complex biological media should also be tackled. At present, actuation is mainly carried out in *in vitro* settings, in fact, bodily fluids consist of proteins, lipids, or nucleic acids that can greatly influence the motion and navigation of MNRs in living body. In addition, MNRs also need to cross several biological barriers such as cell membrane, mucosal, blood-brain, vitreous humor, among others to perform biomedical functions. Therefore, to enter pre-clinical and clinical trials, MNRs must clear these hurdles and the most important requirement is to be able to monitor the function and motion of such MNRs in deep tissue. For that the use of medical imaging technique poses a significant challenge and holds several difficulties such as the small size of microrobots, the biocompatibility of available labels and high spatiotemporal resolution of employed technique in deep human body.

A wide plethora of medical imaging techniques are available, but the identification and the selection of the proper one to be employed strongly depend on the intended MNR application and working district. However, employing standard medical imaging techniques for microrobots localization is not trivial and many challenges still need to be faced in the attempt to identify the best compromise between spatiotemporal resolution, field of view (FoV), penetration depth, complexity and level of invasiveness associated with the imaging technique **Figure 1.1.**

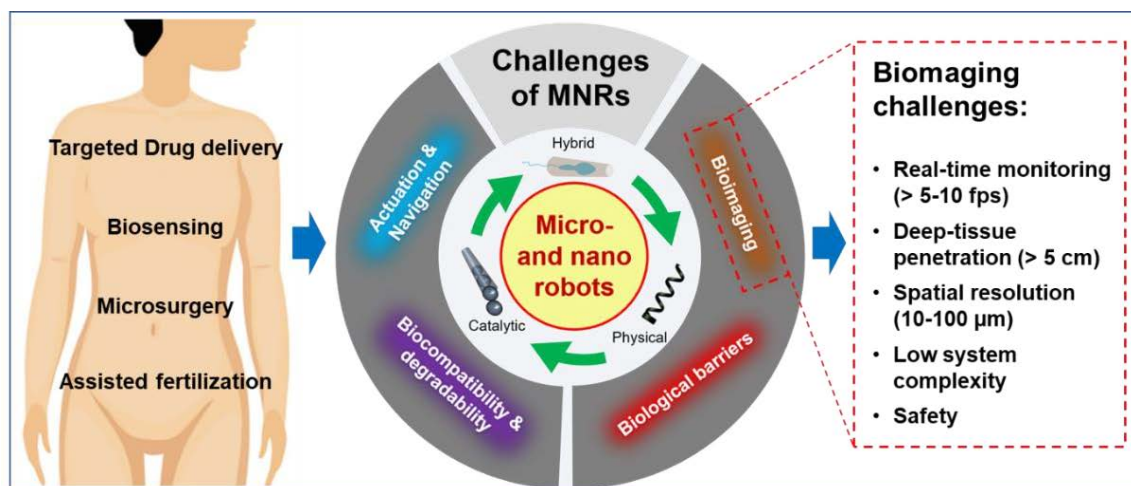


Figure 1.1. Opportunities and challenges of MNRs in their biomedical applications.

The intended applications of this thesis require high spatial and temporal resolution and ideally should be applicable in deep tissue, in particular, related to cancer

treatment or assisted fertilization. The thesis is the emphasis to achieve the required goals and the work focuses on real-time imaging of a single or very few magnetic micromotors (tubes and spheres) in phantoms, *ex vivo* tissue (mouse skull and chicken breast) or *in vivo* (mouse uterus and bladder cavities).

The work presented here demonstrates the use of an IR optical system to image single moving reflective micromotor through scattering phantoms and *ex vivo* mouse skull tissue which can be guided by an external magnetic field. This work is applicable to estimate the viscoelastic properties of biological fluids by determining the speeds of moving micromotor through viscous fluids or bloodstream. This technique provides better spatial resolution but lacks the penetration depth due to enhanced photon scattering in tissue. Photoacoustic imaging (PAI) overcomes this problem and provides deep tissue penetration. To evaluate the capabilities of this technique to track single micromotors, systematic experiments varying micromotor size, density of contrast agents decorating the micromotors, and different tissue thicknesses were carried out, demonstrating a successful tracking of single magnetically driven micromotor (in sizes of 25, 50 and 100 μm) below 1 cm *ex vivo* chicken breast tissue.

Moreover, the use of hybrid High-Frequency Ultrasound and Photoacoustic (HFUS and PA) imaging is demonstrated as a better approach to capture molecular and anatomical information of micromotors in different synthetic and biological environments. Furthermore, the micromotors are visualized in mice bladder and uterus in real-time. Finally, 3D multispectral imaging is performed to locate our MNRs deep in the tissue which is an important parameter to distinguish MNRs deep in the body from other absorbing chromophores present in the body.

1.2 Background

1.2.1 Microrobotics

Micro- and nanorobots (MNRs), are highly functional autonomous devices that aim at biomedical applications driven by biological organisms, self-propulsion or external power sources. The field of microrobotics brings together different disciplines like physics, engineering, material science, chemistry, biology, and medicine. The purpose of this field is either to mimic the behavior of biological components or to use whole cells or their components to create functional microdevices.

There have been plenty of approaches to develop artificial MNRs of various designs with simple geometries such as rods, tubes, spheres, and helices, which can propel by chemical reactions,^{6–13} physical fields,^{14–25} motile cells or microorganisms inclusion.^{26–32} The use of MNRs towards biomedical operations like minimal invasive surgery,^{17,33} targeted drug delivery, diagnosis,^{34,35} and to perform several other functions,^{31,35–41} has led to interesting progress in recent years. Schematic shows medical MNRs (chemical, physical, and bio-hybrid) swimming in the bloodstream (**Figure 1.2**) for potential biomedical applications. Other advances are the demonstration of an artificial micromotor inside the stomach of a mouse⁴² or the motion of rod-shaped nanomotors inside living cells by ultrasound.²⁰ However, the efficient operation in physiological environments requires precise control over MNRs locomotion and function to enable target reaching and efficient task performance. The avoidance of toxic fuels remains the challenge for potential biomedical applications of artificial MNRs *in vivo*.

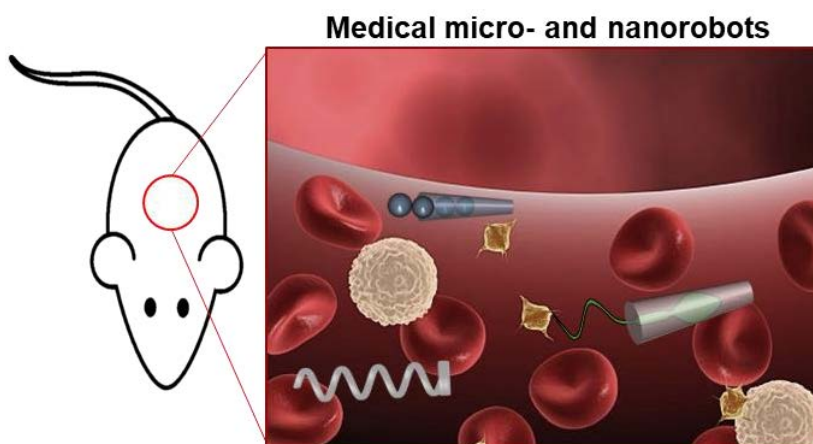


Figure 1.2. Medical MNRs swimming in living organism.

Magnetic MNRs mimicking biological flagella in shape and dimension propel efficiently in low-Reynolds-numbers regimes, similar as bacteria or sperm do. For instance, artificial bacterial flagella^{43,44} and flexible magnetic swimmers are examples of such robots which in contrast to their natural counterparts does not have an on-board power source and should be actuated by continuously rotating magnetic fields. For example, magnetically-driven microhelices (mimicking bacteria flagellum) have been used to carry particles,⁴⁵ cells,¹⁶ and biomolecules.^{4,46}

Biological motors such as flagella or cilia function efficiently on the micro- and nanoscale in viscous media. These biological motors consist of biomolecular motor proteins such as myosin, kinesin, and dynein which form different complexes that convert chemical energy into mechanical work.⁴⁷ Another possibility to make use of

biological motors is to implement whole cells as actuators. Bacteria and sperm cells have been implemented as propulsion sources in various approaches for the development of bio-hybrid systems that may perform robotic tasks on the microscale.^{48,49} Motile bacteria have also been explored for their potential in developing microbiorobots. Microorganisms are especially attractive as components in microrobots because of their sensing and taxis abilities. For instance, magnetotactic bacteria are being explored for their potential as microcarriers in blood vessels and for cancer therapy.^{48,50}

1.2.2 Medical Imaging

This section discusses the current state of the art of medical imaging techniques that have been implemented to image MNRs in *in vitro*, *ex vivo*, or *in vivo* scenarios by highlighting and discussing the opportunities and limitations of each technique. To this aim, the spatial and temporal resolution as well as penetration depth are discussed to motivate the suitability of the technique for specific medical applications. Among the various challenges of MNRs in biomedical applications, imaging of them is a major hurdle towards clinical trials. In an ideal imaging scenario, captured images should have a high spatiotemporal resolution, deep tissue penetration (> 5 cm), non-invasiveness, high molecular contrast, and microrobot control. The clinically established and widespread imaging techniques such as infrared (IR) emission techniques, ultrasound (US), magnetic resonance imaging (MRI), computed tomography (CT), positron emission tomography (PET) and single-photon emission computed tomography (SPECT) are continuously improving in terms of technical specifications for new potential applications. Although various other imaging techniques may be available, here, we discuss the most promising candidates for the localization and tracking of MNRs in terms of three key parameters, namely spatial and temporal resolution as well as penetration depth (**Figure 1.3**).

Spatial resolution is the parameter that defines the minimal object size guaranteeing to image or, alternatively, which is the minimal distance possible between two objects to be discriminated from each other. Temporal resolution is the minimal time required to complete the data acquisition needed to reconstruct one complete image of the object. Penetration depth is the measure of how deep the probing signal can penetrate into tissues. All imaging techniques share a similar basic principle: a physical signal passes through the body/area under diagnosis and its interaction with the tissue causes transmission or reflection of the radiation which is then captured by a detector

array and processed into an image pattern.⁵¹ Different energy sources can be exploited ranging from electromagnetic fields (including light and high energy radiations) to US. Despite rapid development in the last decade, most of the MNR applications have been enabled by the use of optical microscopy in *in vitro* conditions, and translating such approaches to an *in vivo* environment is challenging³ and the way ahead to the clinical practice and to high therapeutic efficiency is however long. In fact, medical imaging techniques should be employed to visualize the physiological environment, including potential vascular and administration routes and the target site for therapy, and for assessing the position of MNRs in the biological environment.

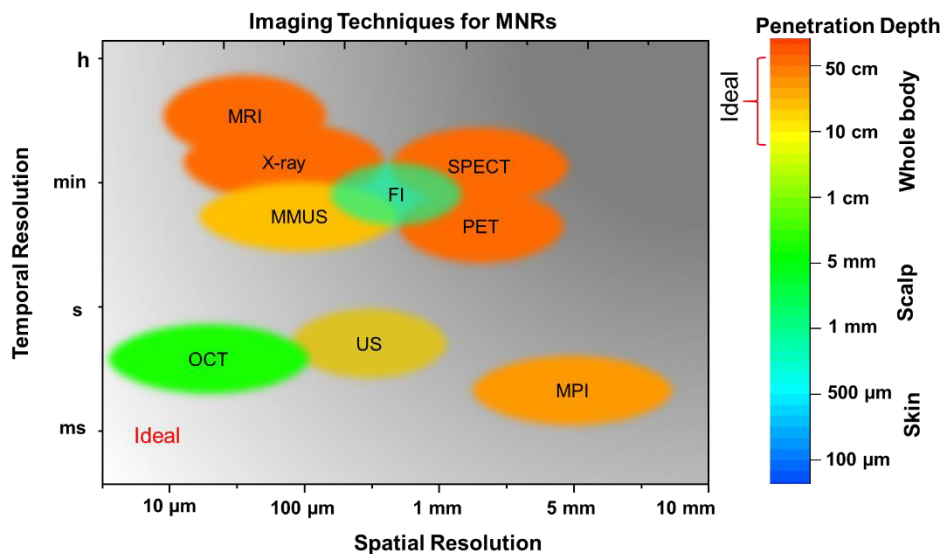


Figure 1.3. An overview of most widespread biomedical imaging techniques to visualize and control MNRs by highlighting their key parameters like spatial resolution, temporal resolution and tissue penetration depth. Magnetic Resonance Imaging (MRI); Magnetic Particle Imaging (MPI); Ultrasound (US) Imaging; Reflection-based Imaging (RI); Fluorescence Imaging (FI); X-ray Imaging (X-ray); Positron Emission Tomography (PET); Single Photon Emission Computed Tomography (SPECT); Magnetomotive Ultrasound (MMUS); Optical Coherence Tomography (OCT). Light gray region (lower left side) indicates the ideal scenario for spatial and temporal resolution for tracking medical MNRs, and the ideal penetration depth is marked as yellow-orange color.

Here, a brief overview of imaging and tracking capabilities of MNRs and key developments are described using conventional medical imaging modalities applied at the microscale. To date, various imaging techniques have been employed for the tracking of MNRs^{17,52-54} in particular to visualize swarms of them.^{30,46,55,56} However, the spatiotemporal resolution of such imaging techniques is insufficient to exert precise control and sensitivity over one or a few micromotors in deep biological tissues in real-time.

US offers deep tissue imaging inside the living body and enables real-time tracking but provides insufficient spatial resolution to track single micro-scale structures. An *in vitro* study has shown real-time tracking of a trail of microscopic bubbles from a fast-moving microjet engine (50 μm in length) using US with a spot size of $\sim 300 \mu\text{m}$.⁵³ The same group also demonstrated 3D position control of a magnetic sphere (800 μm in diameter) under US guidance.⁵⁷ Also, a microrobotic swarm was tracked in biofluids.⁵⁸ These swarms are particularly convenient to capture due to their enhanced area density as compared to single tiny robots.

MRI is suitable for submillimeter resolution but has a limited temporal resolution for real-time monitoring of micromotors and demands complex infrastructure. MRI was used to image and steer a swarm of magnetotactic bacteria and magnetic beads *in vitro* and *in vivo* (e.g. swine) across the vasculature.⁵⁹⁻⁶¹ Likewise, a swarm of naturally occurring *Spirulina platensis* micromotors was imaged in living mice using MRI,⁴ at a temporal resolution of ca. 0.2 frames per minute.

Nuclear imaging techniques, like PET and SPECT in combination with CT,⁶² offer high sensitivity⁶³ and molecular information, but utilize ionizing radiation which could be a drawback if prolonged radiation is required to observe the micromotors while controlling them for long periods of time.^{62,63} Recently, some attempts to exploit nuclear imaging techniques to monitor and track MNRs for medical applications have been reported. PET in combination with anatomical techniques like CT was used to track a cluster of catalytic micromotors (single tube length $\sim 12 \mu\text{m}$) labeled with radioactive isotopes in transparent glass tube phantoms.⁵² The absorption onto the micromotor surface of ^{124}I enabled PET tracking with 7 frames over 15 minutes. Another study reported the use of SPECT imaging to localize soft hydrogel-based thermoresponsive microrobots and track their shape transition for controlled release of drugs in the target site. Imaging of single millirobot (3mm) in different configurations and across various dimensions was enabled by the inclusion in the hydrogel structure of $^{99\text{m}}\text{Tc}$ Zinc colloids. Results obtained with nuclear imaging were confirmed by comparison with CT images and with *ex vivo* study, where the millirobots were injected in the peritoneal cavity of a mouse.⁶⁴

Recently, metal-coated particles were propelled in aqueous solution using a full-field transmission X-ray microscope to actuate and image in real-time half-metal-coated Janus microparticles in aqueous solution. Both propulsion and visualization of the particles are activated by X-ray radiations.⁵⁴ This work opens the possibility to combine locomotion and imaging while achieving spatial resolution in the range of hundreds of nanometers. The extended X-ray exposure to the tissues can be harmful to guide the micromotors to the region of interest.

Optical techniques utilize non-ionizing radiation sources such as lasers or LEDs. Such techniques are relatively fast, safe and low cost and offer high spatial (order of few μm) and temporal (order of millisecond to seconds) resolutions. However, most optical techniques suffer from low penetration depth in biological tissues and are however limited to the investigations at sub-surface levels, typically between hundreds of micrometers and rarely beyond 1 mm deep.^{65,66} Few examples of imaging of MNRs are explained based on fluorescence-based imaging (FI). In this context, micromotors based on *Spirulina platensis* were fabricated via dip-coating in a suspension of Fe_3O_4 NPs. These micromotors exhibited magnetic properties and biocompatibility due to their biogenic nature. The innate autofluorescence (emission at 660 nm) was achieved with an excitation wavelength of 552 nm, allowing the tracking of a swarm of micromotors (ca. 10000 spirulina micromotors with a typical length of single structure $\sim 100 \mu\text{m}$) *in vivo* with a spot size in the millimeter range (about 3-5 mm) and a temporal resolution of ~ 0.2 fps. This study was limited to subcutaneous tissues due to the strong scattering of light at the specific emission wavelength. To overcome this problem, the inclusion of fluorescent dyes that emit in the IR region (700-950 nm) was proposed in one of the first *in vivo* studies of magnetically controlled microswimmers employing FI. They fabricated artificial bacterial flagella (ABFs) labeled with an isothiocyanate dye (NIR-797)⁴⁶ with an emission peak around 810-875 nm when excited at 745 nm and placed under a rotating magnetic field. A swarm of labeled magnetic ABFs (detection limit ~ 15000 ABFs per ml) was tracked *in vivo* in the peritoneal cavity of a mouse when moving under rotating magnetic fields (9 mT, 90 Hz) with a temporal resolution of approx. 1 frame per second.

Optical coherence tomography (OCT) is an interferometric technique which provides high spatial resolution (1-15 μm). OCT was employed to track magnetically-driven spherical microrobot (90 μm in diameter) *in vivo* in the portal vein of mice at a penetration depth of ~ 1.6 mm, with a line scanning rate of 5.5-70 kHz.⁶⁷ The similar technique was also used to track cluster of reflective particles (polystyrene, 2 μm in diameter) as contrast agents to improve imaging contrast in OCT in *ex vivo* mice liver and *in vivo* in zebrafish.⁶⁸

1.3 Objectives and Structure of Thesis

Real-time tracking/imaging enables us to monitor the capabilities of employed micromotors in deep tissue, for instance, for sensing, cargo transport, or sperm-transport, among others. The key objective of this thesis is to investigate and

implement a reliable medical imaging technique for visualizing 2D/3D microstructures through scattering tissues (in phantom, *ex vivo*, and *in vivo*), in real time. To accomplish this objective, we explore non-invasive, high spatiotemporal resolution, deep tissue, and compact imaging setups. The first imaging technique involves the development of an optical imaging setup integrated with a 3D magnetic coil system and real-time detection of microstructures in tissues. While keeping the goal of this work in mind, the optical technique is limited to very thin or sub-skin level tissues and cannot penetrate deep tissue due to pronounced scattering of photons. This motivates the use of photoacoustic imaging which employs the detection of ultrasound waves and provides deep tissue penetration down to ~ 1 cm in scattering phantom and chicken breast tissues. To take advantage of US for deep tissue imaging, we further explore the use of hybrid high-frequency ultrasound and photoacoustic (HFUS and PA) imaging for the tracking of micromotors in mice bladder and uterus.

The Thesis is structured in seven chapters. Chapter one deals with motivation and background of microrobotics and the employed medical imaging techniques.

Chapter two (Fundamentals) an overview and state of the art of the three different imaging techniques employed in this work (optical IR, photoacoustic and ultrasound) are presented. The last subsection discusses light tissue interaction and possible light loss mechanisms.

Chapter three (Materials and Methods) first subsection describes the fabrication of magnetic micromotors, material deposition methods and surface functionalization of micromotors with gold nanorods. The second subsection provides the fabrication of phantom and *ex vivo* tissues. The third subsection discusses two main characterization methods employed in this thesis, which are in particular optical microscopy and scanning electron microscopy (SEM). The fourth subsection describes magnetic actuation systems (magnetic field gradient and rotating magnetic field) employed in all imaging techniques. The final subsection provides protocols for mice handling.

Chapter four (Optical imaging of microrobots) discusses the concept and design of reflective micromotors. Furthermore, this chapter discusses IR imaging setup and performance of single reflective micromotors in phantom, *ex vivo* (mouse skull tissue), and blood samples.

Chapter five (Photoacoustic imaging of microrobots) starts with an introduction of absorber micromotors and design and fabrication of them. The following subsections discuss the photoacoustic imaging setup and actuation and propulsion performance of single moving micromotors in phantom and *ex vivo* (chicken breast) tissues.

Chapter six (Hybrid ultrasound and photoacoustic imaging) presents a hybrid high-frequency ultrasound and photoacoustic imaging of single micromotors in phantom, *ex vivo* (chicken breast) and *in vivo* scenarios (mice bladder and uterus). Furthermore, we explore the use of multiwavelength excitation to spectrally distinguish the employed micromotors from the surrounding tissues. This section ends with highlighting possible applications of presented micromotors using a hybrid system.

Chapter seven (Summary and Perspectives) summarizes the thesis and concludes the achievements using three different imaging modalities with different functionalities. This section ends with discussing potential contrast-enhancing labels and further unexplored imaging concepts for MNRs.

2 FUNDAMENTALS

Although much progress has been carried out in the development of synthetic MNRs, the translation of these devices in the clinical applications is still obstructed due to the absence of suitable *in vivo* imaging methods. Furthermore, the *in vivo* environments carry dynamic, heterogeneous, and complex systems rich with biomechanical forces such as blood flow, body motion, heart beating, or lung expansion. The accurate movement of such MNRs in a highly complex or dynamic environments followed by their tracking is highly challenging. Thus, efforts are required in the development of imaging tools and protocols for propelling micro/nanostructures to control their movement and localization in biological environments. Such control will lead to various medical applications including targeted drug delivery, cell transport, tissue diagnosis, and biomedical imaging at a specific body site that has limited access.

Despite various other imaging techniques as highlighted in the previous section, this thesis will focus on three imaging techniques (optical IR, photoacoustic and ultrasound) by highlighting their advantages over conventional imaging methods and some limitations in particular applications.

2.1 Optical Imaging

In comparison with other imaging modalities such as X-rays or PET/SPECT, which use hazardous radiation, optical imaging utilizes non-ionizing radiation sources such as lasers or LEDs which emit in the IR range. Two optical windows exist in the NIR range: the first biological window (NIR-I) which ranges from 650-950 nm and the second (NIR-II) ranging between 1000-1350 nm.⁶⁹ Such techniques are relatively faster and safe, offering low cost, high spatial (order of few μm), and temporal (order of millisecond to seconds) resolution. However, most optical techniques suffer from low penetration depth in biological tissues and are still limited to the investigations at sub-surface levels^{65,66} typically between hundreds of micrometers and rarely beyond 1 mm. The light penetration into tissues is limited by scattering and absorption at different biomolecules and endogenous chromophores. The exact behavior depends on the

tissue properties. These properties can be described by the mean free path (MFP) which is the average distance a photon travels between two scattering or absorption events and is defined as:

$$\text{MFP} = \frac{1}{\mu_s} + \frac{1}{\mu_a} \quad (1)$$

where μ_s and μ_a are the scattering and absorption coefficients, respectively.⁶⁶

One strategy to overcome the limited penetration depth of optical techniques is to choose an appropriate wavelength window in the NIR which can significantly reduce the tissue autofluorescence and light absorption. For higher penetration depths, the use of NIR-II is desirable as it has been demonstrated elsewhere.⁶⁹ Hence, in the appropriate wavelength range, μ_s is much larger than μ_a for most of the tissues e.g. muscle, brain, breast, and lung tissues, and the MFP becomes $1/\mu_s$. Scattering in biological tissues occurs predominantly in the forward direction (the direction in which the light strikes the tissue). This is considered by the anisotropy factor “g” which defines the degree of forward scattering $g=1$ would mean total forward scattering and $g=-1$ total backscattering. Typical values for biological samples are in the range of $g \sim 0.9$. The transport MFP (TMFP) considers the MFP and the average angle in which photons are scattered and is linked to the MFP by the reduced scattering coefficient $\mu_s' = \mu_s(1-g)$ and the TMFP is defined as $\text{TMFP} = 1/\mu_s'$.⁶⁶

Another strategy to improve the penetration depth is to tune the emission features of target objects (i.e. MNRs) by incorporating dedicated contrast agents or labels. For the sake of clarity, we have organized the optical imaging techniques used for MNR tracking into reflection-based and fluorescence-based techniques (**Figure 2.1**).

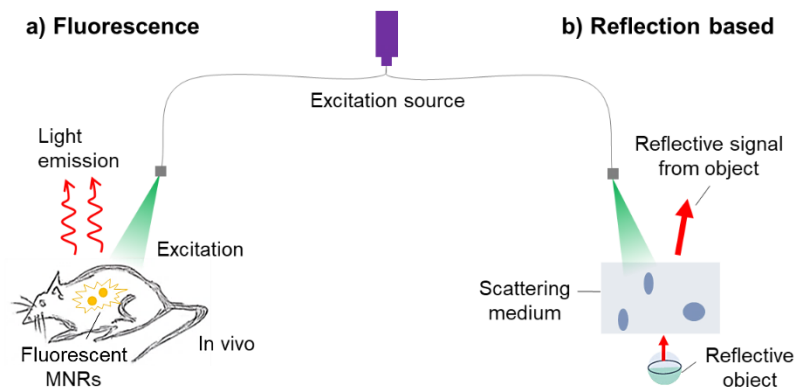


Figure 2.1. Basic principle of fluorescence imaging where light is emitted from target MNRs upon excitation. b) Reflection-based imaging where incident light is reflected back from the target micro-object underneath scattering tissue.

2.1.1. Reflection-based Imaging

Optical techniques are widely exploited in body districts where the scattering of tissues is relatively low, e.g. in ophthalmology, sub-skin intervention, and small animal experiments. As the penetration depth of light in tissue is comparably small, optical techniques are mostly used in reflection rather than transmission configuration, meaning that the illumination and detection are done with single-sided optical access to the sample. Reflection-based imaging (RI) does not rely on the emission of a fluorescent probe but on the intrinsic reflection or backscattering properties of the sample. Nanoparticles (NPs) or thin metal layers incorporated on target samples can be used to enhance signal reflectivity. In this regard, gold (Au) is one of the most suitable materials for its biocompatibility and high reflectivity over a broad spectral range.⁷⁰ However, when scattering scrambles both the illumination and the backscattered light, a high amount of background light occurs, which strongly reduces the signal to noise ratio (SNR). In the worst case, the scattered light saturates the detector, and no sample information can be recorded. To reduce saturation and scattering, depth sectioning techniques can be employed. In this regard, confocal microscopy is based on filtering out-of-focus light using a pinhole.^{71,72} Optical coherence tomography (OCT) is an interferometric technique that was first developed by Fujimoto's group⁷³ in 1991 and takes advantage of the short coherence length of a light source which allows recording coherence gated images and obtains μm -scale cross-sectional imaging of the target. OCT provides improved spatial resolution (1-10 μm) in scattering tissue, but with high acquisition times due to the point-wise (time-domain OCT) or line-wise (frequency-domain OCT) scanning mode, thus avoiding real-time imaging.⁷⁴⁻⁷⁶

Several studies reported the use of OCT imaging for tracking microagents. For instance, this technique was used to track reflective particles (polystyrene, 2 μm in diameter) as contrast agents to improve imaging contrast in OCT in *ex vivo* mice liver and *in vivo* in zebrafish.⁶⁸ Likewise, SiO_2 particles (1.2 μm in diameter, half-coated with a thin film of Au) were functionalized with a specific antibody that recognizes a biomarker (cardiac troponin I) of acute myocardial infarction to perform on-chip nonspectroscopic optical immunosensing.⁷⁷ By following the same principle, Nelson's group tracked the position of a microrobot (size: $285 \times 1800 \mu\text{m}$) for minimally invasive intraocular surgery. The magnetic robots were steered using rotating magnetic fields in *ex vivo* porcine eyes as well as *in vivo* in lapin eyes and consecutive images were acquired at a speed of 15 Hz.⁷⁸ Strategies such as pulsed laser excitation, and the usage of wavelengths in NIR-II optical window can improve the achievable penetration

depth. While the discussed methods suppress the scattered light, they result in a strong reduction of the SNR.

2.1.2. Fluorescence-based Imaging

Fluorescence imaging (FI) is a widely used biomedical imaging modality; its working principle relies on the well-known Jablonski energy diagram⁷⁹ which describes the molecular fluorescence from excitation to emission. The process initiates by the absorption of an incoming photon (light source) after exciting the target molecule, followed by the vibrational relaxation of excited state electrons to the lower energy level. Finally, the emission of a longer wavelength photon appears and the excited molecule returns to the ground state. The emission efficiency is reduced after excitation to emission processes and the amount of emitted light is randomly dispersed and collected efficiency reduces.

FI requires an excitation light source, a detector, and image-forming optics to produce a visual representation of the target object based on the distribution of fluorescent labels. Fluorescence or two-photon fluorescence microscopy⁸⁰ allows the reduction of background noise by using wavelength filters that suppress or at least reduce the contribution of the scattered light to the recorded signal. FI can have relatively low cost and produces no harm to living organisms if used in the IR range within the allowed exposure limits (typically 329 mW/cm² at 808 nm) indicated by the International Commission on Non-Ionizing Radiation Protection guidelines.⁸¹ Fluorescence emission can be provided by specific labels or can be an intrinsic property of the materials (autofluorescence). Autofluorescence is the natural emission of light from structures upon light absorption. This is the case of proteins such as tyrosine and melanin, spirulina plant or non-biological polymer materials like photoresists. For instance, SU-8 photoresist shows an emission peak in the blue region of the spectrum (between 400-490 nm). This property enables to track magnetic microrobots obtained from SU-8 doped with iron oxide powder in 2D open cell culture chambers while performing particle and cell manipulation.⁸² Other examples of autofluorescent structures are the micromotors based on *Spirulina platensis*. Spirulina micromotors (after inclusion of Fe₃O₄ NPs) exhibited magnetic properties and biocompatibility due to their biogenic nature. The innate autofluorescence (emission at 660 nm) of the microalgae was achieved with an excitation wavelength of 552 nm, allowing the tracking of a swarm of micromotors (ca. 10000 spirulina micromotors with a typical length of single structure ~ 100 μm) *in vivo* with a spot size in the millimeter range (about 3-5 mm) and a

temporal resolution of ~0.2 fps. This study was limited to subcutaneous tissues due to the strong scattering of light at the specific emission wavelength.

To overcome this problem, the inclusion of fluorescent dyes that emit in the IR region (700-950 nm) has been proposed by Nelson's group who reported one of the first *in vivo* studies of magnetically controlled microswimmers employing FI. They fabricated artificial bacterial flagella (ABFs) labeled with an isothiocyanate dye (NIR-797)⁴⁶ with an emission peak around 810-875 nm when excited at 745 nm. A swarm of labeled magnetic ABFs (detection limit~15000 ABFs per ml) was tracked *in vivo* in the peritoneal cavity of a mouse when moving under rotating magnetic fields (9 mT, 90 Hz) with a temporal resolution of approx. 1 frame per second.

Standard fluorescent labels^{83,84} have limitation issues associated with signal intensity strength, photobleaching, and short lifetimes.⁸⁵ Additionally, these fluorophores produce broad emission spectra that create overlapping detection ranges, making data analysis more challenging as highlighted by Nelson and coworkers.⁴⁶ To address these limitations, continuous development of new species based on semiconductor nanocrystals have been carried out, in particular, aimed at the development of a variety of quantum dots (QDs),⁸⁶ and more recently the upconversion nanoparticles,⁸⁷ that offer high sensitivity and penetration depths.

QDs are semiconductor nanoparticles, owing to many unique and attractive properties, such as controllable optical properties by varying the size (typically ~ 2 to 10 nm), narrow emission peak, and broad excitation range.^{86,88} QDs are more stable, robust and brighter and are advantageous for both single and multi-color experiments as compared to conventional dyes.⁸⁹ QDs owing to improved photostability and brightness have been used in cellular and *in vivo* imaging and targeting.⁸⁵

There are few studies suggesting the use of QDs labeled MNRs, for instance, fabrication of self-propelled mobile MNRs as a sensing platform by incorporating CdTe QDs on the outer surface of poly(3,4-ethylenedioxythiophene) (PEDOT)/Pt microtubes through electrostatic self-assembly, serving as mobile microsensor to discriminate mercury species, Hg²⁺ and CH₃Hg⁺.⁹⁰ However due to their composition and the presence of heavy metals, QDs are toxic making them unfit for *in vivo* applications. The same group described the fabrication of Janus micromotors encapsulated with phenylboronic acid (PABA) modified graphene QDs to detect deadly endotoxins released from *Escherichia coli* bacteria.⁹¹ Such microrobots exhibited strong blue fluorescence emission signal (excitation ~ 360 nm and emission ~470 nm) under static and dynamic fluorescence imaging and were primarily used for targeting detection. Fluorescence quenching was observed during the interaction of microrobots and endotoxins present in urine and serum samples.

FI maintains several advantages owing to its inherent properties: no ionizing radiation is required; high-resolution images are made at a high speed, and this technique can be straightforwardly combined with other imaging modalities. Because fluorescent tags suffer the limitation of light penetration in biological tissues, it is a better choice to use this technique for MNRs application in exposed organs such as the eye or tongue, or near the skin. Another possibility is to look for NIR probes with longer wavelengths, meaning with reduced photon scattering and optical absorption (refer to the Future Perspectives section).

2.1.1 Light-Tissue Interaction

The interactions between light and the surrounding biological tissue are increasingly important at greater depths and both excitation and emission photons have to travel through thick biological tissue. This is essential for the excitation light to reach the target object and excite it, and for the emitted light from the object to reach the detector to be collected for image formation. Besides signal from the target object, the processes related to light-tissue interactions are interface reflection, scattering of photons, light absorption, and tissue autofluorescence (**Figure 2.2**).

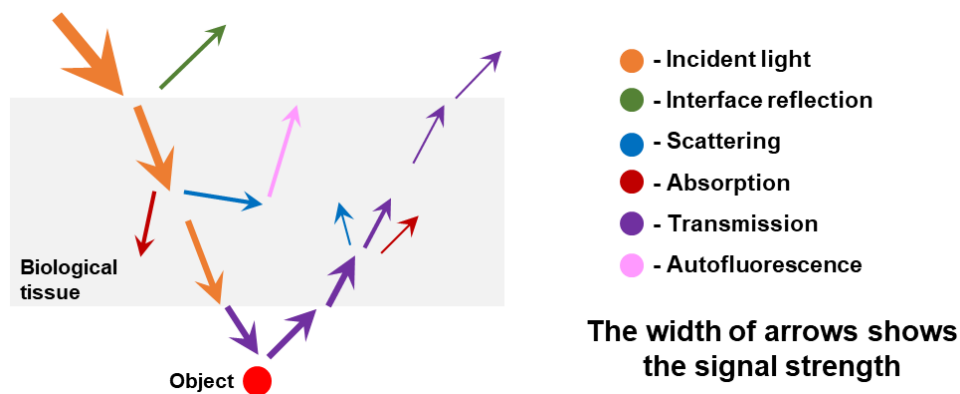


Figure 2.2: Light-tissue interaction resulting from incident light (orange). Interface reflection (green), scattering (blue), absorption (red) and autofluorescence (pink) all contribute to the loss of signal (purple).

Light absorption determines how far light can penetrate into specific tissue. Scattering in tissue remains another significant factor in light-tissue interactions. Together, absorption and multiple scattering of photons cause light beams to broaden and decay as photons travel through tissues. These two processes have an important influence on how light is measured from the outside.^{92,93}

2.1.1.1 Light Absorption

Absorption of light determines how much electromagnetic energy transforms into thermal energy. The intensity of light waves reduces as they pass through a medium or an object. In a homogeneous medium, light wave propagates along a straight path, and the loss of energy is often expressed by the Beer-Lambert law, which relates the attenuation of light to the medium properties. In this case, light interacts with the different absorbers present in the medium that absorb photons. After undergoing this process, light energy is dissipated through heat or light emission (e.g. fluorescence). This phenomenon can be represented through a global absorption coefficient μ_a , usually expressed in 1/cm (1/length). The absorption coefficient describes how much light energy is absorbed or lost by a material of a given thickness along with light propagation. The light power flux after propagating over a distance z is given by;

$$I(z) = I_0 e^{-\mu_a z} \quad (2)$$

where I_0 indicates the input light power flux and absorption coefficient (μ_a) defines the absorption mean free path which is the average distance (z) a photon travels through a medium before experiencing an absorption event.

2.1.1.2 Light Scattering

Scattering is a process of photon absorption and re-emission with a change of photon direction without the loss of energy after interacting with molecular species or a medium. The light energy is dissipated through absorption while propagating inside a homogeneous material. In practice, many objects are inhomogeneous and consist of interfaces associated with varying refractive indices. Biological tissues are also inhomogeneous media. These inhomogeneities cause scattering of incident light and physics of light attenuation cannot be explained from the Beer-Lambert law.

The accumulation of multiple scattering events results in randomization of the propagation direction. The mean free path (MFP) is the average distance a photon travels between two scattering or absorption events. In an appropriate wavelength window, scattering coefficient (μ_s) is much larger than μ_a for most of the tissues e.g. muscle, brain, breast, and lung tissues, and the MFP becomes $MFP = 1/\mu_s$.⁶⁶ Scattering in biological tissues occurs predominantly in the forward direction (the direction in which the light strikes the tissue) for each scattering event. This is considered by the anisotropy factor “ g ” which defines the degree of forward scattering.

$g=1$ would mean total forward scattering and $g=-1$ total backscattering. Typical values for biological samples are in the range of $g\sim 0.9$. The transport MFP (TMFP) considers the MFP and the average angle in which photons are scattered and is linked to the MFP by the reduced scattering coefficient $\mu_s' = \mu_s(1-g)$ and the $TMFP = 1/\mu_s'$.⁶⁶

Scattering occurs in the whole spectral region, but it is particularly strong in the ultraviolet (<450 nm), visible (450-690 nm) and IR (700-950 nm) regions due to photon interaction with cellular structures.⁹⁴ There is less scattering in the IR region as compared to the ultraviolet and visible regions.

Light scattering can be explained either as scattering by particles or by a medium and the terms Rayleigh scattering and Mie scattering are used to describe them. Rayleigh scattering refers to scattering by particles much smaller than the wavelength of light and Mie scattering refers to scattering by particles comparable in size or larger than the wavelength of light. Schematic of Rayleigh scattering, where incident photons interact with a very small particle (radius $\sim 10^{-4}$ μm), and Mie scattering, where photons interact with small (radius ~ 0.1 μm) or larger (radius ~ 1 μm) particle are shown in

Figure 2.3.

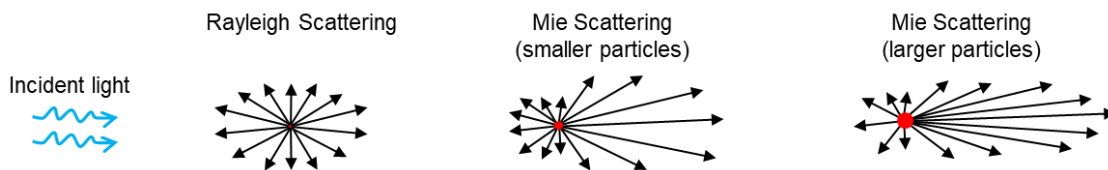


Figure 2.3. Schematic of Rayleigh scattering and Mie scattering, where incident photons interact with a very small (radius $\sim 10^{-4}$ μm), small (radius ~ 0.1 μm) or larger (radius ~ 1 μm) particle.

Rayleigh scattering^{95,96} is the elastic scattering of incident electromagnetic radiation by particles much smaller than the wavelength of the incident light. For instance, this condition is met when visible light interacts and scatters by the atmosphere (N_2 , O_2 or CO_2). The electromagnetic wave, after interacting with a particle, induces charge oscillations and local oscillating dipoles. The electromagnetic field becomes homogeneous after interacting with very small scattering particles. All local dipoles oscillate and the particle acts as a unique dipole. In Rayleigh scattering, the scattered power is strongly wavelength dependent and this scattering is inversely proportional to the wavelength raised to the fourth power ($1/\lambda^4$).

In Mie scattering,^{97,98} when the size of the particle becomes similar or bigger compared to the wavelength of the incident light, the field distribution cannot be considered as homogeneous over the particle volume. The signal is then proportional to the square of the particle diameter.

2.2 Photoacoustic Imaging

2.2.1 Theory

Photoacoustic (or optoacoustic) imaging (PAI) has emerged as a novel medical imaging technique in the last decade^{66,99-102} and was first introduced by Alexander Graham Bell¹⁰³ in 1880 upon observation of the sound waves generated by the sunlight. As the method includes combination of two fields that is ultrasound and optics, it has attracted the attention of applied mathematicians, clinical imaging specialists, applied physicists, and biomedical engineers. PAI relies on the 'light-in, sound-out' approach: IR light penetrates the biological tissue and generates ultrasonic waves following the absorption of light. Short-pulsed or periodically modulated electromagnetic radiation is delivered with wide-field illumination and is absorbed by specific chromophores which cause a localized and rapid increase in temperature and - in turn - US pressure waves (**Figure 2.4**). The sound waves generated from the optical absorbers are reconstructed by using image generation algorithms.¹⁰⁴ The contrast of PA images comes from the distribution of the absorbed optical energy and is thus related to the optical properties of the tissues and the wavelength of the incident light.¹⁰⁵ The method is opposite to the optical imaging in which multiple scattering events randomize the direction of a photon that deteriorates contrast and resolution upon photon detection. The photoacoustic strength arises from its detected energy which is US that undergoes low scattering in the tissue in comparison to the optical imaging. The result carries optical absorption spatial distribution deep in the tissue showing greater depth and better resolution as compared to other optical imaging methods.

The fundamental contrast mechanism from optical absorption carries information related to the tissue components including melanin, lipids, hemoglobin, bilirubin, water and oxy-hemoglobin.¹⁰⁶ Additionally, each chromophore carries particular spectral signatures, separating them from one another. The spatial resolution of PAI is derived from the US transducers, including the frequency response and spatial sampling steps of the US detector. Both the resolution and imaging depth correlate with the US detection frequency. A higher frequency of US signal would result in better spatial resolution but decreases the imaging depth. The higher US frequencies would attenuate more as compared with lower frequencies. Typically, the spatial resolution of PAI ranges from several tens of micron (depth of a few mm) to sub-millimeter (depth of a few cm).¹⁰⁰

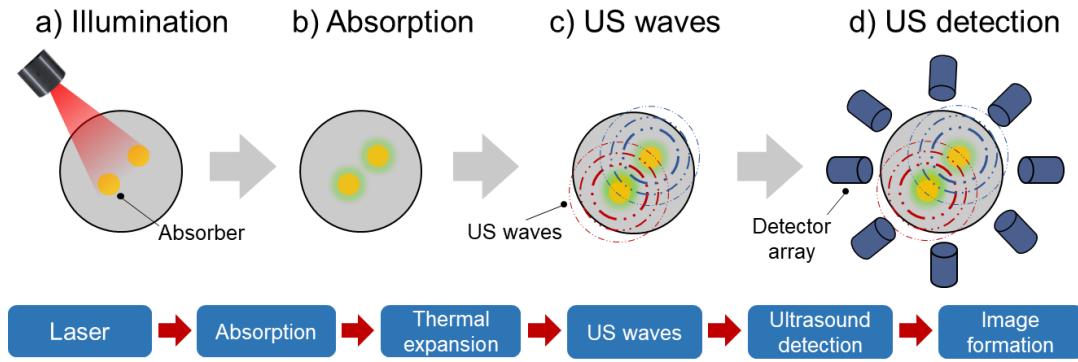


Figure 2.4: The basic principle of photoacoustic imaging. When an absorber is exposed to pulsed laser light, it absorbs light and undergoes thermoelastic expansion, thereby generating ultrasound signals (the photoacoustic effect). These laser-induced US signals can be detected using an ultrasound transducer array.

Different US piezoelectric transducer geometries have been proposed: linear and cylindrical, for two-dimensional imaging whereas spherical arrays allow the acquisition of a 3D data set.^{107,108} Typically a PAI system comprises a pulsed IR laser (600-900 nm and 1100-2000 nm, 1 to 100 ns pulse widths and 10-50 Hz pulse frequency), US transducer (256 or 512 elements) and on-board image reconstruction equipment.

PAI takes advantage of endogenous chromophores (e.g. lipids, melanin, hemoglobin) available in the body or exogenous contrast agents that absorb light at specific characteristic wavelengths^{109,110} thus enabling their detection and identification with respect to the surrounding tissues and structures.^{111,112} For instance, oxy- and deoxy-hemoglobin can provide anatomical functional information of vascular structures including blood oxygen saturation, flowrate, and metabolism by employing multi-wavelength excitation.^{99,113-115} PAI has the advantage of spectrally unmix the absorption spectra from diverse sources of absorption, thus enabling to discriminate structures and processes based on their composition or on the involved molecules. A rich choice of exogenous contrast agents (dyes, NPs and reporter genes) can be used for molecular imaging. PA signals can be treated to extract both anatomical and functional features of the tissue microenvironment. There have been several advancements in the PA reconstruction algorithms: deconvolution algorithms to retain the structural information,¹¹⁶ filtered-back-projection algorithms,^{117,118} and single-stage algorithms for high-quality imaging¹¹⁹ have been proposed depending on the intended application. The spatial resolution of PAI depends on the features of the US transducers, including the center frequency and the spacing between piezoelectric elements. Both the resolution and the imaging depth correlate with the US detection frequency, as well as, on the applied light wavelength and its pulse repetition rate. The

spatial resolution of PAI ranges from several tens of micron (depth of a few mm) to sub-millimeter (depth of a few cm).¹²⁰

2.2.2 Implementation

From a long time, medical specialists are working on the early clinical and preclinical investigations owing to the countless possibilities in high-resolution microvasculature visualization along with the health and disease monitoring and the field is growing with applications, for instance, in dermatology,¹²¹ cardiology,¹²² neurology,¹²³ oncology¹²⁴ with a wide range of contrast agents.

PAI has been also used to image anatomical features like human vasculature,^{125,126} to assess fatty tumors,¹²⁷ monitor blood flow, and oxygen state,¹¹⁵ and to detect melanoma cells in sentinel lymphnodes¹²⁸ – but not yet dynamically for tracking single moving MNR. Within this context, PAI appears to be a promising technique as it allows real-time imaging in deep tissue,¹²⁹ a resolution in the $\sim\mu\text{m}$ range and molecular specificity required for distinguishing the spectral signatures of the MNRs from surrounding tissue for future *in vivo* studies.^{99,114,130–132}

Similar to other imaging modalities, contrast agents can be used to improve image contrast and targeting in PAI. In particular nanoparticles or molecular chromophores with strong optical absorptivity and characteristic spectral profiles in the NIR spectral range are preferred. Among various contrast agents,^{109,110} gold nanorods (AuNRs) are excellent candidates due to their absorption spectrum which can be tuned across the NIR region by varying their size and shape,^{133,134} and their molar extinction coefficients are much higher than those of endogenous tissue chromophores like water, melanin, and hemoglobin.¹³⁵ AuNRs have been previously used for cell tracking.¹³⁶ First, AuNRs were uptaken by cells via endocytosis for further PA tracking, however, after cell uptake, the confinement and the presence of endosomes lead to the AuNRs plasmon band broaden and reduced absorbance. Therefore, the authors of this work showed that by coating the AuNRs with silica, they can provide them with steric hindrance which improves the resulting photoacoustic signal and preserved their spectral properties. This approach allowed the tracking of 2×10^4 mesenchymal stem cells in mice over a period of 15 days with high spatial resolution and without affecting the viability or differentiation potential of the transplanted cells.¹³⁶ PAI has also been used to screen ovarian cancer cells for early diagnosis. In this study, AuNRs were used as passively targeted molecular imaging agents, showing the highest PA signal *ex vivo* and *in vivo* for an aspect ratio of 3.5. After 3h, the maximum PA signal was observed for the 2008, HEY, and SKOV3 ovarian cancer cell lines in living mice and a linear

relationship between the PA and the concentration of the injected molecular imaging agent was observed with limits of detection of 0.4 nM AuNRs, being lower than other labels in the literature.¹³⁷

However, the maximum tissue penetration depth has been limited to optical excitation due to the strong attenuation of light in biological tissues.^{120,138} There is still a need to overcome the penetration depth limits imposed by light to enable MNRs in human tissues (>5 cm deep) for any medical tasks.

In summary, PAI combines the advantages of structural discrimination of light-based imaging with the penetration depth of US-based imaging,^{120,138} and the possibility to perform spectral unmixing is a substantial feature to extract optical signatures of MNRs from the surrounding tissues. It would be even advantageous to combine real-time US/PA with pre-acquired MNR images towards more efficient diagnosis and therapy.¹³⁹ Another study highlights the dual-imaging system based on PAI and OCT for surgical guidance.¹⁴⁰ However, many applications require real-time imaging well beyond the penetration depths of PAI which is still challenging.

2.3 Ultrasound Imaging

2.3.1 Theory

US imaging is a widely-used, well-established, radiation-free medical imaging technique. It is a mature technology regularly used in clinical settings and it has been applied in clinical diagnostics such as cardiology, pelvis, orthopedics, and uterus. This technique is based on the reflected acoustic waves that have interacted with the imaging objects and their surrounding environments. Amongst conventional techniques, US-based imaging stands as one of the most promising solutions for providing real-time feedback on microrobot position in deep tissue. US shows high temporal resolution with minimum adverse effects on tissues and lower equipment costs.

US imaging modes (e.g., Brightness mode (B-mode), Doppler-mode) provide the potential for applying MNRs to perform medical tasks in different environments. The B-mode US is commonly used in both clinic and pre-clinical trials and is a pulse-echo imaging modality in which a pulse wave is transmitted by a piezoelectric transducer. When the US waves encounter acoustic impedance discontinuities, the backscattered echoes generated by the interaction of the wave with the propagating media are

processed¹⁴¹ to reconstruct an image of the target object or scatterer (**Figure 2.5**). Several US beams can be independently shot and registered back by an array of piezoelectric elements (US probe) to acquire adjacent scan lines which are then combined to reconstruct a 2D tomographic image.

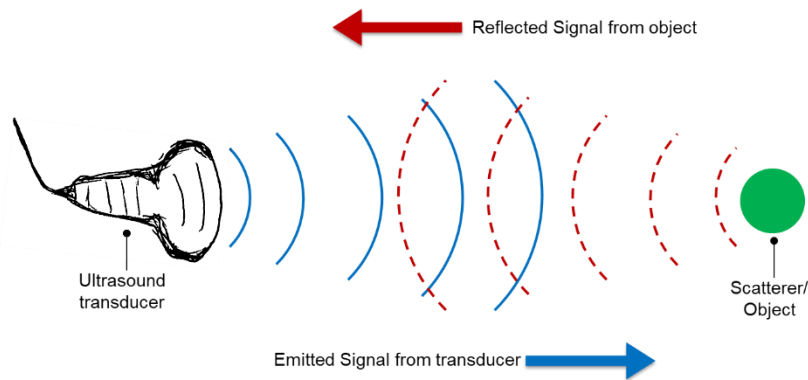


Figure 2.5: Basic principle of US imaging

When propagating in human tissues, US waves are strongly absorbed by bones (producing acoustic shadows) and highly reflected by air sacs. Due to its strong echogenicity (i.e. the property of backscattering US waves), the air is generally used as a contrast agent, for instance in the form of microbubbles. These are micron-sized spheres consisting of a gas core surrounded by a lipid shell which acts as echo-enhancers.¹⁴²

In US, the temporal resolution depends on the speed of sound in the medium (about 1500 m/s in soft tissues)¹⁴³ and on the FoV. Typical frame rates are in the order of 50-100 fps, while greater rates are achieved by plane wave imaging (>1000 fps).¹⁴⁴ The spatial resolution is defined by two parameters, namely axial and lateral resolution. The lateral resolution depends on the geometry of the US probe since it is related to the distance between the piezoelectric elements of the probe array. Axial resolution is related to the wavelength of the transmitted pulse (typically 100-500 μm) and thus to both the characteristics of the transducer (center frequency) and the properties of the medium (speed of sound). Due to wave diffraction, objects with characteristic dimensions comparable to the US wavelength are not well resolved. Ideally, axial resolution is defined by one half of the transmitted pulse wavelength. However, as a result of the combined effect of the physical processes involved (i.e. scattering and diffraction) and of the reconstruction procedure (e.g. imaging artifacts), the axial resolution is usually worse than the ideal value.¹⁴⁵ A higher axial resolution can be obtained by increasing the transmission frequency, yet at the expense of the

penetration depth (wave attenuation increases with frequency). Altogether, axial resolution can vary between hundreds of micrometers at 3-4 cm depth for 12-15 MHz and at 20 cm depths for 3-5 MHz US waves, generally used in standard abdominal B-mode imaging.¹⁴⁶

2.3.2 Implementation

In the past few years, researchers have accomplished encouraging results in the localization and tracking of MNRs through US imaging. In 2014, Misra and coworkers demonstrated that point-to-point control of a magnetic sphere (100 μm in diameter) could be achieved with position feedback control.¹⁴⁷ They reported an average position tracking error about half the microsphere size while navigating it in 2x2 cm arena. The same setup was used for tracking the trail of bubbles (spot size of $\sim 300 \mu\text{m}$) from a single self-propelled microjet *in vitro* with a characteristic length of 50 μm .⁵³ To localize such a small microjet in the imaging plane, they exploited the echogenicity (i.e. characteristics of large wave reflection) of gas bubble trails produced by catalysis-based propulsion. However, the average position tracking error reported in this case was $250.7 \pm 164.7 \mu\text{m}$, about 5 times the characteristic length of the micro-motor. To achieve better performances, in 2018 they developed a model-based tracking system able to achieve ultra-fast localization of millimeter-scale hydrogel grippers from B-mode images with an average position tracking error of $25 \pm 7 \mu\text{m}$ (over one percent the dimension of the gripper).¹⁴⁸ The same group recently demonstrated 3D position control of a magnetic sphere (800 μm in diameter) under US guidance.⁵⁷ To achieve 3D localization with 2D US tomographic images, the transducer was swept along the vertical direction to identify the horizontal plane containing the microrobot. The target plane (2D image) was thus processed by a tracker to extrapolate the remaining two coordinates. Promising results were reported also in *ex vivo* studies where different tasks of millimeter-scale robots were monitored through US images. Qiu and coworkers exploited US images for the localization of a helical propeller (characteristic length of 2 mm) moving in rat liver.¹⁴⁹ Cappelleri and coworkers used US imaging to monitor a sub-millimetric tumbling microrobot capable of releasing the therapeutic payload in the dissected colon.¹⁵⁰ Sitti and coworkers used US images to visualize the multimodal locomotion of a milli-robot within *ex-vivo* chicken tissue.¹⁸ However, none of these microrobot was smaller than 800 μm .

Recently, US imaging has been successfully employed in microrobot swarm tracking.¹⁵¹⁻¹⁵³ Due to their enhanced area density, swarms of microrobots have shown very good contrast properties.¹⁵⁴ In 2018, Zhang and coworkers reported the controlled

navigation of a rotating colloidal swarm of paramagnetic NPs in a centimeter-scale arena. They found the dynamic equilibrium conditions of the swarm produce periodic changes in their contrast. These changes can be used to discriminate the swarm from other elements in the image. In addition, they demonstrated how the centripetal forces of the rotating swarms can be exploited to trap tunable concentrations of contrast agents (e.g. microbubbles) in their cores.¹⁵⁵ This feature can be exploited to further enhance the contrast properties of microrobotic swarms under US imaging. The same group also exploited US images to localize swarms of microrobots *ex vivo* in the bovine eyeball and swine bladder.^{58,156} In more recent study, a swarm of magnetically-coated sperm cells (so-called IRONSperms) was detected under US feedback and showed efficient localization.¹⁵⁷

Disclaimer:

Parts of results presented in this chapter have been published in ACS Nano with the following permissions.

“Reprinted with permission from [A. Aziz, S. Pane, V. Iacovacci, N. Koukourakis, J. W. Czarske, A. Menciassi, M. Medina-Sánchez and O. G. Schmidt, “Medical Imaging of Microrobots: Toward In Vivo Applications” ACS Nano, 14 (9), 10865-10893, 2020]. Copyright [2019] American Chemical Society.”

3 MATERIALS AND METHODS

3.1 Fabrication of Magnetic Micropropellers

3.1.1 3D Laser Lithography of Polymeric Resin

Micromotors were fabricated using a 3D laser writing tool (Photonic Professional GT, Nanoscribe GmbH, Germany) based on the principle of two-photon polymerization or absorption (TPA). TPA is the highest resolution 3D printing technique¹⁵⁸ that allows direct laser writing of microstructures with a resolution of ~ 200 nm. The main advantage of this tool is the fabrication of pre-defined or programmed shapes intended for specific applications. TPA is a non-linear optical process predicted by Goeppert-Mayer¹⁵⁹ in the 1930s and demonstrated by Kaiser in 1961 after the invention of the laser.¹⁶⁰

In this process, one molecule simultaneously absorbs two photons to reach to the excited state from the ground state. The maximum absorption occurs at the focal point of laser light and the size of this area depends on the laser power and spot size and also on the properties of the resist material. The basic principle of TPA is described somewhere else,¹⁶¹ where a molecule is excited from the ground state to an excited state located with energy above the ground state by absorbing two photons. After excitation, the system relaxes quickly and returns to the ground state by undergoing radiative or nonradiative processes. By precisely scanning the laser focus spot throughout the printing material, a 3D extended volume can be polymerized, within the spatial resolution of the moving stage. Afterwards, similar to any other photolithographic process, the chemical difference between exposed and unexposed regions leads to selective etching inside a suitable developer.

Briefly, pure quartz glass substrates (25x25 mm²) were washed and ultra-sonicated (Elmasonic, Elma Schmidbauer GmbH, Germany) in acetone and in isopropanol, and finally dried with N₂. On these substrates, dip-in laser lithography photoresist (IP-Dip, Nanoscribe GmbH) was drop-casted as the basic polymer material for laser writing. In the process, the negative-tone photoresist was locally patterned by two-photon induced polymerization with NIR ultrashort pulse laser (≈ 100 fs, 780 nm) in a defined

focal spot volume (voxel). The exposed feature was first designed with CAD software (AutoCAD, Autodesk), and exported as an .stl file to be read by the Describe software. Based on the initial CAD-based feature, arrays of the different geometries were fabricated with reproducible dimensions. The slicing distance was set at max. $0.5 \mu\text{m}$ with a hatching distance of $0.25 \mu\text{m}$. After laser writing, the samples were developed in mr-Dev 600 (Micro Resist Technology GmbH) for 20 min and washed in isopropanol for at least 3 min. The samples were kept in isopropanol and transferred to a critical point dryer (CPD, Autosamdri-931, Tousimis Research Corporation) to remove the liquid and to obtain dry arrays of upstanding polymeric tubes on the quartz glass (**Figure 3.1**).

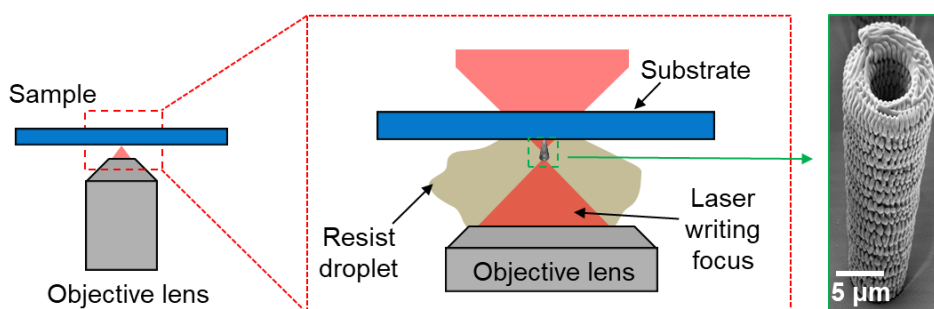


Figure 3.1. 3D laser writing with two-photon absorption.

3.1.2 Self-assembly of SiO_2 Particles

Reflective micromotors were fabricated via a drop-casting method and subsequent metallic layers deposition. In detail, glass substrates ($25 \times 25 \text{ mm}^2$) were rinsed and ultra-sonicated (Elmasonic, Elma Schmidbauer GmbH) in acetone first and then in isopropanol, and finally dried in a stream of N_2 . The glass slides were further treated with oxygen plasma, leading to the removal of impurities and contaminants from the surface (Diener electronics), to obtain clean and hydrophilic substrates. Next, a monolayer of micro-sized ($\varnothing = 100 \mu\text{m}$ and $20 \mu\text{m}$, Corpuscular Inc. USA) silicon dioxide (SiO_2) particles was self-assembled, using the drop-casting method. SiO_2 particles were washed with methanol and centrifuged for 1 min to remove supernatant and then again mixed with methanol and well mixed them prior to drop-casting. The micro arrays were randomly formed in the direction of solvent evaporation. Silica particles were mixed thoroughly in methanol and $\sim 20 \mu\text{l}$ of the particle-solvent solution was drop-casted on the edge of the pre-plasma treated glass slide. The glass slide was adjusted at an angle to allow the spreading of silica particles over the entire glass coverslip, making a homogeneous monolayer of silica particles. The resulted monolayer was dried at room temperature and spacing among SiO_2 particles was controlled by

tuning the solution concentration (**Figure 3.2**). The samples were coated with metal layers of high purity (99.995%) by electron beam physical vapor deposition (e-beam evaporator, Plassys MEB550S).

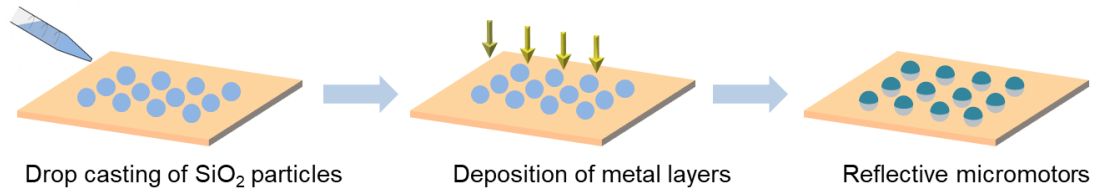


Figure 3.2. Fabrication process of reflective micromotors ($\varnothing = 100 \mu\text{m}$ and $20 \mu\text{m}$) after deposition of metal layers (50 nm Au, 10 nm Ti, 30 nm Fe and 50 nm Au).

3.1.3 Electron Beam Evaporation

Electron beam (e-beam) evaporation is a physical vapor deposition (PVD) method to coat thin metal films by anisotropic condensation of material on the surface of the sample. The target material is vaporized by heating a solid source by electron bombardment at high vacuum pressures. The advantages are nearly anisotropic deposition and the comfortable handling of the device. The target material is placed into a crucible which can be mounted into a water-cooled hearth. A thermionic filament is used as a source of electrons accelerated at 5 kV high voltages by the anode and focused on the target by magnetic fields. The target material is heated up by the transfer of the kinetic energy of the high energy electrons striking the target material. After reaching the melting point of crucible material it evaporates with its specific vapor pressure and evaporation rate.^{162–164}

The vacuum chamber contains the evaporation unit at the bottom, a shield with a window facing the thickness monitor, an oxygen gas pipeline, a shutter, and the substrate holder. The shield protects the machine and slightly collimates the evaporated material. The thickness monitor is a quartz crystal microbalance (QCM) measurement device and can detect the current deposition rate for all used materials. The thickness monitor has not the same orientation and distance to the material source as the substrate and therefore, a so-called tooling factor for each material has to be calculated to adjust the displayed thickness on the QCM monitor to display an accurate value of the deposited thickness. Spherical reflective micromotors (20 and 100 μm in diameter, for experiments in Chapters 4 and 0) and tubular micromotors (25–100 μm in length, for experiments in Chapter 5) were fabricated.

In the second step, an e-beam evaporator was used to deposit thin metal layers of different materials (e.g. Ti, Fe, Au) onto the substrate. Iron (Fe, 30 nm) layer was

evaporated for magnetic guidance, and Titanium (Ti, 10 nm) was chosen as an intermediate adhesive layer sandwiched between gold and iron layers. To obtain reflective micromotors, the sample was coated from one side maintaining the sample holder at 0° and the deposition rate was adjusted between 0.5-1.0 Å/s. SEM and optical microscopy images show the metal-coated micromotors (**Figure 3.3**).

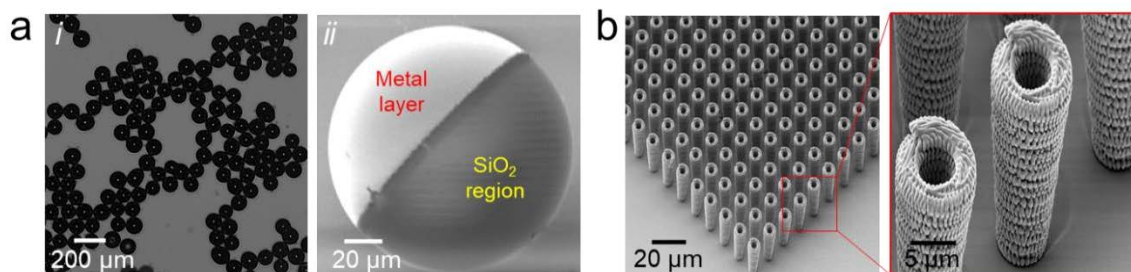


Figure 3.3. a) Bright-field microscopy image of monolayer of metal coated (Au/Ti/Fe/Au) spherical micromotors (i) and SEM image of single micromotor showing the interface of silica region and evaporated metal layer surface (ii). b) SEM images of an array of 3D printed microtubes after subsequent metal coating (Cr/Ni/Ti). Figure modified from refs.^{165,166}

3.1.4 Surface Functionalization

In this sub-section, we describe the labeling of commercially available AuNRs to the outer surface of 3D printed microtubes and thereby enabling strong PA signal (for experiments in Chapter 5). To do so, the surface chemistry method was conducted after 3D printing of microtube arrays. Thin metal layers were deposited using electron beam evaporation. Thin Fe layer provides external magnetic control and Ti offers good biocompatibility. Al_2O_3 is used as a top layer to aid surface functionalization and is biocompatible.

Carboxyl-modified AuNRs (Nanopartz Inc., USA) were immobilized on the surface of the microtubes implementing a protocol based on ((3-aminopropyl) triethoxysilane) (APTES) and carbodiimide chemistry.¹⁶⁷⁻¹⁶⁹ Briefly, the outer tube material (Al_2O_3) was activated by oxygen plasma (50 s) to create hydroxylic groups onto the surface. Meanwhile, 2% APTES solution was prepared with 5% DI water and 93% ethanol and the microtubes were transferred to the APTES solution after plasma activation. In the presence of APTES, having silane groups in one side and the amino groups on the other side, the silanes were conjugated to the hydroxylic groups of the micromotor surface. The amine groups were exposed from the other side and were then bonded to the carboxylic groups of the AuNRs, by EDC-NHS chemistry after incubating for 1 hour at room temperature. The samples were washed afterwards with ethanol and then with PBS.

Then, N-ethyl-N-(3-dimethylaminopropyl) carbodiimide hydrochloride (EDC) at a concentration of 10 mM, and active ester compound N-hydroxy-succinimide (NHS) at a concentration of 5mM, were used for coupling the carboxyl groups from the AuNRs to the amino groups from the outer surface of microtube, forming covalent bonds (during 2 h at room temperature). Finally, the samples were washed with PBS and DI water for further experiments. Each sample was prepared (for experiments in Chapter 5) with a different concentration of AuNRs (75, 150 and 300 $\mu\text{g}/\text{mL}$), which resulted in three final densities (40, 64 and 96 AuNRs/ μm^2) as displayed in **Figure 3.4**.

This linker chemistry leads to covalent bonding between the microtube surface and the AuNRs. The carbodiimide 1-ethyl-3-(3-dimethylaminopropyl) carbodiimide (EDC) is a zero-length cross-linking agent that reacts with a carboxyl group of a biomolecule, forming an amino group of a biomolecule. EDC has the advantage of water solubility which allows direct bioconjugation without prior organic solvent dissolution. The primary amine N-hydroxy succinimide (NHS) is used to stabilize the reactive ester-intermediate and form the amide bonds.^{169,170} This protocol chemistries allow all kinds of molecules (e.g. antibodies, enzymes, fluorophores, or DNA) to attach the NPs or nanorods surface without prior modification.

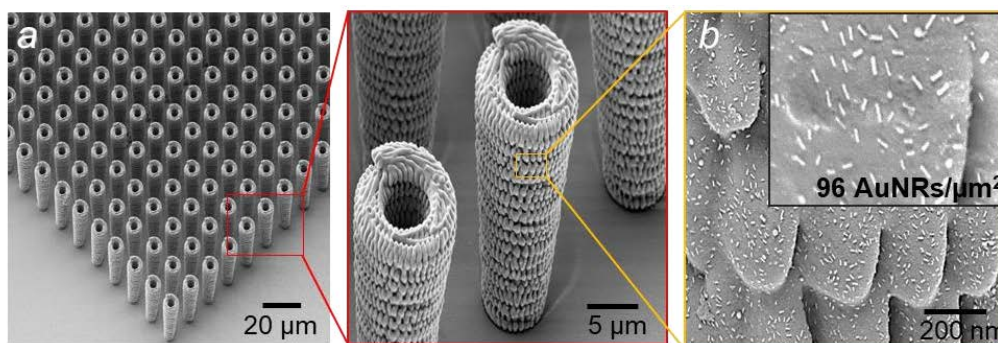


Figure 3.4. a) SEM images of 3D printed microtubes before functionalization of AuNRs on the outer surface (a) and high magnification SEM image (b) after functionalization with AuNRs 96 AuNRs/ μm^2 . Figure modified from ref.¹⁶⁶

3.2 Fabrication of Phantom Tissue and Microfluidic Channels

3.2.1 Fabrication of PDMS-Glycerol Phantom

The fabrication of PDMS-Glycerol phantoms has been explained in detail elsewhere.¹⁷¹ The phantoms were prepared freshly, and the thickness was controlled by the Vernier caliper. We describe the phantom fabrication procedure and the materials that make

up the phantom. Briefly, the two components of silicone elastomer polydimethylsiloxane (PDMS) (Dow Corning GmbH, Germany) were mixed together in a volume ratio of 10:1 (elastomer: curing agent). Then, glycerol (Sigma-Aldrich GmbH, Germany) with a concentration of 0.5 parts per volume was added carefully by avoiding the excessive number of air bubbles. The mixture was well mixed and poured into Petri dishes (Henke Sass, Wolf GmbH) with controlled thicknesses (for IR reflective imaging) and poured into 20 mL syringes (for photoacoustic imaging). Air bubbles were removed from the mixture using a desiccator, and the mixture was left at room temperature to solidify for 24 hours. **Figure 3.5a** shows an absorption spectrum (green curve) of PDMS-glycerol phantom with a thickness of 1 cm.

3.2.2 Fabrication of Agarose Phantom

Agarose is a cost-effective bacteriological powder that, when dissolved in water, remains in a gelatinous state in ambient temperature after being warmed-up. Agarose phantoms mimic soft tissues and some preparation techniques are described in literature.^{172–174} The dry agarose was weighed out and then dissolved in distilled deionized water. Briefly, 100 ml DI water was heated at 300 °C and 1.50 g of agarose (Fluka, Germany) was slowly added and gently mixed forming a homogeneous solution. The agarose solution was heated on a hotplate with magnetic stirring. Then, 6 ml soya milk (Alpro, UK) was added to introduce tissue-mimicking scattering properties in phantoms. After adding milk, the solution was mixed well during heating and 10-15 ml of this hot solution mixture was poured into a plastic syringe (used as a mold) with a diameter of 2 cm (**Figure 3.5b**).

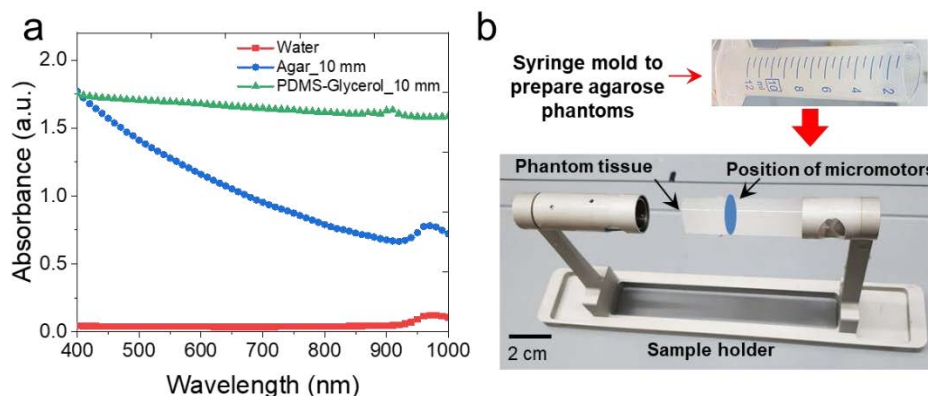


Figure 3.5. a) Absorption spectrum of water, agarose and PDMS-glycerol phantom tissues with a thickness of 1 cm. b) Syringe mold with solidified agarose and then transferred to sample holder.

The solution was left to cool down at room temperature for ~ 30 min to solidify into a gel. The syringe was filled sealed with a thin parafilm sheet to prevent evaporation. The solidified agarose gel was then taken out of syringe mold and carefully placed in a sample holder for PA imaging

3.2.3 Phantom based on *Ex vivo* Tissues (Chicken Breast and Mice Skull)

Chicken breast samples were purchased from a local store and used with thicknesses of 5 and 10 mm. A millimetric channel (~3 mm) was realized from the agarose phantom by inserting a straw during solidifying process. This channel containing micromotors as a fluidic platform was placed on top of 5- or 10-mm thick chicken breast tissue (for experiments in Chapter 5) for the PA study of micromotors (**Figure 3.6a**). A transparent intravascular polyurethane (IPU) tubing (inner diameter ~380 μm and outer diameter ~840 μm , SAI Infusion Technologies, USA) as a fluidic channel for dynamic tracking experiments. The IPU tubing was filled with the micromotors suspended in 1x PBS and then placed between two layers of 5 mm thick chicken breast tissues (**Figure 3.6b**). The process was repeated for 10 mm thick tissues afterwards (for experiments in Chapter 6).

To ensure uniform distribution of thickness and prevent from drying, the thickness of the tissue samples was measured using a digital Vernier Caliper. The tissues containing micromotors were then placed on an imaging chamber grid for tracking measurements.

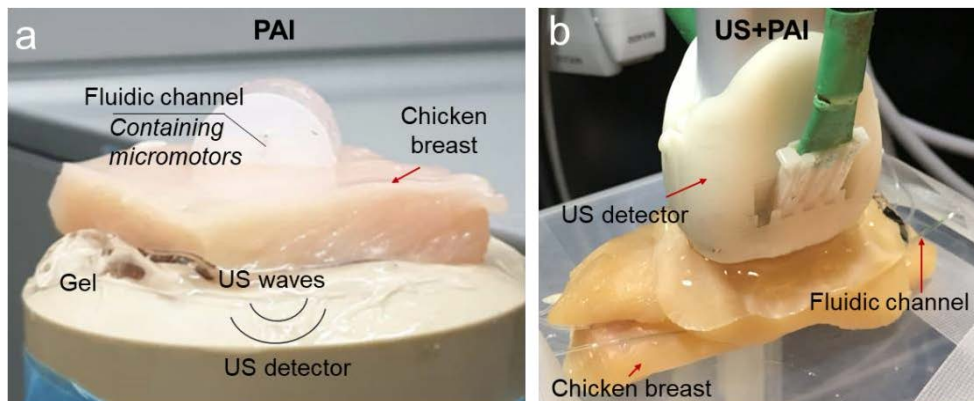


Figure 3.6. *Ex vivo* chicken breast tissue platform for different imaging systems; a) PA setup and b) Hybrid US and PA imaging system.

The mice skull tissues were obtained from the Mortensen Lab at the University of Georgia in Athens, USA and used in accordance with care and use of laboratory animals. All mice were anesthetized before sacrificing using O_2 gas flow mixed with isoflurane. The hair over the scalp was removed using hair removing cream. An

incision was made on mice brain and the skull tissues were removed immediately after sacrificing the mice.

The mice were decapitated after euthanizing with CO₂, the skin and periosteum were removed and fixed in 2% PFA for 2 days. The top part of the skull was cut using a dental drill and washed with PBS to removed unwanted tissues. The samples were mounted in agarose gel (**Figure 3.7**) to maintain their optical properties. The thickness of the skull tissues was estimated from laser triangulation measurements. The skull tissues were carefully removed from the agarose gel prior to use and placed in phosphate-buffered saline (PBS) to prevent dehydration. First, the micromotors (100 μm) were injected into the fluidic channel and aligned by using external magnetic fields.

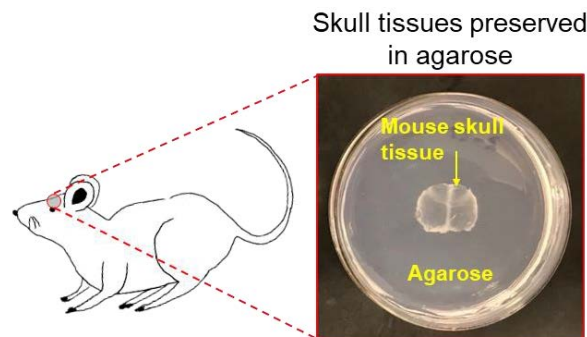


Figure 3.7. *Ex vivo* mice skull tissues preserved in agarose gel.

3.2.4 Microfluidic Channel Platform

Two kinds of microfluidic channels were fabricated and used in this work. First, glass-based channel was prepared by using double-layer parafilm sheets that allowed the tracking of the reflective micromotors in a confined transparent space. A glass slide (75x26x1 mm) and a coverslip (60x26x0.15 mm) were sonicated in acetone and isopropanol for 3 min each. The parafilm stripes were placed between the glass slide and coverslip and melted at 120°C to fasten the three parts together, resulting in an enclosed channel (**Figure 3.8a**).

In order to measure fluid viscosity in the vascular network, it is important to consider the influence of the confinement on the micromotor hydrodynamics. For that, we fabricated a microchannel with a blood vessel mimicking network, with three different widths 100, 50, and 25 μm , all with a height of about 50 μm (**Figure 3.8b**) (for experiments in Chapter 4). To fabricate the channel, a SU-8 mold was prepared on a 4-inch Si wafer and then a mixture of PDMS was poured into the mold. Air bubbles

were removed from the mixture using a desiccator, and the mixture was left at room temperature to solidify for 24 hours.¹⁷⁵

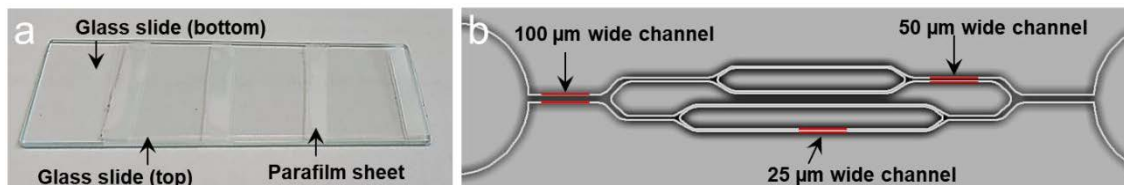


Figure 3.8: a) Microfluidic channel platform b) Schematic of a PDMS microchannel mimicking blood vessel network.

3.3 Sample Characterization

3.3.1 Optical Microscopy

Optical or light microscopes commonly utilize visible light, and a series of lenses to generate magnified images of small objects. The sample is placed on the 3D stage and viewed directly through the eyepiece by using a suitable objective lens or typically a camera is used to capture the image. The sample can be illuminated with light coming through (bright-field mode) or around the lens (dark-field mode). Different objective lenses with varying magnifications are used mounted on a turret providing an ability to zoom-in. In this work, optical microscopy was performed using an optical microscope (Zeiss Microscopy GmbH) equipped with 5x, 10x and 20x objective.

3.3.2 Scanning Electron Microscopy

Scanning electron microscopy (SEM) is an electron microscope that uses a focused beam of electrons to form images instead of light. The electrons interact with atoms in the sample, forming various signals that reflect the surface morphology and composition of the samples on the micro-/nano-scale. The resulting signals include backscattered electrons (BSE), secondary electrons (SE), absorbed current, and so on. Among them, the SE signal is frequently used.¹⁷⁶ The achievable resolution of SEM is less than 1 nm.¹⁷⁷

In this thesis, Zeiss Nvision 40, Carl Zeiss Microscopy GmbH (for experiments in Chapter 5) and Zeiss DSM982 (for experiments in Chapters 4 and 0) devices were utilized for the morphology characterization. Prior to SEM, the samples were coated with ~10 nm Pt thin layer to make the specimen conductive and to avoid charging effects during imaging.

3.4 Magnetic Actuation

Tethered and untethered microdevices, to perform noninvasive or minimally invasive diagnosis and therapy or other medical tasks, are actuated by magnetic,¹⁶ optical,²³ acoustic,²⁰ or electrical fields,¹⁷⁸ among others. Achieving remote control over an autonomous system is a crucial requirement for its implementation in a desired medical task. Most of them are usually controlled and/or guided by a magnetic field with precise localization and tracking to perform the intended functional tasks. Compared with optical, acoustic, or electrical fields, actuation using the magnetic field has the advantages of high precision, deep tissue penetration, and large force output.¹⁷⁹ Magnetic fields also offer a great way to control a system in a biocompatible and non-invasive way. In this thesis, we have implemented the magnet field gradient, to guide and drag the micromotors, and customized Helmholtz coil setup, for rotational and translational movement of magnetic micromotors.

3.4.1 Magnetic Force

The magnetic force on a particle in a magnetic field is determined by its induced magnetic moment and the gradient of the magnetic field:

$$\mathbf{F} = \nabla(\mathbf{m} \cdot \mathbf{B}) \quad (3)$$

where \mathbf{F} is the magnetic force, \mathbf{m} is the magnetic moment and $\nabla\mathbf{B}$ is the magnetic field gradient. The induced magnetic moment depends on the magnetic permeability of the material (μ), flux density (\mathbf{B}) and volume of magnetic material (V).¹⁷⁹

In experiments, to generate the magnetic field gradient, a permanent neodymium magnet was used and the magnetic field strength was estimated using the Hall sensor by positioning the magnet with respect to a sensor over a distance of 0-3 cm (**Figure 3.9a**).

3.4.2 Magnetic Torque

While in a rotating magnetic field, the magnetic torque experienced by a particle aligns itself toward the direction of magnetic flux density, and the direction of the magnetic flux density \mathbf{B} changes as given below:

$$\boldsymbol{\tau} = \mathbf{m} \times \mathbf{B} = mB\sin \theta \quad (4)$$

where ‘ θ ’ is the angle between \mathbf{m} and \mathbf{B} and $\sin \theta$ reaches a minimum when \mathbf{m} and \mathbf{B} are aligned and it becomes maximum when \mathbf{m} and \mathbf{B} are perpendicular to each other. Large field strength is required to increase the magnetic torque on the particle and, in this case, magnetic particles made of the permanent magnet are used.¹⁷⁹

To explain the basic principle of rolling, the micromotors were half-coated with a thin Fe layer and a uniform in-plane (x-y) rotational magnetic field at 5 Hz and an out-of-plane magnetic field result in rolling and translation using a custom-made setup of three orthogonal Helmholtz coils. These coils were used to generate a rotating magnetic field with homogeneous magnetic field strength of ca. 3 mT to actuate the Au/Ti/Fe/Au-coated micromotors. The setup was designed and built in-house to fit our needs in terms of working space, rotational frequency and field amplitude modulation. To achieve real-time visualization of micromotors, the external magnetic field setup was placed on the observation platform which is compatible with our IR imaging system (**Figure 3.9b**) and optical microscope (AxioTech Vario, Carl Zeiss Microscopy GmbH) to observe them.

To actuate the micromotors in the working space of the Helmholtz setup, they were collected from the glass substrate by gentle scratching and dispersed in a drop of water or PBS and injected into the customized vascular network or fluidic channel platform made from cut Parafilm sheets as described in Materials and Methods section. These platforms were then placed and mounted onto the sample holder that was used to reach into the working space of the Helmholtz coil setup.

For the performance evaluation of the spherical micromotors, single micromotors were actuated to move along a defined, rectangular track or any desired trajectory (e.g. IFW logo, **Figure 3.9c**) while being observed and captured in real-time under the IR imaging setup. Several tracks with modulated parameters were captured using a single moving micromotor. The yellow arrows represent its moving direction from the beginning to the end. This magnetic system can be used to actuate the micromotors on different tracks or trajectories.

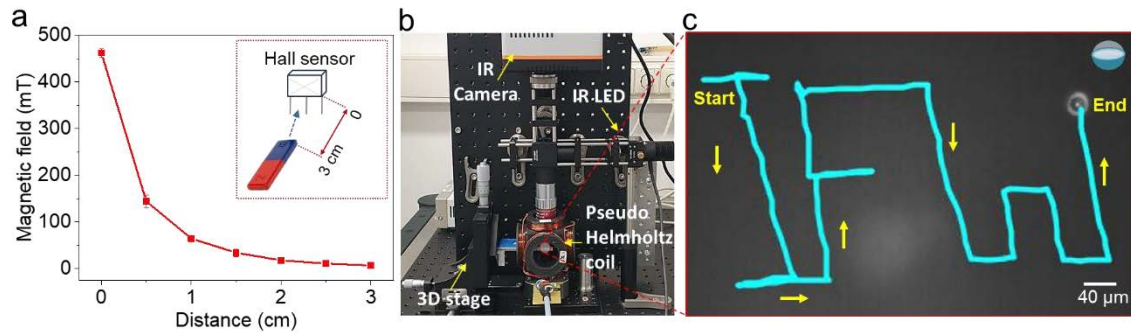


Figure 3.9. a) The magnetic field gradient was measured using Hall sensor at different distances for dynamic imaging studies. b) Helmholtz coil setup implemented for the tracking of micromotors. c) Controlled tracking of a single rolling micromotor resulting in IFW logo (yellow arrows represent its moving direction).

3.5 Ethic Statement for Mice Experiments

The *in vivo* mice experiments were conducted at the FUJIFILM VisualSonics laboratory in Amsterdam. The animal protocols used in this work were appraised and approved by the Committee on Ethics in the Use of Animals (CEUA), The Netherlands (Protocol AVD2450020173644). They are in conformity with FELASA guidelines and the National Law for Laboratory Animal Experimentation (Law No. 18.611). The experiments were performed by using the same equipment used for the phantom studies. 12 weeks old mice were used for *in vivo* imaging in bladder and uterus. All mice were anaesthetized using isoflurane, at a concentration of 1.5-2%. O₂ flow (1>2 mL/min maintenance) mixed with isoflurane. For optimized coupling of the ultrasound gel the rodent fur needed to be removed using commercially available depilation cream. For 3D multiplexing imaging, an ICR(CD-1) +/- 25-gram female mouse was injected with a 10 μ L mix of PBS 1X and micromotors into the hind limb (popliteal lymph node fat pad). 3D PA multiwavelength was applied to automatically un-mix the injected micromotors. PA multispectral imaging distinguished the difference in optical signals related to the micromotors in 2D and 3D for subsequent post-processing.

4 OPTICAL IMAGING OF MICROROBOTS

In optical techniques, fluorescence imaging (FI) is a widely used biomedical imaging modality; its working principle relies on the well-known Jablonski energy diagram⁷⁹ which describes the molecular fluorescence from excitation to emission. The process initiates by the absorption of an incoming photon (light source) after exciting the target molecule, followed by the vibrational relaxation of excited state electrons to the lower energy level. Finally, the emission of a longer wavelength photon appears and the excited molecule returns to the ground state. The emission efficiency is reduced after excitation to emission processes and the amount of emitted light is randomly dispersed and collected efficiency reduces. Fluorescent labels emitting in IR decay over time after encountering repetitive excitation processes and ultimately reach the saturation level. Emitted radiations require long acquisition times to collect a fluorescent and insufficient signal for real-time imaging. In the case of QDs, if they agglomerate due to the surrounding proteins or molecules, it could alter their optical properties.

To address some of these limitations, this section will focus on reflection-based imaging of single moving reflective micromotors under scattering tissues as a label-free approach. Reflection-based imaging (RI) describes the image formation by detecting back-scattered or reflected light with single-sided optical access to the specimen. There are various configurations to perform RI, for instance, confocal, interferometry, oblique angle illumination, and total internal reflection allowing different biomedical applications. Such techniques are suitable in body districts where the photon scattering is relatively low. RI does not rely on the emission of a fluorescent probe, but the signal depends solely on the intrinsic reflection or backscattering properties of the sample. Gold (Au) is one of the most suitable materials as it is biocompatible and highly reflective over a broad spectral range.⁷⁰

4.1 Concept of Reflective Micromotors

Transparent silica particles can be converted into micro-reflectors by incorporating a thin gold layer as a biocompatible and highly reflective material.¹⁸⁰⁻¹⁸³ Additionally, if a magnetic layer (Fe) is introduced into the reflective materials, then the position of

the particles can be controlled by external magnetic fields, resulting in magnetic reflective micromotors that can be steered and visualized under IR light. Layers of Au, Ti, Fe, and Au were deposited in series onto a monolayer of silica particles at an angle of 0 degree, leading to a semispherical cavity which is then used for the imaging (**Figure 4.1**).

The gold layer is highly reflective over a broad spectral range⁷⁰ and was chosen as a reflective layer coating half of the micromotor. The metal layers deposited on top of spherical transparent silica particles ($\varnothing = 100 \mu\text{m}$ and $20 \mu\text{m}$), lead to a semispherical reflector to collimate the beam to an appropriate focus for their further visualization. The rear surface, exhibiting the Au/SiO_x interface, acts as a concave spherical mirror and the incident light is reflected back internally through the leading surface of the micromotor and is being redirected back towards the light source.^{184,185} The incident light, reaching the gold-coated surface of the reflective micromotor, eventually reflects back towards the light source along nearly the identical path

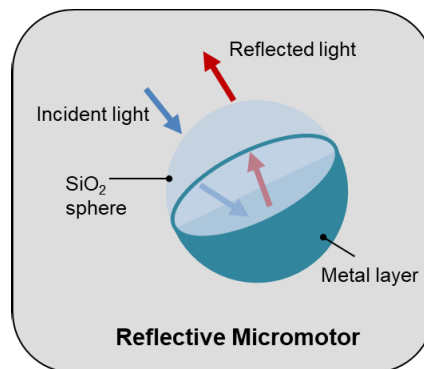


Figure 4.1. Concept of the reflective micromotor fabricated by half-coating silica particles with a metal layer. Figure modified from ref.¹⁶⁵

The reflective micromotors can have different orientation angles (**Figure 4.2a**). We distinguish between the ‘reflector’ (0°), ‘gold particle’ (180°) and ‘hybrid’ (90°) orientation that can be controlled by applying the external magnetic field. The micromotors were illuminated by an LED light source (center wavelength: 970 nm). The illumination source was held perpendicular to a fluidic channel and at different angles to the micromotor reflectors (**Figure 4.2b, i-ii**). The characteristic shape of the micromotor in the ‘reflector’ orientation makes it easy to detect in comparison to a simple spot obtained by the ‘gold particle’ configuration (**Figure 4.2c**). In case of the ‘gold particle’ (same size like the ‘reflector’), the incident light scatters into a broader space angle with a lower signal returning to the detector. The integral over the intensities shows that ~13 times more light is reflected by the ‘reflector’ compared to the ‘gold particle’.

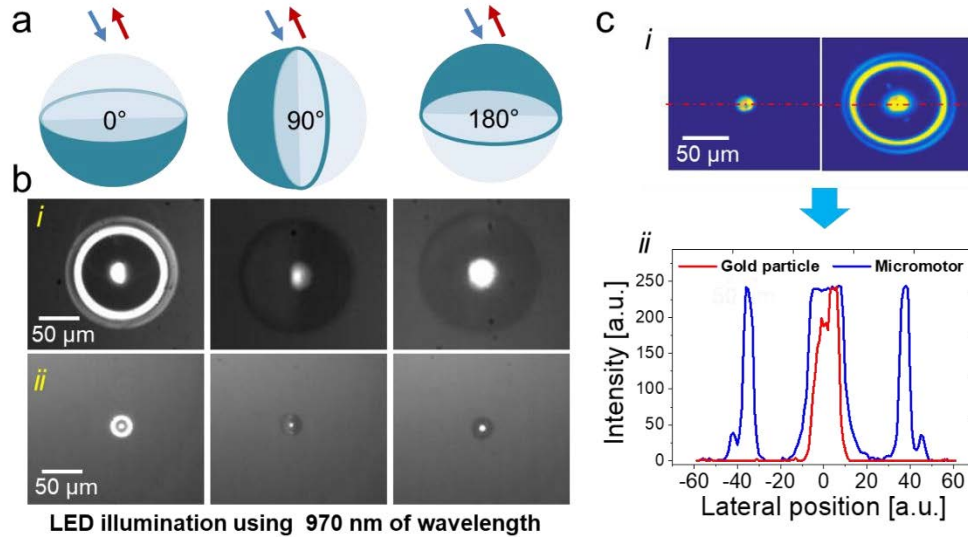


Figure 4.2. a) Schematic of reflective micromotor at different angles and b) Infrared illumination (LED at 970 nm) shows the reflective light from the micromotors in different orientations (0° , 90° and 180°). c) (i) Signal of the 'reflective' micromotor and the 'gold particle' of the same size and (ii) their corresponding signal intensity distributions. Figure modified from ref.¹⁶⁵

4.2 Fabrication of Reflective Micromotors

Reflective micromotors were fabricated via a drop-casting method and subsequent metallic layers deposition as described in Chapter 0. The resulted monolayer of silica particles was coated with Au (50 nm), Ti (10 nm), Fe (30 nm) and Au (50 nm) of high purity (99.995%) by electron beam physical vapor deposition. Iron (Fe, 30 nm) layer was evaporated for magnetic guidance and titanium (Ti, 10 nm) was chosen as an intermediate adhesive layer sandwiched between gold and iron layers. To achieve reflector configuration, the sample was coated from one side, and the sample holder was placed at 0° and deposition rate was set to 0.5 \AA/s . Bright-field image shows a monolayer of metal-coated SiO_2 particles and SEM image shows the asymmetric coating, leading to a semispherical cavity which is then used for the imaging (**Figure 4.3a, i-ii**). Different deposition rates (0.5 to 1.0 \AA/s) were used but no significant effect was observed on the roughness. Atomic force microscopy analysis was carried out to determine the resulting roughness of the deposited metal surface (**Figure 4.3b**). The roughness within a $1 \mu\text{m}^2$ area was calculated by the root mean square ($R_q = 1.62 \text{ nm}$) and the maximum height feature ranges from -5 to 5 nm. Ideal reflection occurs on a surface with a roughness value of zero but in real cases, the reflected light possesses different path lengths due to reflection from different height locations, leading to diffuse reflection¹⁸⁶ and interference of the reflected light. The measured roughness

(1.62 nm) of the gold surface is approx. 0.17 % of the used wavelength (975 nm) and hence guarantees a sufficiently good reflectivity.

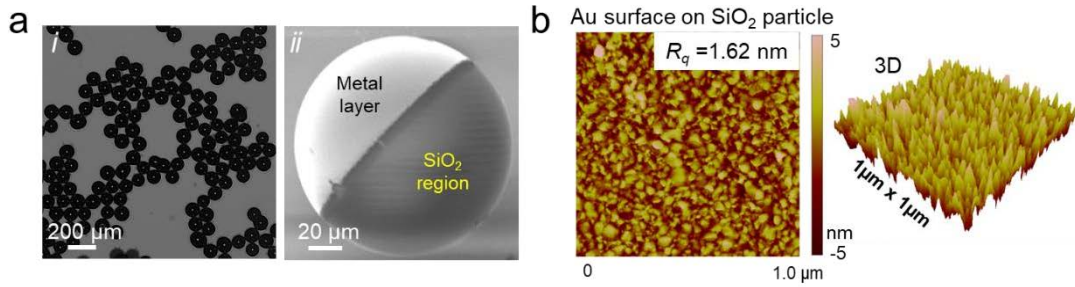


Figure 4.3. a) Bright-field microscopy image of monolayer of metal coated micromotors (i) and SEM image of single micromotor showing the interface of silica region and evaporated Au layer surface (ii). b) Surface morphology and the roughness in 2 and 3D cross section was calculated by the root mean square ($R_q = 1.62 \text{ nm}$) of $1 \mu\text{m}^2$ area and the maximum height feature was measured ranging from -5 to 5 nm.¹⁶⁵

4.3 IR Imaging Actuation Setup

A straightforward approach is adopted by using IR high-power LED (970 nm, Thorlabs, Germany) to illuminate the micromotors with and without scattering phantoms. The IR light is collimated and directed towards the fluidic channel by the aid of an objective lens (Mitutoyo 20x, Edmund optics) as shown in **Figure 4.4a**. An InGaAs camera (900-1700 nm, Xenics Belgium) is used for image acquisition and a home-made C++ code is implemented to drive the camera and to directly process the data by subtracting the scattering background and using image correlation-based algorithms to track the micromotors **Figure 4.4b**.

In cooperation with TU Dresden (Prof. Jürgen W. Czarske, Dr. Nektarios Koukourakis and Hannes Radner), the real-time tracking algorithm was demonstrated by implementing a shape detection algorithm. We used image correlation between an ideal concentric spot-ring model and the real signal to recognize the particle position in each frame in real-time. With an increasing phantom thickness, when the characteristic features of the micromotor disappeared in the diffuse background, the 'reflective' micromotor with a characteristic reflection shape (concentric spot-ring geometry) made it easier to track in comparison to the single spot obtained by a simple 'gold particle'. 3D micromanipulator (XYZ) is used to find the lateral position of the particle (X and Y direction) while the Z-axis is taken to readjust the focus position. With increasing thickness of the tissues, the focus position shifts towards the objective, as the optical

path length change induced by the tissues is the product of the local thickness and the refractive index.

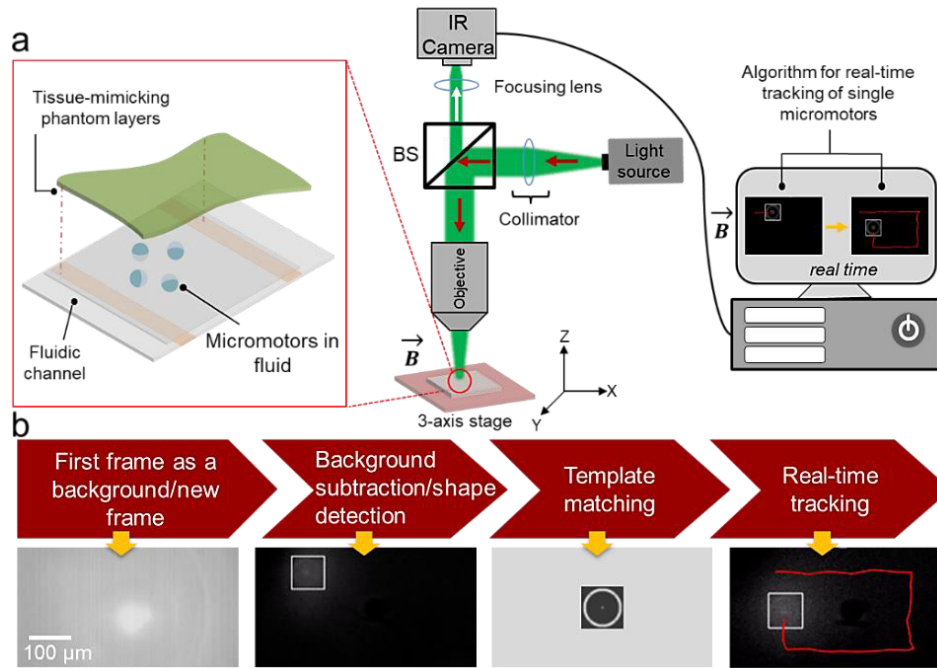


Figure 4.4. a) Schematic of IR imaging setup. b) Flow diagram showing image treatment algorithm and the real-time micromotor detection parameters.¹⁶⁵

Prior to imaging, the micromotors were suspended in DI water ($\sim 10 \mu\text{l}$) and injected into a fluidic channel. The orientation of the micromotors was controlled by an external magnetic field (ca. 20-25 mT). Two sizes of micromotors (100 and $20 \mu\text{m}$ in diameter) were imaged separately with and without scattering phantoms. **Figure 4.5** summarizes the results from the dynamic imaging of the micromotors without scattering phantoms.

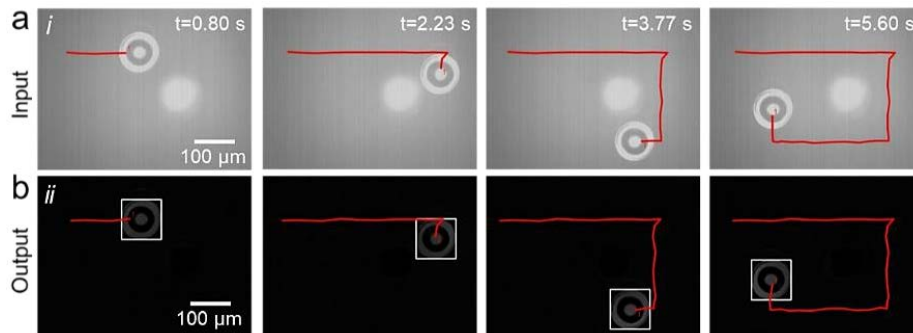


Figure 4.5. Time-lapse images of a single micromotor ($100 \mu\text{m}$ in diameter) tracked in a rectangular trajectory without the scattering phantoms (from 0.80 to 5.60 seconds).¹⁶⁵

Individual micromotors were tracked in real-time in an enclosed channel. Two separate windows indicate the tracking with unprocessed data (input) and with processed data (output, after real-time processing). The complete trajectory of a single micromotor is depicted in the time-lapse images before and after implementing the real-time tracking

algorithm. The central bright spot present in Figure 4.5 is an image of the LED and is part of the light intensity which is present in the system without any object, e.g. induced by internal back-reflections and camera noise. The central bright spot just influences and saturates a small part of the image and is removed with the background intensity suppression real-time algorithm, not affecting the results or the deduced limitations of the presented measurements.

4.4 Actuation and Propulsion Performance below Phantom

The scattering phantoms were fabricated based on a polydimethylsiloxane (PDMS) and glycerol combination (see Chapter 0). In the first set of experiments, $1 \times 1 \text{ cm}^2$ phantoms with thicknesses varying from 0.8 to 2.2 mm were prepared and the micromotors (100 μm and 20 μm in diameter) were tracked below phantom layers. Light from the LED (970 nm) illuminates the phantom tissue. As the light is scattered, a diffused light field illuminates the micromotors. Using laser light would lead to a speckled illumination, meaning that the detected micromotor in 'reflector' orientation would not show its complete characteristic ring shape, but varying arcs. Using LED light, instead, leads to a homogeneous but diffuse illumination and background. The light is reflected from the micromotor and crosses the scattering tissue again. The signal strength collected by the camera depends on the thickness of the phantom tissues. The phantoms only mimic scattering properties of real tissues but their thicknesses do not correspond to the actual biological tissue thickness. This is due to the fact that the phantoms were prepared to be thicker but with less glycerol, maintaining the scattering properties while facilitating their handling for the experiments.

The physical parameters limiting the optical penetration depth in biological tissues are scattering and absorption, represented by the coefficients $\mu_s[\text{m}^{-1}]$ and $\mu_a[\text{m}^{-1}]$ respectively. The scattering phantoms used here have an anisotropy factor of approximately $g=0.975^{171}$ resulting in TMFP=10 mm and MFP=250 μm (**Table 1**).

A maximum LED power density of $\sim 146 \text{ mW}/\text{cm}^2$ for 2.2 mm thick phantom was used. This power density is within the allowed limits of exposure according to International Commission on Non-Ionizing Radiation Protection (ICNIRP) guidelines.⁸¹ Both the 100 and 20 μm micromotors can be clearly distinguished in the processed images up to 1.8 mm thick phantom **Figure 4.6,a-b**. The increased scattering for increasing phantom thickness is documented by increased lateral spreading of the intensity at the camera. For 2.2 mm thick phantom, the characteristic features of the micromotors cannot be distinguished. However, the high reflectivity of the micromotors still leads

to a strong but diffusive signal that moves with the particle still enabling its tracking. Due to rotational symmetry of the diffuse light, the lateral position can be securely detected. The axial position, however, is determined with higher position uncertainty. Using intensity or contrast analysis may help to improve.

The intensity profiles of the 100 and 20 μm micromotors at varying thicknesses of the scattering phantoms are displayed in **Figure 4.6,c-d**. As the light power illuminating the micromotors is kept constant, mainly two effects that change with the phantom-thickness contribute to the detected signals. First, with increasing the scattering-phantom thickness the reflection efficiency of the micromotors is slightly reduced as the illumination takes place at a larger angular range. Secondly, the amount of scattering increases with phantom thickness, changing the intensity ratio between the intensity of the characteristic features of the micromotors and the diffuse signal, which leads to a reduction of the signal-to-diffuse-background ratio (SDBR) (red curve in **Figure 4.6e**). Concurrently, the lateral intensity spreading increases (blue curve).

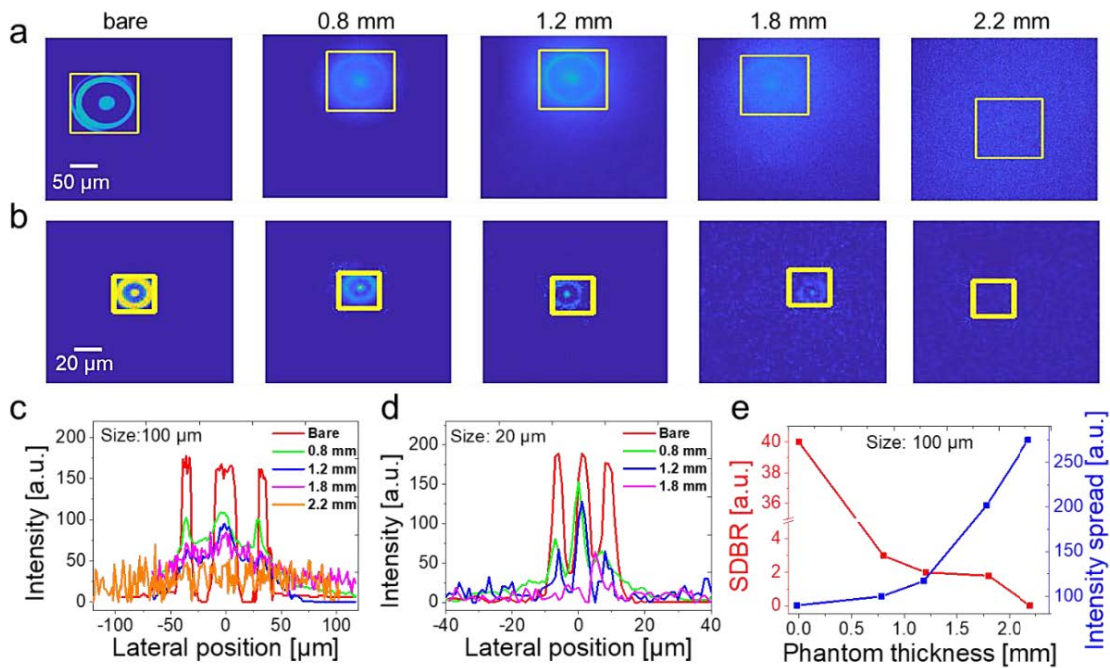


Figure 4.6: Tracking of a single micromotor beneath varying thicknesses of the scattering phantoms (0.8 to 2.2 mm in thickness) for a) 100 μm and b) 20 μm micromotor. c, d) Intensity profiles of the 100 and 20 μm micromotors, respectively. e) The SDBR decreases with increasing the phantom thickness (red curve) and is accompanied by an increase of the lateral intensity spreading (blue curve) due to increased amount of scattering of the diffuse light intensity back-reflected by the micromotors.¹⁶⁵

The characteristic shape of the micromotor is visible up to a thickness of 1.8 mm, which corresponds to $0.18 \cdot \text{TMFP}$. The upper experimental limit for the tracking of the diffuse signal is set by the dynamic range of the camera. The limitation of the imaging

depth is governed by the saturation of the camera by scattered light, which depends on the camera properties like the dynamic range and sensitivity, as well as the employed exposure time, illumination intensity, and the field of view. To probe this limit for our setup and phantoms, the phantom thickness was further increased under varying illumination conditions and the results are shown in **Figure 4.7**. The high reflectivity of the micromotor still enables to detect signals through 3.2 mm thick phantom, corresponding to $0.32 \cdot \text{TMFP}$, whereas at $0.36 \cdot \text{TMFP}$ we only detect noise and this can be observed in the line scans (**Figure 4.7,a-b**). However, the line scans aim to show the limitation, not to really compare the line scans in terms of signal strength. The relative intensity is obtained by dividing the integrated intensity of the background-subtracted images by the integrated background intensity (**Figure 4.7c**). The illumination power was normalized by a simple correction-factor.

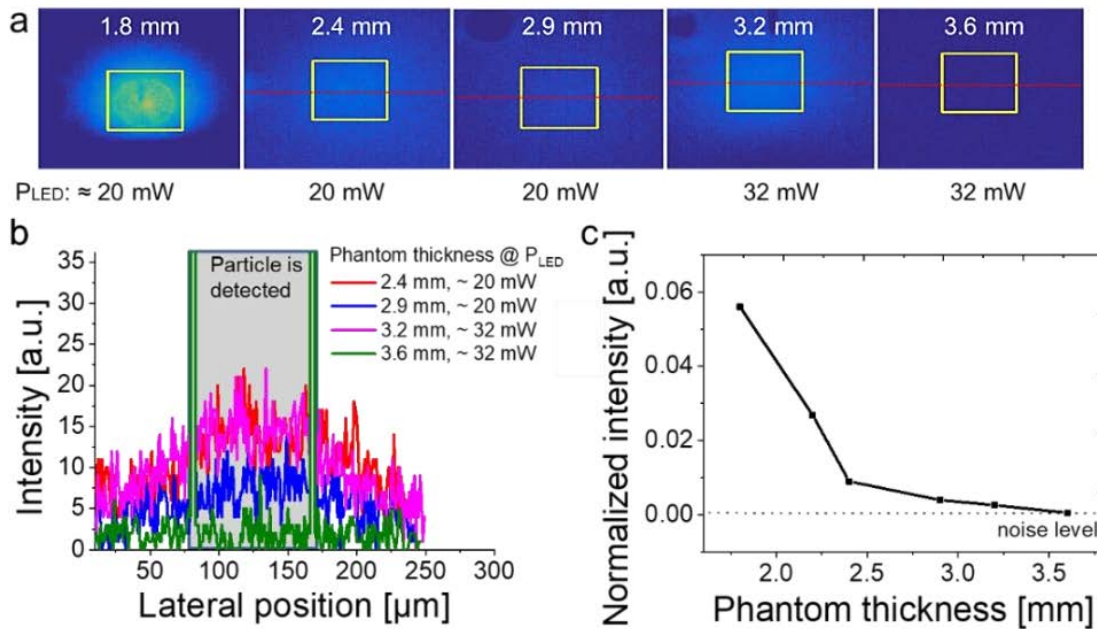


Figure 4.7. Micromotors beneath different phantom thicknesses: a) The micromotor is visible up to a thickness of 3.2 mm and it disappears for 3.6 mm. Note that the illumination power was strongly increased. b) Line scans across the lines marked in red. Up to a thickness of 3.2 mm, a clear signal from the micromotor is detectable, while for 3.6 mm it disappears in the noise. c) The relative intensity is obtained by dividing the integrated intensity of the background-subtracted images by the integrated background intensity.¹⁶⁵

4.5 Actuation and Propulsion Performance below *Ex Vivo* Skull Tissue

The mice skulls were used in accordance care and use of laboratory animals and were taken from 8- and 14-days old mice (see Chapter 0). The thickness of the skull tissues was estimated from laser triangulation measurements. The skull tissues were carefully removed from the agarose gel prior to use, and placed in PBS to prevent dehydration. First, the micromotors (100 μm) were injected into the fluidic channel and aligned by using external magnetic fields. Real biological tissues have an anisotropy factor in the range of $g \approx 0.9$ ¹⁸⁷ and varying reduced scattering coefficients. 2 mm of the tissue-mimicking phantoms used in our studies correspond to 80-220 micrometer of real biological tissues (**Table 1**).

Table 1. Comparison of scattering medium in tissues (phantoms and skull tissues) and various other biological tissues.¹⁸⁷

Tissues	g	(1/mm)	MFP (μm)	TMFP (μm)	0.2 * TMFP (μm)
Skin	0.9	2.44	41	410	82
Brain	0.9	1.07	94	935	187
Breast	0.95	1	50	1000	200
Bone	0.9	1.84	55	545	109
Soft	0.9	0.9	111	1111	222
Fibrous	0.9	1.78	56	561	112
Fatty	0.9	1.34	75	750	150
Skull	0.9	2	50	500	100
Phantoms	0.975	0.1	250	10000	2000

The mouse skull tissues were preserved in agarose gel to maintain their optical properties (**Figure 4.8a**). First measurements were performed through the parietal bone of the skull. The thickness was estimated to be approx. 80 μm for the 8 day and 90 μm for the 14-day skull. The micromotors were visualized underneath skull tissues as shown in **Figure 4.8b**. For both skulls the characteristic shape of the micromotors was clearly visible. As a next step, the skull of the 14-day old mouse was shifted to the frontal bone part, which was estimated to be approx. 110 μm thick. As can be seen, the characteristic shape of the micromotors disappeared due to scattering of the reflected photons through the skull tissues. However, as for the phantom tissues, still enough light is scattered back towards the camera and the position of the micromotor

can be tracked. The characteristic shape of the micromotor was visible up to a tissue-thickness of approx. $0.2 \cdot \text{TMFP}$. **Figure 4.8c** shows the intensity profile of the micromotors ($100 \mu\text{m}$) beneath varying thicknesses of the skull tissues.

Similarly, the smaller micromotor ($20 \mu\text{m}$ in diameter) was captured and there was a moderate change in signal intensity by using the varying thicknesses of the tissues (**Figure 4.8,d-e**). As the smaller micromotors reflect less light, the characteristic shape disappears at $90 \mu\text{m}$ skull tissue.

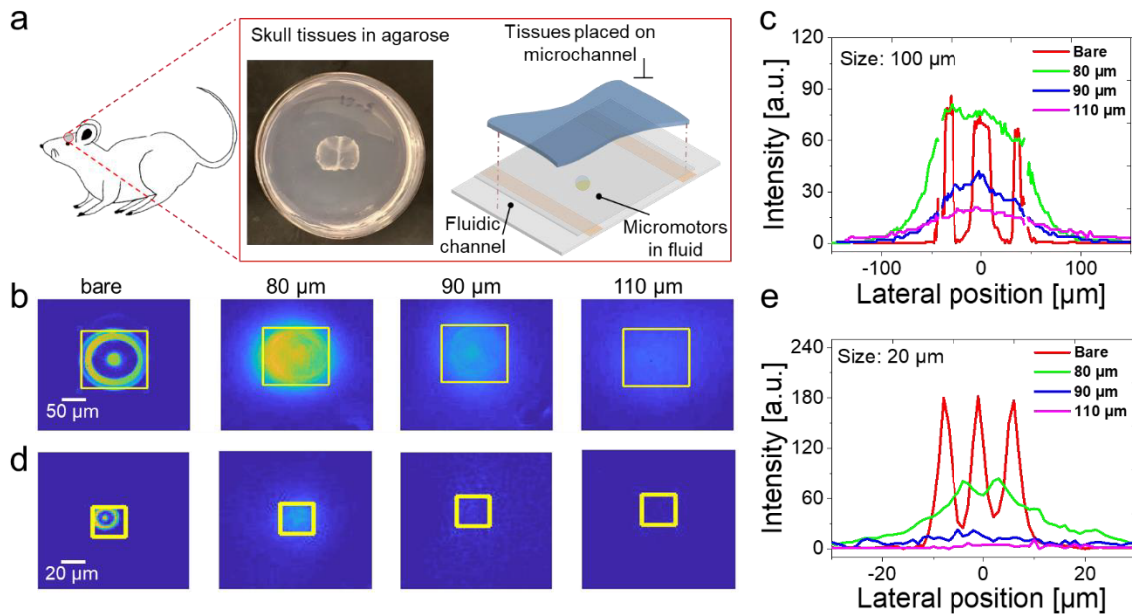


Figure 4.8. *Ex vivo* tracking of single micromotors under mice skull tissues: a) Mouse skull tissue preserved in agarose. b) Tracking of a single micromotor ($100 \mu\text{m}$ in diameter) with varying thicknesses of the mice skull tissues ($80\text{--}110 \mu\text{m}$ in thickness). c) Intensity profile of the micromotors ($100 \mu\text{m}$). d) Tracking of a single micromotor ($20 \mu\text{m}$ in diameter) with varying thicknesses of the skull tissues ($80\text{--}110 \mu\text{m}$ in thickness). e) Intensity profile for $20 \mu\text{m}$ micromotors up to $110 \mu\text{m}$ deep in tissue.¹⁶⁵

4.6 Actuation and Propulsion Performance in Blood

The proposed reflective micromotors hold great potential as remote diagnosis tools, where a biological or physiological parameter can be detected from the outside of the body to determine certain health conditions. An example of it is their use as active rheometers. Fisher's group reported magnetic propellers moved by magnetic field gradients to determine the rheological properties of the vitreous of the eye, where smaller particles (500 nm) were tracked in the complex polymer network.^{188,189}

In this thesis, we also demonstrate the potential application of moving magnetic reflective micromotors as microrheometers to determine the rheological properties of viscous fluids, in particular of blood. This is important to diagnose vascular diseases such as cardio vascular diseases, where blood viscosity is altered.¹⁹⁰ Thus, in this work, an artificial vascular network mimicking the real blood vessels has been developed (**Figure 4.9a**). For this experiment, a rotating magnetic field was applied to steer the micromotors. We found out that the micromotors move more efficiently under rotating magnetic fields, especially when they are in close contact with surfaces as well as in highly viscous solutions. The movement and the corresponding change in the speed of the different micromotors are also presented. However, in order to measure fluid viscosity, it is also important to keep in mind the influence of the confinement on the micromotor hydrodynamics. For that, we fabricated a microchannel with a mimicking vascular network, with three different widths 100, 50 and 25 μm , all with a height of about 50 μm , and as expected when moving the micromotor at 3 mT and 5 Hz, the micromotor speed while moving in PBS was reduced (**Figure 4.9b**). This reduction can be attributed to the increased hydrodynamic resistance of small channels, in particular, the ones close to the micromotor size. Then, the micromotors were also tracked in real cow blood (2x dilution) in different vascular network (**Figure 4.9c**). In a similar fashion, the viscosity of the blood can be estimated towards in situ sensing and diagnosis of vascular diseases by measuring the moving speed of the particle and considering the confined channel widths and the micromotor size.

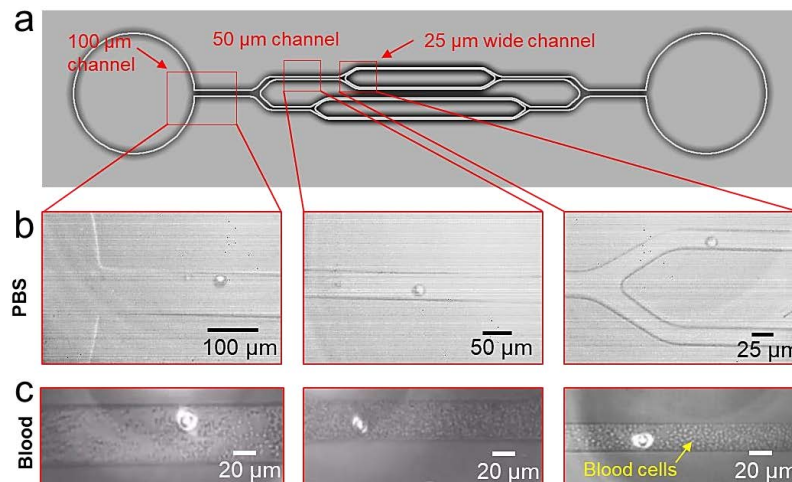


Figure 4.9. a) Schematic of a PDMS microchannel and movement of b) 20 μm particle moving in PBS in different channel sizes. c) 20 μm particle moving in 2x diluted blood. Figure modified from ref.¹⁶⁵

Reflective micromotors (20 μm) can also carry a therapeutic cargo (doxorubicin hydrochloride, DOX-HCL), a model drug which is widely approved for cancer therapy.¹⁹¹ For demonstration purposes, we employed the well-known physical

adsorption method to load drug onto the microparticles. First, we prepared a solution of DOX-HCL at a concentration of 20 $\mu\text{g}/\text{ml}$ dissolved in water, and incubated the metal-coated silica particles in that solution for 24 h, under agitation and at RT. The drug-loaded particles were then washed twice and collected by centrifugation. The drug molecules were adsorbed onto the silica surface as previously reported in the literature.¹⁹² To evaluate the loading and transport of the DOX-HCL loaded micromotors, fluorescence microscopy was used to track single drug-loaded micromotor in the channel with an excitation wavelength of 470 nm (**Figure 4.10,a-b**). It was possible to distinguish drug-loaded micromotors from un-loaded ones (control) using fluorescence microscopy. DOX-HCL possesses an intrinsic fluorescence with an emission peak at around 600 nm. Time-lapse images show the navigation of a drug-loaded micromotor within a microfluidic channel and the potential of drug-loading and transport in a confined vascular network.

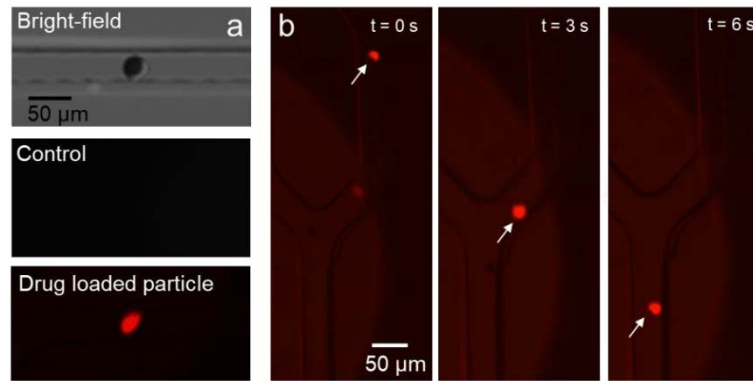


Figure 4.10. a) Bright-field, control, and fluorescence images of DOX-loaded micromotors, and b) the time lapse images of the transported drug-loaded reflective micromotor within the microfluidic network. White arrows show the position of drug-loaded micromotor after different time intervals.¹⁶⁵

The presented imaging approach can still be improved, for instance, using rotational magnetic fields to induce motion through rolling of the reflective micromotors with known frequency and this can be beneficial for extracting additional information about the micromotor positioning and speed in deep tissues by precisely sorting out the background noise from the rotating micromotor signal. Additionally, the usage of an IR wavelength in the second biological window could improve the results due to reduced photon scattering, although LED sources at this wavelength range have commonly reduced power. A change to laser light is also possible, however it leads to a speckled illumination of the particle, which can result in an incomplete ring-shape and consequently in an increase of processing time.

In *in vivo* applications, the scattering tissues will not be static, but will be moving, due to the movement of the animal or simply by changes due to the heartbeat, requiring

continuous calibration steps. This will lead to motion artifacts. A solution could be to track any change induced by the artifacts and counteract with adaptive optics. Commonly, the adaptive optical control should be at least a factor of five faster than the disturbance. Wavefront shaping approaches like digital optical phase conjugation¹⁹³ have been shown to be capable of extending the range of optical techniques into deep-tissue applications of up to several TMFP. They also enable to create minimally invasive needle-sized endoscopes¹⁹⁴ that could be effectively used to get closer to the region of interest.

To conclude this section, we have demonstrated real-time and high-resolution tracking of single 'reflective' micromotors (100 and 20 μm in diameter) through scattering tissues (phantom and *ex vivo* mouse skull), which are key requisites for translating micromotors to clinical applications. The achievable penetration depth in our current setup depends mainly on the camera properties like the dynamic range and sensitivity, as well as on the employed exposure time, illumination intensity and field of view. However, using the high reflectivity of the micromotors enables tracking their movement through phantom thicknesses of up to $0.32 \cdot \text{TMFP}$ (which corresponds to 160 μm of skull tissue). The presented reflective micromotors have the potential to be used as theranostic tools. They can serve as active microrheometers which by analyzing their motion performance within tissues provide information about physiological fluid viscosities possibly associated with a disease status. Moreover, the micromotors can be loaded with drugs and be transported precisely within a microfluidic network through rolling thanks to an applied rotating magnetic field.

Disclaimer:

The results presented in this chapter have been published in *Advanced Functional Materials*.

"Reprinted with permissions from John Wiley and Sons under License Number: **4860851053912** from [A. Aziz, M. Medina-Sánchez, N. Koukourakis, J. Wang, R. Kuszmierz, H. Radner, J. W. Czarske and O. G. Schmidt, "Real-time IR tracking of single reflective micromotors through scattering tissues" *Adv. Funct. Mater.*, 29 (51) 2019]. Copyright [2019] John Wiley and Sons."

5 PHOTOACOUSTIC IMAGING OF MICROROBOTS

Photoacoustic (PA) imaging (PAI), or optoacoustic imaging is a hybrid imaging technique that combines optical excitation and US detection. It has gained rapid popularity for varying biomedical applications in the last two decades. As pure optical methods are limited to sub-skin level or cannot maintain high resolution in deep tissue due to optical scattering, the ability to maintain high resolution optical contrast images in depth of few cm makes PAI a promising tool as it allows real-time imaging in deep tissue,¹²⁹ a resolution in the μm range and molecular specificity. These features are essential for distinguishing the spectral signatures of the micromotors as well as from their cargo (i.e. drugs) from surrounding tissue, which is particularly important for future *ex vivo* and *in vivo* studies.^{99,114,130–132} PAI relies on the excitation of molecules by nanosecond pulsed near-infrared laser light and detection of emitted acoustic waves by highly sensitive ultrasound detectors. When laser pulses are absorbed by tissue, the tissue expands and contracts (thermoelastic expansion), giving off pressure waves that can be detected by ultrasound detectors and accordingly mapped as 2D cross-sectional or 3D volumetric images. These images have high contrast (dependent on the molar extinction coefficient of the absorbers) and high spatial resolution (dependent on the center frequency of the transducer).

5.1 Absorbers for Deep Tissue Imaging

PAI exploits mainly on the intrinsic absorption of chromophores (endogenous i.e. melanin, lipid or Hb/HbO₂ or exogenous i.e. NIR dyes, NPs or metals). Each of these absorbers exhibits its own absorption spectra. However, if endogenous absorbers are not sufficient due to similarity of absorption signals of one or more agents, various exogenous absorbers can be used for better image contrast and targeting in deep tissue imaging. There are few clinically approved contrast agents such as indocyanine green-ICG¹⁹⁵ and methylene blue¹⁹⁶ for PA imaging.

After light illumination, photons can be absorbed with various mechanisms like electronic absorption, vibrational absorption or SPR absorption. Moreover, nanoparticles or molecular chromophores with strong optical absorptivity and

characteristic spectral profiles in the NIR spectral range are preferred due to surface plasmon resonance (SPR) absorption.¹⁹⁷ The oscillations resulted from the charges on the surface of metal NPs, give rise to strong optical absorption properties. NPs can also be directly conjugated with antibodies, cells or peptides. Among various contrast agents,^{109,110} gold nanorods (AuNRs) are excellent candidates due to their unique absorption spectrum which can be tuned across the NIR region by varying their size and shape,^{133,134} and their molar extinction coefficients are much higher than those of endogenous tissue chromophores like water, melanin, and hemoglobin.¹³⁵ **Figure 5.1** shows absorption spectrum of employed agarose phantom and AuNRs with a density of 64 AuNRs/ μm^2 .

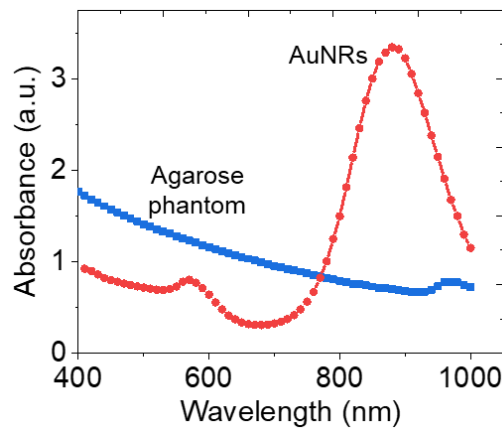


Figure 5.1. Absorbance spectrum of agarose phantom (blue curve) and commercially available AuNRs (red curve) in DI water at a concentration of 150 $\mu\text{g}/\text{ml}$ (64 AuNRs/ μm^2).

5.2 Absorber Micromotor Design and Fabrication

Here, we present the micromotors (labeled with AuNRs) as PA absorbers and, for the first time, the real-time PA tracking of single micromotors in 3D, down to ca. 1 cm deep in scattering phantom and chicken breast tissues. The labelling of AuNRs on the micromotors' surface showed an enhanced PA signal and provided the micromotors with a unique spectral signature, which is of high relevance for distinguishing them from that of the surrounding tissue.

3D printed micromotors (diameter large opening = 12 μm , diameter small opening = 6 μm and different lengths: 25, 50 and 100 μm), were fabricated using two-photon lithography¹⁹⁸ (see Chapter 0). After 3D writing, the samples were developed and the dried samples were coated with Cr/Ni/Ti by e-beam evaporation, Cr improves adhesion and Ni provides controlled magnetic propulsion. To homogeneously

coat the upstanding micromotors, the sample holder was tilted by 15° and rotated at 5 rpm during the deposition process with a rate of 1.5 \AA/s (**Figure 5.2a**).

Afterwards, the structures were covered with Al_2O_3 by atomic layer deposition (ALD) to improve their biocompatibility and to facilitate the surface functionalization with AuNRs. Commercially available AuNRs with an absorption peak around 820 nm and a size of 10 nm in width and 41 nm in length were used for this study. The AuNRs were already covered with a dense layer of hydrophilic polymer that shielded the gold surface and provided long circulation times for *in vivo* applications. The polymer layer also contained carboxyl groups that were used as anchoring points for immobilization on the micromotors. The carboxylic groups of the AuNRs were attached to these amino groups via carbodiimide chemistry (see details in Chapter 3). The density of the attached AuNRs was optimized by functionalizing the micromotors with three different AuNRs concentrations (75, 150 and $300 \mu\text{g/mL}$), which resulted in three final densities (40, 64 and $96 \text{ AuNRs}/\mu\text{m}^2$), after washing as shown in **Figure 5.2b**.

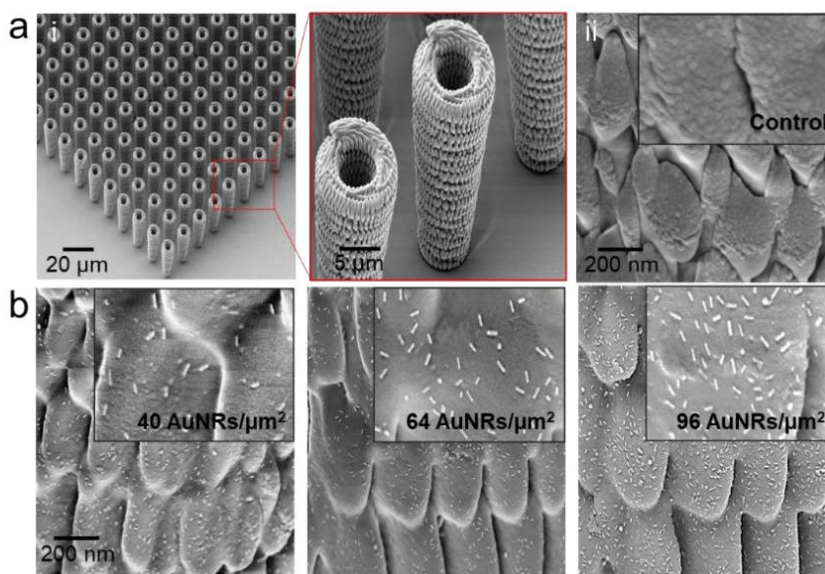


Figure 5.2. a) SEM images of an array of 3D printed micromotors before AuNRs functionalization. b) High magnification SEM images of the micromotors after functionalization with AuNRs (0, 40, 64 and $96 \text{ AuNRs}/\mu\text{m}^2$).¹⁶⁶

The PA signal from static micromotors was recorded from labelled micromotors (with AuNRs densities of 0, 40, 64 and $96 \text{ AuNRs}/\mu\text{m}^2$) as shown in **Figure 5.3**. The measured PA signal intensity was proportional to the areal concentration of AuNRs. It is worth noting that the nonfunctionalized micromotors also absorb light due to patterned metal layers but their resulting PA signal intensity is less as compared to the ones coated with AuNRs.

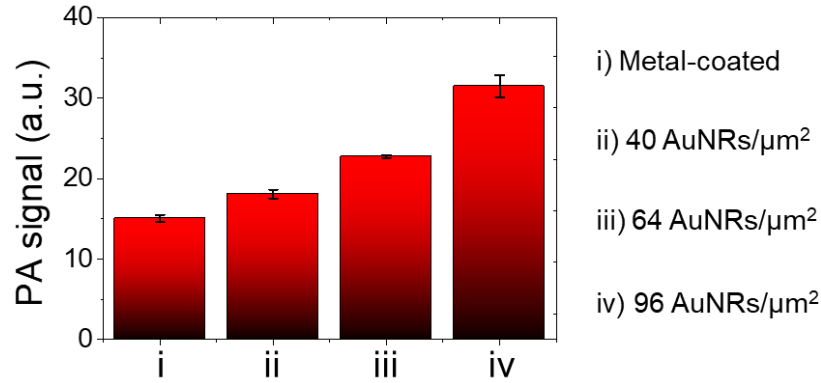


Figure 5.3. PA signal intensity of the AuNRs-coated micromotors embedded in agarose phantom for different densities of AuNRs (0, 40, 64 and 96 AuNRs/μm²).¹⁶⁶

5.3 Photoacoustic Imaging Setup

PAI studies in this section were conducted using an inVision 256-TF small animal scanner, in cooperation with iThera Medical, Munich. Micromotors embedded in phantoms were imaged in static environment and image reconstruction was performed using ViewMSOT (iThera Medical). All images were frequency-filtered from 1.8 MHz to 7 MHz to exclude low frequency distribution from phantom material and were equally scaled with pixel intensities ranging from 0 to 255 arbitrary units (a.u.). ROIs were chosen to measure the PA signal and were placed at the same positions during all measurements.

PAI is based on optical illumination and US detection. A cylindrical tissue-mimicking phantom with a diameter of 2 cm is placed in a holder and submerged in a water tank in a horizontal position around 256 US detector elements. PAI setup shows the position of the phantom (with embedded micromotors inside), the excitation source and the ultrasound detectors (**Figure 5.4**). The laser beam and detector transducer array were in a fixed position during the entire data acquisition. PA signal intensities in the images correlate directly to the absorption properties of the micromotors at the illuminated wavelengths. Images shown in this study were reconstructed using filtered back-projection algorithms.¹¹⁷

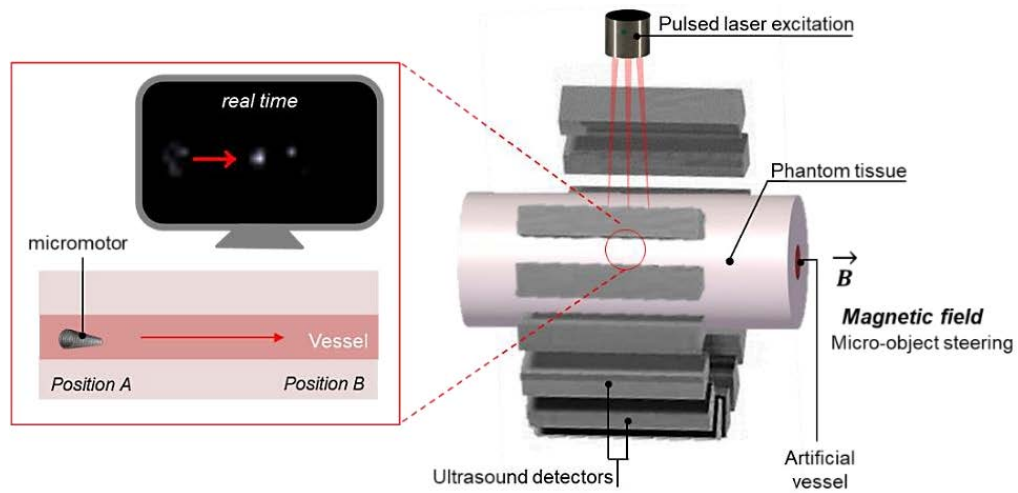


Figure 5.4. PA imaging system, illustrating the position of the phantom (with embedded micromotors inside), the excitation source and the ultrasound detectors.¹⁶⁶

Dynamic experiments were conducted with a different detector (handheld 3D cup) which was coupled to the above-mentioned PA system. The PA imaging parameters implemented in this study including frequency and wavelength ranges, acquisition time, and recording speed are given in **Table 2**.

Table 2: PA imaging parameters for visualization of micromotors

PA imaging parameters (static)			
Wavelength (nm)	680-980 nm	Detector (static)	256 elements
Frequency (MHz)	5 MHz	High energy	100 mJ
Penetration depth	1 cm	Spatial resolution	150 μm
Acquisition time	< 100 ms (single wavelength), < 1s (multispectral)		
PA tracking parameters (dynamic)			
Wavelength (nm)	820 nm	Detector (dynamic)	256 elements
Frequency (MHz)	8 MHz	Spatial resolution	80 μm
Penetration depth	1 cm	Frame rate (live)	10 fps

In PAI, a nanosecond pulsed laser is commonly used to illuminate the sample. The molecules (from target sample) absorb the optical energy and convert it into heat, giving rise to an increase in temperature. The confined optical absorption induces a temperature rise and consequently pressure rise due to thermoelastic expansion. Approximately, a temperature rise of 1 mK induces a pressure increase of 800 Pa,¹⁹⁹ which is above the noise level of typical US detector. After propagating through the scattering tissue, the pressure waves are detected by the ultrasonic transducers to form a high resolution image of optical absorption. As sound wave scatters 1000 times

lesser than light,^{199,200} the US signal penetrates much deeper in biological tissue without significant attenuation.

In a similar fashion, micromotors coated with AuNRs were embedded within the scattering phantoms (made of agarose, see Chapter 0). The phantom was illuminated by short pulses of NIR light which was absorbed by the molecules inside the phantom and the embedded micromotors. The magnitude of absorbed light was proportional to the optical absorption properties of the imaging target and local light intensity.¹¹⁴ The pressure signals, resulting from thermoelastic expansion, were simultaneously collected by 256 detector elements positioned in a tomographic way and further processed to obtain cross-sectional images of the phantom in which the micromotors were located (**Figure 5.5**).

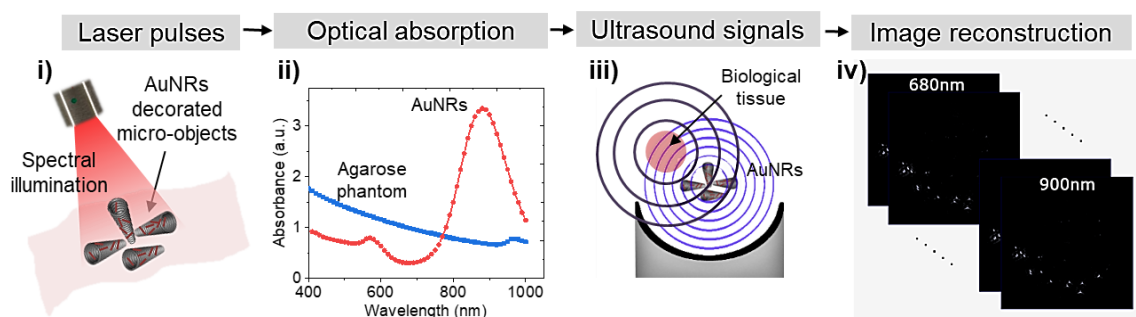


Figure 5.5. Principle of PAI. The micromotors within the phantom is illuminated by light pulses, which then results in local heat (absorption of light) that induces pressure waves due to contraction and expansion of the molecules. These sound waves are captured by ultrasound detectors and displayed on screen after on-board post-processing.¹⁶⁶

5.4 Actuation Performance below Phantom Tissue

Two different kinds of phantoms were fabricated, polydimethylsiloxane (PDMS)-glycerol and agarose containing soya milk, to systematically. We first studied the feasibility of visualizing different size of micromotors ($25\ \mu\text{m}$ in length) with and without AuNRs (**Figure 5.6a**). For this experiment we used PDMS-glycerol phantoms. The results showed a good correlation between the PA spot size and intensity increase with the increased concentration of labelled AuNRs immobilized on the micromotors' surface (**Figure 5.6b**). Though, it was not possible to distinguish adjacent smaller micromotors ($25\ \mu\text{m}$) due to limitations in spatial resolution of the used detector (with 5 MHz center frequency), which was about $150\ \mu\text{m}$.

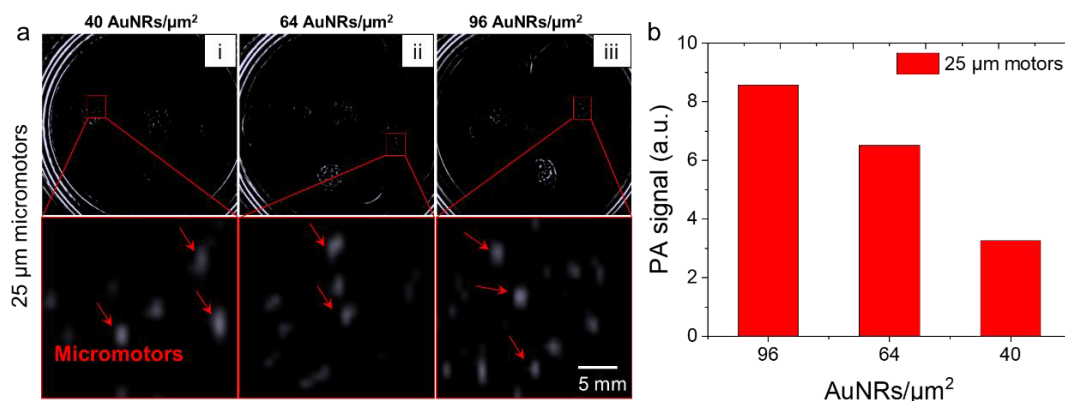


Figure 5.6. PA imaging of swarm of 25 μm long micromotors (a) and their corresponding PA signal intensity (b) for different densities of AuNRs (0, 40, 64 and 96 AuNRs/ μm^2).²⁰¹

As the speed of sound in agarose is matched to that of the surrounding water bath, single micromotors were visualized with high precision compared to those embedded in PDMS-glycerol phantoms which have a mismatch of 150 m/s compared to water, so we continue using agarose phantoms, focusing on the 100 μm length micromotors for the consequent systematic experiments. A first layer of liquid agarose was poured into the syringe and solidified for 30 minutes inside a fridge. Then a drop of 10 μL of water containing the micromotors was placed on top for drying. Finally, a second layer of agarose was poured onto the micromotors to complete the embedding procedure (**Figure 5.7a**). The sample was illuminated using multiwavelength excitation (680-980 nm) with a step size of 5 nm and the ratio between the PA signal from the functionalized micromotors (with different AuNRs concentrations) and the nonfunctionalized micromotors was obtained. Such signal is the result of the average of at least three individual micromotors. The ratio correlated well to the different AuNRs densities, and a well-defined absorbance peak at around 820 nm was detectable in all cases despite the low amount of AuNRs per micromotor (**Figure 5.7b**).

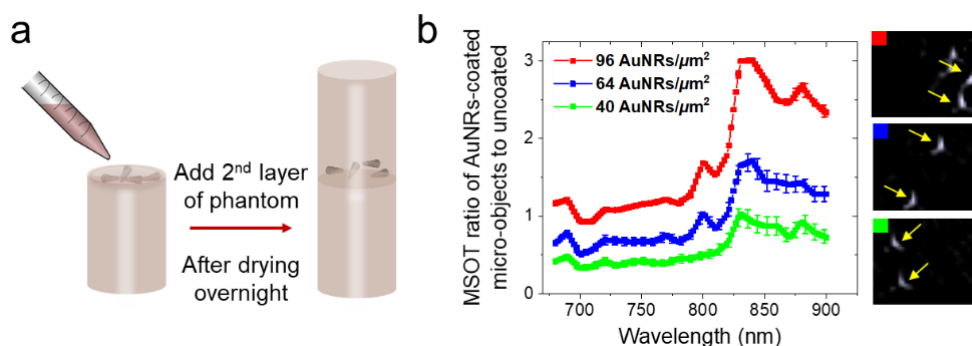


Figure 5.7. a) Schematic representation of phantom preparation. Micromotors were embedded within the phantom for static imaging studies. b) PA signals from micromotors (100 μm in length) embedded within agarose phantoms and with different density of AuNRs.¹⁶⁶

To accomplish single micromotor imaging, we did a comparative study of micromotors and analyzed the sample in both PA and optical imaging systems. For this purpose, prior to PA imaging, we captured optical images of the phantoms with micromotors during the fabrication process before pouring the second layer of agarose. Afterwards, it was possible to locate individual micromotor and visualize their distribution inside the phantoms. Bright-field images correlate well with the PA data and reveal matching locations of the micromotors before and after imaging analysis (red rectangle, **Figure 5.8**). We observed that the PA signal from static spots was proportional to the areal concentration of AuNRs. It is worth noting that the non-functionalized micromotors also absorb light but their resulting PA signal do not exhibit strong absorption as can be observed for the AuNRs-coated micromotors. The reason is that the micromotors are first coated with some metal layers for their further magnetic manipulation, and such layers also possess SPR but with a broader absorbance spectrum. The main advantage of using PA is to excite with multi-wavelength infrared light, which leads to different absorption spectra by the involved tissues/micromotors. If the micromotors are coated with specific absorbers, for example AuNRs, they will exhibit a strong signal that differs from the chromophores present in living tissues, which have a relatively broad absorption peak with low absorbance.

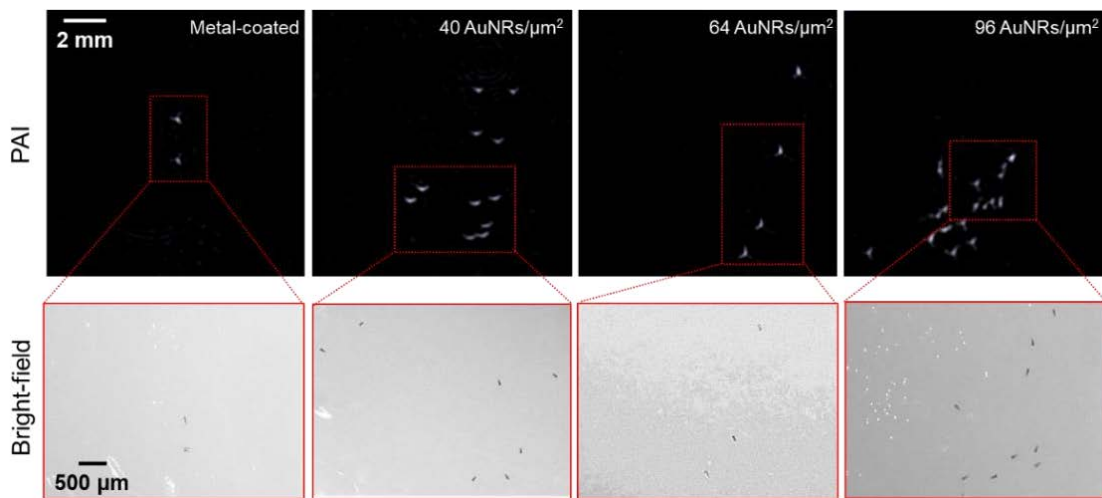


Figure 5.8. PA signal of fully embedded micromotors (top) with different densities of AuNRs (0, 40, 64 and 96 AuNRs/ μm^2), and their corresponding bright-field images (bottom) prior to the embedding procedure.¹⁶⁶

To evaluate the accuracy of the single micromotor position, we measured the distance between micromotors in both PA and bright-field images. We chose different regions of interest (ROI) where two adjacent micromotors were located and measured the distance between them using imageJ. First, we determined the maximum pixel intensity, which corresponds to the highest part of the micromotor (large opening of the lying conical microstructure) and measured the distance between those points.

The same procedure was carried out with the bright field image as shown in **Figure 5.9**. The distance in PA (ROI1) and bright-field (ROI2) images was measured to be $770 \mu\text{m}$ and $830 \mu\text{m}$, respectively, with a distance difference of $60 \mu\text{m}$. The average distance difference between the micromotors in PA and BF was about $108 \mu\text{m}$, after analyzing 4 different cases. This position shift could arise due to slight displacements of micromotors after pouring the second layer of agarose phantom.

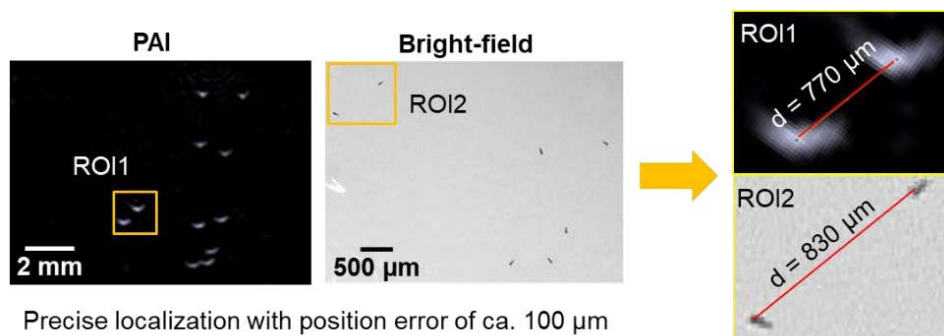


Figure 5.9. Comparison of the measured distance between two micromotors derived from PA ($770 \mu\text{m}$) and bright field ($830 \mu\text{m}$) images, resulting in a distance difference of $60 \mu\text{m}$.¹⁶⁶

The average length of a single micromotor derived from the PA signal was $525 \pm 50 \mu\text{m}$, ~ 5 times larger than the real length of the micromotor (obtained by optical microscopy) due to resolution limits imposed by the used detector array. The intensity of the PA signal increases by increasing the density of AuNRs compared to the uncoated micromotors.

In the second set of experiments, a semi-cylindrical agarose phantom with an internal channel cavity of 3 mm in diameter was prepared and placed onto a hand-held imaging detector. These dynamic experiments were conducted with a different detector (handheld 3D cup) which was coupled to the above-mentioned PA inVision system (**Figure 5.10a, Table 2**). This detector allowed real-time acquisition in 3D. The detector consisted of 256 ultrasonic elements with a central frequency of 8 MHz, which were evenly distributed over a cylindrical surface with a radius of 4 cm. The optical excitation (820 nm short-pulsed laser) for the hand-held probe was applied through a silica fiber bundle inserted into a cylindrical cavity and pointing towards the center of the phantom tissue. Acoustic gel was applied between the membrane and the imaged phantom for ensuring a proper acoustic coupling. For real-time tracking of micromotors, tunnel-shaped agarose phantoms were fabricated with an internal diameter of 3 mm. The channels were treated with 1% w/v, aqueous sodium dodecyl sulfate (SDS) solution and then micromotors were introduced. The micromotors were actuated with an external magnetic field. The tunnel shaped channel was placed on top of the 3D cap detector and the videos were captured at 10 fps.

The channel was treated with surfactant (1% w/v, SDS) to reduce the attachment of the micromotors to the inner wall surface. Afterwards, AuNRs-coated micromotors were injected into the channel which was later sealed to avoid undesired flows during the micromotors' actuation. The micromotors were moved forward by an external magnetic field (~60 mT). The magnetic field gradient was measured using the positioning of a magnet with respect to a Hall sensor over a distance of 0 to 3 cm. As the measurement was performed with a hand-held detector image blurring was avoided by using single pulse acquisition at a single wavelength (820 nm) with a temporal resolution of 10 frames per second (fps). Ultrasound signals were collected by 256 detector elements with an angular coverage of 270°. The data was processed by a workstation deconvoluting the signal from the electrical impulse response of the detectors. Band-pass filtering with cut-off frequencies between 1.8 and 7 MHz (maximum frequency available for the hand-held detector) was applied in order to exclude the low frequency signal distribution from the phantom. The information from PA images was extracted by employing image reconstruction algorithms based on the back-projection approach as previously described in the literature.²⁰²

The single moving micromotor (100 μm long) was recorded in real-time and the trajectory of a single micromotor is depicted in the time-lapse images which took 2.7 s to travel 3.1 mm (**Figure 5.10b**). The yellow arrows represent static micromotors or microstructures attached to the phantom which act as a reference point. The speed of the AuNR-coated micromotors based on the measured trajectories from the PA video was 1160 $\mu\text{m}/\text{s}$. To validate these experiments, bright-field videos were captured in a similar fashion by preparing the same kind of phantom channel, except that the channel was left open on the top side for optical tracking (**Figure 5.10c**). The red arrows show the position of moving micromotor after certain time-interval. The measured speed of the single micromotors over 2.7 s and a travel distance of 2.9 mm was 1070 $\mu\text{m}/\text{s}$, agreeing with the results obtained from the PA tracking experiment. The dynamic PA tracking performance of a single micromotor was compared with bright-field modes. Furthermore, the hand-held detector also allowed the real-time tracking in 3D at a rate of 10 fps, which is prerequisite for living body experiments. The average length of a moving micromotor at different locations along the trajectory was $\sim 585 \pm 40 \mu\text{m}$. To validate this, the average length of static micromotors (imaged with different end detector) was $\sim 525 \pm 50 \mu\text{m}$, confirming similar sensitivity and spatial resolution for both detector arrays.

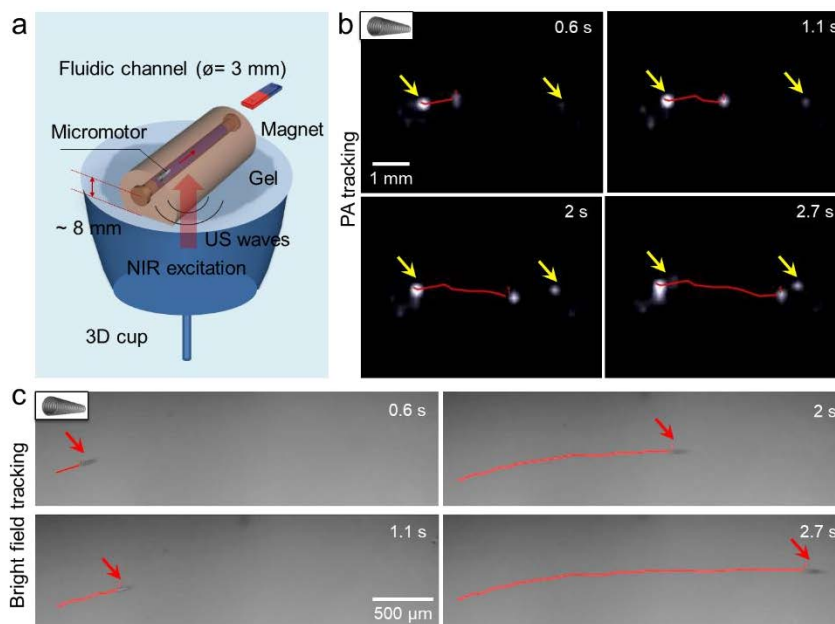


Figure 5.10. a) Schematic of 3D hand-held detector for real time tracking of moving micromotors approx. 1 cm deep. The micromotor is dragged using a permanent magnet (Magnetic Field: ca. 60 mT). b) Time-lapse images of a 100 μm micromotor moving over a time period of 2.7 s (travel distance = 3.1 mm). Yellow arrows point at static micro-structures which were stuck on the phantom surface and which are used here as reference points. Red lines mark the trajectory of a single moving micromotor after different time intervals. c) Optical tracking of a single micromotor over the same period of time (2.7 s) in an open agarose channel to compare the velocity and traveled distance (2.9 mm) within the same time interval.¹⁶⁶

5.5 Actuation Performance below *Ex Vivo* Tissue

To demonstrate that the micromotors can be tracked and visualized below real biological tissues, we utilized *ex vivo* chicken breast tissue with a thickness of ~ 1 cm, comparable to the thickness of the phantom tissue used in the previous section. We implemented the same experimental conditions and used the same 3D hand-held detector for real-time monitoring as discussed above. We placed a semi-cylindrical phantom with an internal channel cavity on top of the chicken breast tissue and positioned it onto a handheld detector (**Figure 5.11a**). The thickness of the chicken tissue was measured with a Vernier caliper. Again, acoustic gel was applied between the detector surface and the phantom for efficient signal transfer coupling. A solution of ~ 10 μl micromotors coated with AuNRs (density of 96 AuNRs/ μm^2) was injected into the channel and the micromotors were dragged forward by an external magnetic field (~ 60 mT). The locomotion of a single micromotor was tracked under ~ 1 cm chicken breast over a period of 1.3 s (**Figure 5.11b**).

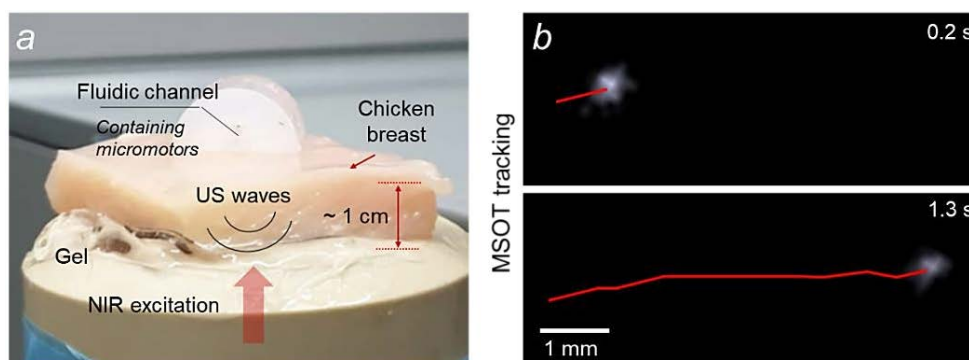


Figure 5.11. a) Tracking of micromotors labelled with AuNRs underneath ~ 1 cm chicken breast tissue. b) Time-lapse images of a moving micromotor over a time period of 1.3 s.¹⁶⁶

In summary, we demonstrated that PAI can be used to track single moving micromotors ($100 \mu\text{m}$ in length) in real time below tissue-mimicking phantoms and *ex vivo* chicken breast tissues with a penetration depth of ~ 1 cm. Such micromotors can be later used as drug carriers or as components of medical microrobots to perform a medical task in living organisms. We established the localization of individual micromotors with a precision of ca. $100 \mu\text{m}$, within phantom tissues which mimic the absorption/scattering properties of real biological tissues, as previously reported in the literature.²⁰³ This work represents an important step towards the use of physically-driven micromotors for non-invasive diagnosis and therapy under scattering tissues. PA emerges as a promising new tool for localization and tracking of single moving micromotors in hard-to-reach target sites, which could significantly improve the accuracy and effectiveness of current diagnosis and therapeutics in the future.

Disclaimer:

The results presented in this chapter have been published in Nano Letters with the following permissions.

“Reprinted with permission from [A. Aziz, M. Medina-Sánchez, J. Claussen, and O. G. Schmidt, “Real-Time Optoacoustic Tracking of Single Moving Micro-objects in Deep Phantom and *Ex vivo* Tissues” Nano Lett., 19 (9), 6612–6620, 2019]. Copyright [2019] American Chemical Society.”

6 HYBRID ULTRASOUND AND PHOTOACOUSTIC IMAGING

Until now the micromotors have been imaged/tracked in phantom or *ex vivo* tissues and it is interesting to visualize the micromotors in more realistic environment inside living body. There are significant limitations when steering single or swarms of MNRs in living organisms,³ in particular when the intended application and micromotor type require high spatiotemporal resolution with precise anatomical positioning. In previous chapter, we use PAI, for the first time, to visualize single moving magnetically-driven conical micromotors (up to 100 μm long) in 3D, underneath ca. 1 cm phantom and in *ex vivo* chicken tissue samples.^{166,201,204}

In later studies, PAI was also employed for guiding capsules containing catalytic micromotors in mice intestines, as well as to track swarms of magnetic spiral-like micromotors to treat induced subcutaneous bacterial infection, also in mice.^{5,205} Both studies showed the application of micromotors *in vivo* but there was no clear observation of single or very few micromotors imaging in real-time in living mice, or the distinction between the structure and function of a single or few micromotors and their surrounding environment. Thus, the complementary particulars such as morphology, functionality, and molecular composition are required to enhance the position accuracy of employed MNRs deep in tissue. Technological analogies between PA and US imaging systems allow easy implementation of dual modality scanners, to expand their potential in morphological functional and molecular imaging²⁰⁶ and this hybrid imaging modality provides another interesting concept, where US allows for accurate real-time tracking of MNRs in deep tissues and PA is responsible for unique signature discrimination from the surrounding tissues.

In this chapter, we investigate the use of hybrid high-frequency US and PA (HFUS and PA) imaging to monitor swimming micromotors' motion and function. In particular, we monitor a single or swarm of magnetically-driven spherical micromotors in different scenarios: phantoms, *ex vivo*, and *in vivo* (in mouse bladder and uterus). Real-time monitoring of bladder catheterization and the localization of the uterus to monitor micromotors during administration is also demonstrated.

6.1 Hybrid Ultrasound/Photoacoustic System

PA measurements were carried out by using the Vevo-LAZR X (FUJIFILM VisualSonics, The Netherlands) system, a multimodal platform which allows the simultaneous imaging of high-resolution ultrasound and photoacoustics. The system was equipped with a linear array ultrasound transducer at a central frequency of 21 MHz and fiber optic bundles on either side of the transducer for illumination. The fiber bundle was coupled to a tunable Nd: YAG laser (680 to 970 nm) with a 20 Hz repetition rate and the signals were collected by the 256-element linear array transducer (**Figure 6.1**).

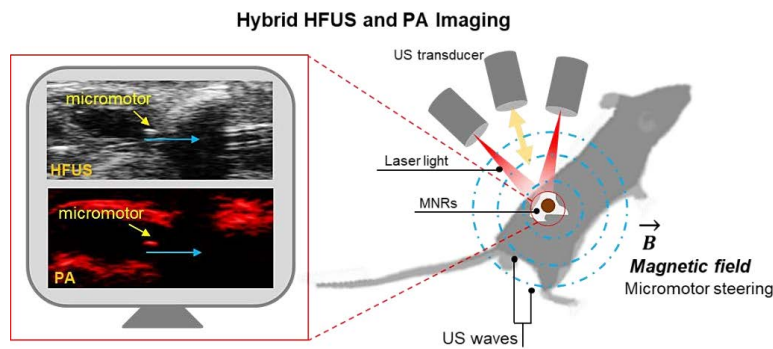


Figure 6.1. Schematic showing the working principle of the employed hybrid HFUS and PA imaging technique.²⁰⁷

The pulsed laser generated a wavelength-tunable pulsed beam (680-970 nm) which was delivered by a bifurcated fiber bundle integrated with US transducer. Both HFUS and PA signals were collected and reconstructed using on-board software.

Table 3. Imaging parameters for Hybrid HFUS and PA system

Hybrid HFUS and PA system			
Static imaging		Dynamic imaging	
Wavelength (nm)	680-970 nm	Wavelength (nm)	800 nm
Frequency (MHz)	21 MHz	Frequency (MHz)	21 MHz
Detector elements	256	Detector elements	256
Axial resolution	75 μ m	Axial resolution	75 μ m
NA		Temporal resolution	US (max.320 fps) / PA (5-20 fps)
Penetration depth	~1 cm (ex vivo) ~2 cm (<i>in vivo</i>)	Penetration depth	~2 cm (bladder and uterus)

For single pulse excitation, the PA images were acquired at an excitation wavelength of 800 nm with in-plane axial (75 μm) and temporal (5-20 fps) resolution. The same protocol was applicable for *in vivo* imaging in mice bladder and uterus. **Table 3** shows implemented imaging parameters for this hybrid study.

6.2 Fabrication and Characterization of Micromotors

The micromotors (SiO_2 particles with a diameter of 100 μm) were fabricated using a drop-casting method followed by the evaporation of subsequent thin metal layers (Ti=10 nm, Fe=50 nm, and Ti=10 nm) (refer to Chapter 3). The particles were half-coated with metal layers by electron-beam deposition as shown in optical and SEM images (**Figure 6.2a**). The same particles were also functionalized using a fluorescent anticancer drug as a model drug, doxorubicin (DOX), for further drug-release monitoring via PAI illustrating further *in vivo* targeted therapeutic ability (**Figure 6.1b**). All kinds of absorbing micromotors (tubes, helices, or spheres) are suitable for PAI. In the previous section, we studied the PAI of microtubes, and here we adopted different geometry to make sure that varying micromotor shapes can also be visualized.

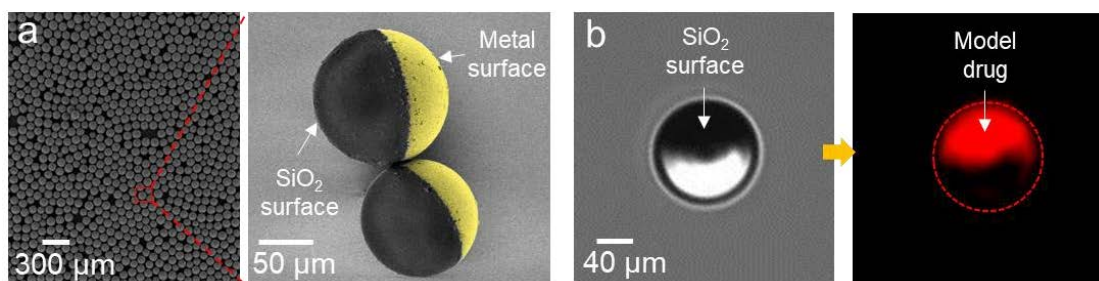


Figure 6.2. a) Optical and SEM images of spherical micromotors half-coated with metal layers (10 nm Ti, 50 nm Fe and 10 nm Ti). b) Bright field and fluorescence images of the functionalized micromotors with a model drug (DOX).²⁰⁷

6.3 Actuation and Propulsion Performance below Phantom

The following experiments were performed in collaboration with FUJIFILM VisualSonics, The Netherlands and conducted in both tubing phantom and *ex vivo* tissues. For the tubing phantom setup, a commercially available methacrylate support (Vevo Phantom, FUJIFILM VisualSonics, The Netherlands) was used to mount transparent intravascular polyurethane (IPU) tubing (inner diameter ~ 380 μm and

outer diameter $\sim 840 \mu\text{m}$, SAI Infusion Technologies, USA) as a fluidic channel for flow experiments. The micromotors were inserted in the tube, and it was then immersed in the phantom chamber containing DI water for better acoustic coupling (**Figure 6.3a**). After the PA image acquisition, the spectral characteristics of the samples were recorded. 3D single-wavelength (800 nm) imaging was also performed using a 2D stepper-motor and a linear translation of the transducer over the IPU tubing. For control experiments, another tube was mounted with a saline solution.

US image quality is influenced by the medium through which sound travels from the transducer. Material choice is a crucial factor in US imaging to match the speed of sound and to avoid undesired artifacts. Thus, the materials must possess low attenuation, meaning that acoustic waves are able to reach the target (micromotor) and return. The material should also exhibit low backscatter between the micromotor and the transducer. The ratio of the micromotor reflection intensity to backscatter intensity is chosen as a relative figure-of-merit to determine the material performance.²⁰⁸ The IPU tubing features low attenuation and low front surface backscatter that provides a better HFUS contrast making possible to visualize single moving micromotors inside this tube phantom. The dynamic tracking of a single micromotor is shown in time-lapse images from 0 to 3.40 s (**Figure 6.3b**), comparing BF, HFUS, and PA imaging modes. Blue arrows show the position of static micromotors (stuck on the tube walls) while the yellow arrows correspond to the single moving micromotor. This hybrid feature is useful in deep tissue imaging where US provides tissue background morphology and PA maintains high contrast of the micromotors.

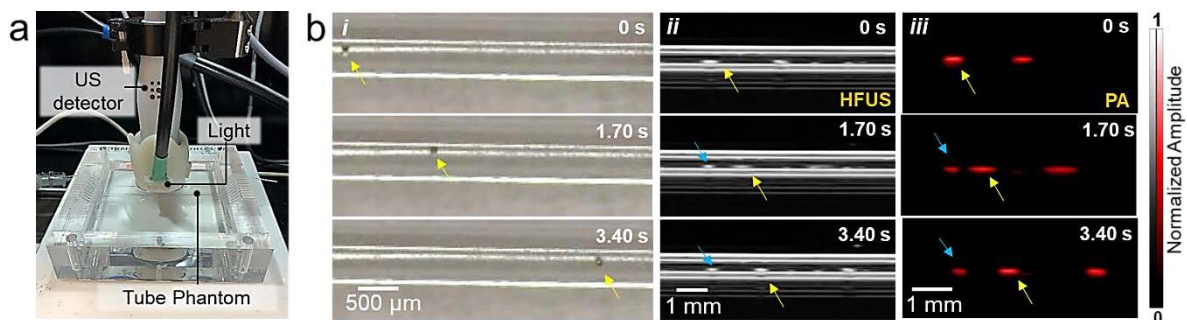


Figure 6.3. Tracking of single micromotors in phantom and *ex vivo* chicken tissues; a) Phantom chamber with tubing immersed in a water batch with HFUS-PA detector on top of it for real-time tracking of moving micromotors. b) Time-lapse images of a $100 \mu\text{m}$ moving micromotor in BF (i), HFUS (ii) and PA (iii) modes. Yellow arrows show the single moving micromotors. Scale bars: 1 mm.²⁰⁷

6.4 Actuation and Propulsion Performance below *Ex Vivo* Tissues

Chicken breast samples were prepared and used with thicknesses of 5 and 10 mm (refer to Chapter 0). The IPU tubing was filled with the micromotors suspended in PBS 1X and then placed between two 5 mm tissue samples (**Figure 6.4a**). The process was repeated for 10 mm thick tissues afterwards. To ensure uniform distribution of thickness and prevent from drying, the thickness of the tissue samples was measured using a digital Vernier Caliper. The tissues containing micromotors were then placed on an imaging chamber grid for tracking measurements.

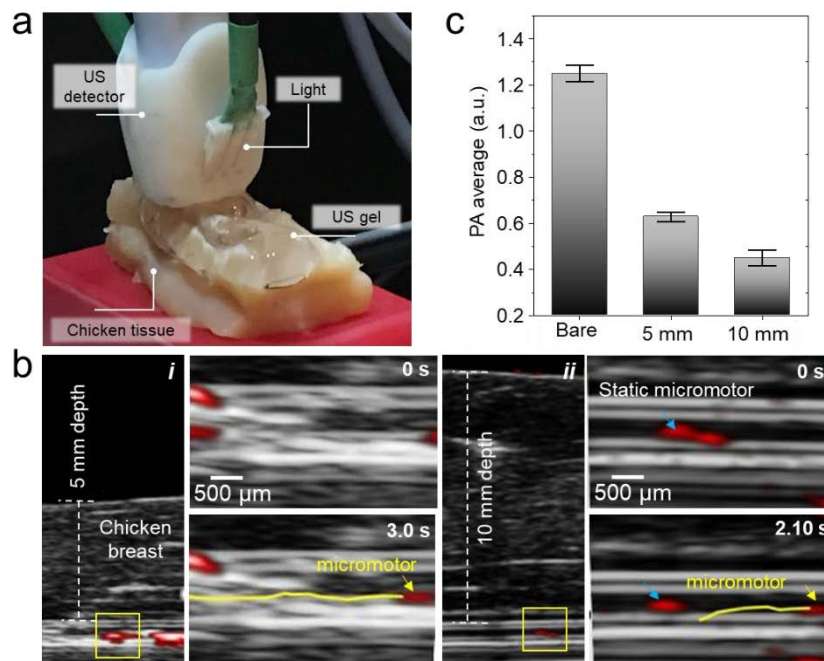


Figure 6.4. a) Micromotors inserted in IPU tubing which is then sandwiched between two chicken breast tissues. The US gel was applied between the acoustic transducer and the chicken surface for efficient acoustic coupling. b) Micromotors embedded within chicken breast tissue and the time-lapse images of a moving micromotor below 5 mm (i) and 10 mm (ii) thick tissue. c) PA signal of single micromotors with comparable ROIs below 5- and 10-mm thick tissue, which decreases with increased penetration depth. Blue arrows show the static structures.²⁰⁷

To visualize the micromotors underneath biological tissues, we employed chicken breast from a local store, with an approx. 5- and 10-mm thickness (measured with a Vernier caliper). The IPU phantom tubing containing micromotors was placed in between two layers of chicken breast tissue for the consequent measurements. The US gel was applied between the detector surface and the top of the tissue to match the acoustic impedance for efficient signal transfer. HFUS brightness-mode (B-mode) generated a structural image, suitable to identify the tubing structure, and the PA

system was used to monitor the displacement of the micromotors, by detecting their light absorption characteristics. Both images were acquired in real-time during external magnetic steering. The locomotion of a single micromotor was tracked under 5- and 10 mm thick tissue samples and it was possible to display overlaid HFUS and PA images as shown in time-lapse images (**Figure 6.4b**). The corresponding PA amplitude values of the micromotors are shown in **Figure 6.4c**. The micromotors showed decreased PA intensity when increasing the tissue thickness due to pronounced scattering of the excitation light in deep tissues.

6.5 Actuation and Propulsion Performance in Mice

6.5.1 Swimming of Micromotors in Bladder

The following *in vivo* HFUS and PA experiments were performed under the animal handling license No. DVS06. The *in vivo* study of the micromotors was conducted using the same equipment and the imaging settings as those for in phantoms or *ex vivo* studies (**Table 3**). The animal testing was performed to illustrate the potential of hybrid HFUS and PA imaging system regarding penetration depth and real-time navigation ability of a single or swarm of micromotors. The micromotors were injected into the bladder and uterus of 12-week old mice. We selected the bladder and uterus cavity as sites of injection to allow enough room for the micromotors free swimming. The bladder is a hollow soft organ that serves as a reservoir for the storage and periodic release of urine, with areal dimensions of approx. 5.50×6.0 mm as shown in 2D US image with anatomical features of bladder and physiological parameters. Under anesthesia, the mouse bladder was catheterized by following standard safety guidelines and protocols.²⁰⁹ Before starting the experiments, the physiological parameters of the mouse were also monitored.

First, the micromotors were collected (15-25 in ~20 μ l PBS) in a catheter, and then inserted into the bladder. The catheter was inserted through the urethra of an anesthetized mouse as shown in schematic in **Figure 6.5a**. The position of the catheter and bladder was monitored *in vivo* as shown in the 3D B-mode reconstructed image (**Figure 6.5b**). After reaching the entrance of the bladder, the micromotors were released gradually into the bladder cavity. The overlaid HFUS and PA image shows the micromotors near the catheter edge before and after release. PA signal (red spot) highlights the swarm of micromotors being ejected from the catheter. While US image highlights the anatomy of the organ of operation, the PA image shows the molecular information (meaning the material absorption properties) of the imaged micromotors.

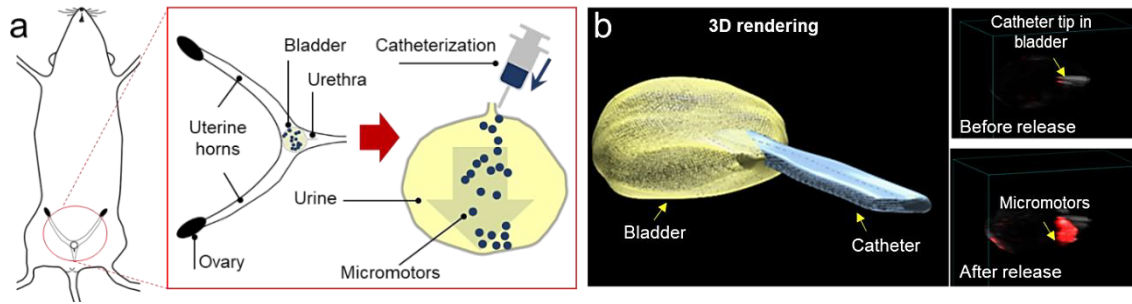


Figure 6.5. *In vivo* HFUS and PA imaging of micromotor: a) Schematic showing the position of the bladder. b) 3D reconstruction of the bladder with the inserted catheter, after performing the catheterization via real-time US feedback and HFUS and PA overlaid images showing the location of the catheter tip, before and after releasing the micromotors.²⁰⁷

After release, the micromotors started to swim down freely in the urinal fluid, and it was possible to visualize the micromotors from a single to very few and even a swarm of them while sinking to the bottom of the bladder cavity. Time-lapse HFUS and PA images show the swimming behavior of micromotors in urinal fluid from top to bottom surface of the bladder over a period of 2.50 s (**Figure 6.6**) and the swimming speed or falling velocity of a cluster of micromotors in the bladder was estimated to be ca. 1250 $\mu\text{m/s}$ (in the current experiment).

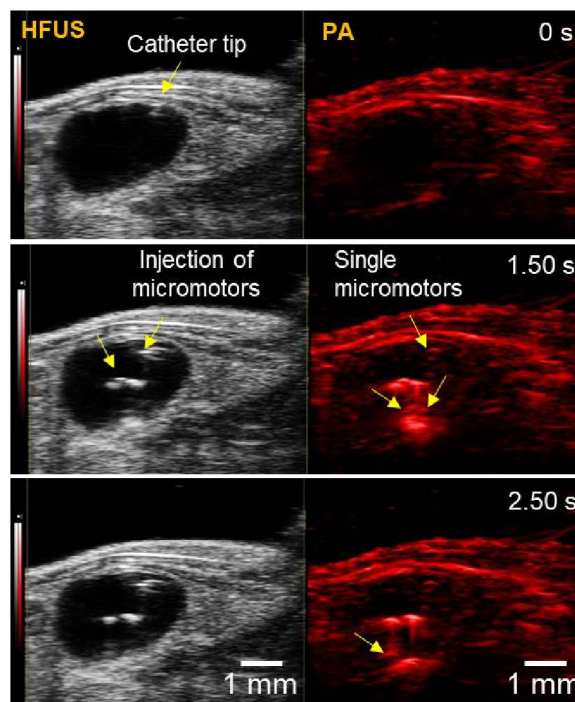


Figure 6.6: Hybrid HFUS and PA time-lapse images of swimming and free-falling micromotors over a time period of 2.50 s. The micromotors migrate downward after being released from the catheter tip individually and then accumulate at the bottom surface.²⁰⁷

The downward displacement of one of a small cluster was ca. 1.6 mm which took 1.3 s to reach the bottom of the bladder. Finally, the whole swarm of micromotors at the

bottom of the bladder was manipulated by using the external magnet and the swimming micromotors were visualized within the bladder environment. The upward displacement of the whole swarm centroid was estimated to be ~ 3.5 mm (in the current experiment) after a time interval of ca. 8 s and the dimension of the moving cluster was estimated to be between 2 to 3 mm wide (**Figure 6.7**). The speed of single or swarm of micromotors also depends on the strength of the applied field at the evaluated distance from the micromotor position. In this experiment, the magnet was placed directly onto mouse skin, after removing the rodent fur with a depilation cream, being approx. 2 cm away from the micromotors location (inside the mouse bladder), resulting in an estimated magnetic field of ~ 60 mT. It is worth noting that this is a proof-of-technology study that shows the ability of controlled movement of micromotors in real-time in mice by employing HFUS and PA imaging. However, a more sophisticated setup including dedicated magnetic field actuators are necessary for a precise steering and complex actuation of the here-presented micromotors and can be extended for any other medical micromotor.

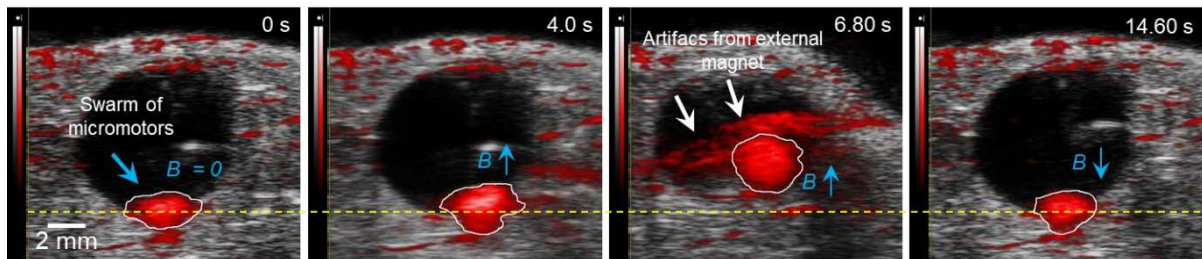


Figure 6.7. A swarm of swimming micromotors under the actuation of an external magnetic field gradient (estimated magnetic field strength (~ 60 mT)). The upward displacement of the swarm centroid from the dashed yellow reference line, was estimated to be ~ 3.5 mm after a time interval of approx. 8 s. The dimension of this moving cluster was ca. 2 to 3 mm wide. White arrows show the artifacts arising from the close proximity of the external magnet.²⁰⁷

6.5.2 Actuation of Micromotors in Uterus

Apart from bladder, we also evaluated the micromotors imaging in the mouse uterus. Here, the catheter was inserted via the vagina and cervix into the uterus cavity by following the previous safety guidelines.²⁰⁹ In this experiment, we investigated the smallest detectable feature size of micromotors in uterus by injecting controlled number of micromotors as depicted in the schematic in Figure 4a. The samples were dispersed in PBS containing few micromotors (<10) in a catheter. By employing US

imaging, it was possible to precisely locate the catheter tip at the opening of the uterus cavity prior micromotors insertion (**Figure 6.8, a-b**).

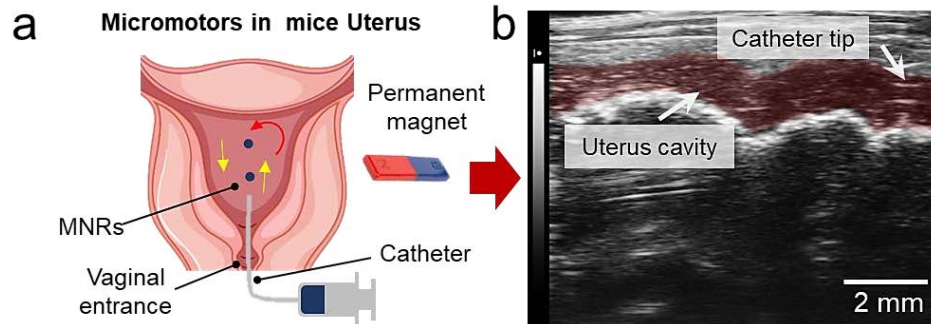


Figure 6.8. HFUS and PA imaging of micromotors moving in the uterus; a) Schematic showing the insertion of the catheter into uterus body through the vagina and moving micromotors by applying an external magnetic field. b) Real-time HFUS feedback positioning of the catheter in the mouse's uterus. Red-shaded area indicates the uterus channel.²⁰⁷

Ultimately, it was possible to deliver ca. 2-3 micromotors in the mouse uterus from the catheter needle. One of the micromotors was steered in real-time in the uterus channel over a trajectory of $\sim 950 \mu\text{m}$. Time-lapse HFUS and PA images showed the moving micromotors from one position to another over a period of 3.60 s (**Figure 6.9a**). The resulted images comprise PA amplitude values of the uterus cavity with and without micromotors (control) by choosing comparable ROIs (**Figure 6.9b**).

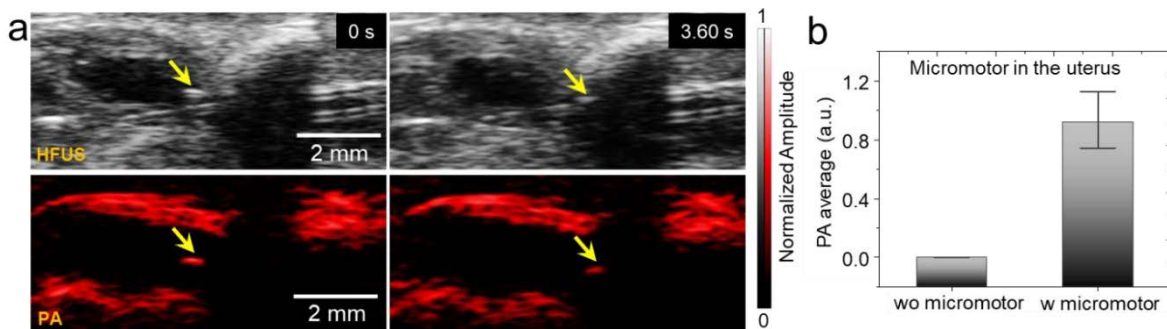


Figure 6.9. a) Time-lapse images of single moving micromotors (Yellow arrows show the position of moving micromotor). b) PA amplitude values extracted from the captured PA images of a single moving micromotor, compared to the control (uterus location where no micromotors was visible “wo micromotor”).²⁰⁷

HFUS images have speckle patterns from the background tissues which make it challenging to identify the micromotors. The tracked micromotor was visible in both HFUS and PA modes, however it is clear that HFUS provided a better visualization of the catheter entrance and the surrounding uterus anatomic features, while PA facilitated the discrimination of the light absorbing micromotors from the surrounding environment, offering a high SNR ratio. The employed micromotors and the here-evaluated hybrid imaging system is appealing for the supervised drug cargo-delivery

towards urinary tract diseases e.g. urethral stenosis, bladder cancer, or infection, or towards *in vivo* assisted fertilization, where similar engineered parts can be used to guide or transport sperm.^{16,32}

6.5.3 3D Multispectral Imaging

The advantage of multiplexed imaging or spectral unmixing is in being able to distinguish light absorbing signals coming from the different organic and inorganic components present in the field of view.¹¹⁰ The multi-wavelength mode takes advantage of the tunability of the pulsed laser source to acquire PA data at multiple wavelengths in 2D and 3D for automated post-processing, obtaining a unique spectrum. Such specific spectral capacity of PAI offers specific detection of endogenous molecules like oxygenated (oxy-Hb) and deoxygenated hemoglobin (deoxy-Hb), among others.⁹⁹ The first step is to image the target (micromotors, oxy- and deoxy-Hb or other employed materials) at multiple wavelengths. Then spectral unmixing algorithm is applied, generating separate images based on the contrast obtained from the different absorber materials (endogenous or exogeneous). Thus, when merging the independent images, one can obtain the distribution of oxy- or deoxy-hemoglobin as well as of the present micromotors marked according their absorption properties.

In this experiment, the mouse was injected with a 10 μ L mixture of PBS and target micromotors into the hind limb (popliteal lymph node fat pad), followed by the PA multi-wavelength measurement in the wavelength range of 680 to 970 nm with a step size of 5 nm in the spectral mode, at a frequency of 30 MHz. The obtained signals were then spectrally un-mixed to discriminate the PA signal of injected micromotors from the surrounding tissue chromophores (**Figure 6.10a**). 3D reconstruction of the target site demonstrates the spectral behavior of the injected micromotors (yellow color) and the chromophores present in blood i.e. oxy-Hb, deoxy-Hb (**Figure 6.10b**). For deep *in vivo* imaging, it is important that the introduced micromotors hold a unique absorption signature compared to the tissue background. **Figure 6.10c** shows the PA amplitude of the micromotors (yellow curve), in comparison with oxy- and deoxy-Hb and it is possible to clearly distinguish the injected micromotors. The PA amplitude values of the micromotors were extracted from the captured PA images and then calibrated with measured optical absorption of hemoglobin.

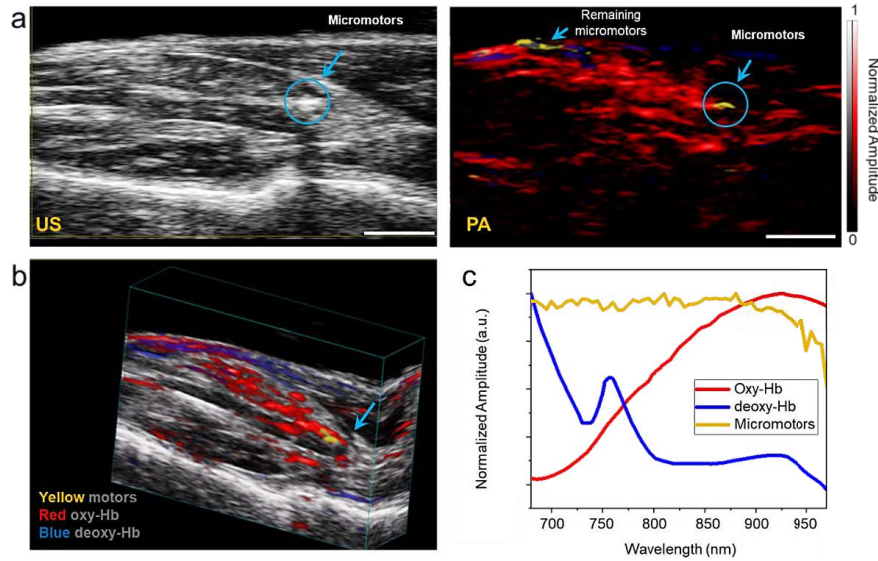


Figure 6.10. 3D multiplexing *in vivo*: a) Injection of micromotors into the mouse hind limb (popliteal lymph node fat pad) and HFUS and PA imaging of a swarm of micromotors (Yellow spot in PA mode shows the position of injected micromotors within tissue). The remaining micromotors from syringe tip were also visible on tissue top surface after taking it out. Scale bar is 2 mm. b) 3D reconstruction and spectral unmixing of the injected micromotors in tissue. c) PA signal strength of the injected micromotors (yellow), oxy (red) and deoxygenated (blue) hemoglobin.²⁰⁷

3D multiplexing PA scans have allowed investigating the biodistribution of the injected micromotors *in vivo* which in turn can be used to target specific body organs to perform a certain medical task. We used metal-coated micromotors that absorb light and generate spectral signatures for acoustic detection and the resulting PA signals exhibited a broad absorption spectrum. In the uterus and bladder cavity, due to the fluid inside, image contrast was better to distinguish the micromotors. However, when injected within the tissue, the signal from oxy- and deoxy Hb, and other chromophores hindered the signal of the micromotor. In this case, spectral unmixing was applied to distinguish the signals by their specific absorption peaks. Another strategy to enhance the PA signal of injected micromotors is to stamp them with suitable and biocompatible contrast agents that absorb in a narrow and specific wavelength range, such as AuNRs shown in Chapter 5.

6.5.4 Towards Targeted Drug Delivery

The spherical micromotors were loaded with an anticancer drug (doxorubicin, DOX), which is widely approved for cancer therapy and a model drug (indocyanine, ICG). ICG is an FDA approved contrast agent for use in humans and was employed for this experiment due to its unique absorption peak at 880 nm. The micromotors were functionalized by overnight incubation in an ICG or DOX using the same protocol. ICG

or DOX solution was prepared with a concentration of 100 $\mu\text{g}/\text{ml}$ and then mixed with the micromotor solution with PBS ($\sim 10 \mu\text{L}$). The mixture was covered with aluminum foil and incubated for 24 h.

To evaluate the loading of the DOX micromotors, fluorescence microscopy was used to track a single micromotor with an excitation wavelength of 470 nm). It was possible to distinguish drug-loaded micromotors from un-loaded (control) ones using fluorescence microscopy. DOX possesses an intrinsic fluorescence with an emission peak at around 600 nm. It shows the potential of using micromotors as a drug-carriers.

Here, we propose a potential scenario where this technique and the employed spherical micromotors could be applied. As reported previously in the literature, metal-coated particles have been shown as drug carriers, propelled either by bacteria or by chemical reactions to target cancer cells *in vitro*.^{28,165,210} The loading mechanism ranges from physical absorption to more sophisticated stimuli-responsive delivery triggers. To evaluate the feasibility of HFUS and PA to not only identify the drug-loaded micromotors but also to monitor the drug release overtime, we functionalized the micromotors with a model biomolecule (indocyanine, ICG), similar as it was done for DOX. ICG, an FDA approved contrast agent, was chosen due to its unique absorption peak at 880 nm which facilitated their visualization via PAI, with negligible artifacts arising from autofluorescence or surrounding tissues deep in the body. As a proof of concept, we first functionalized the spherical micromotors by overnight incubation in an ICG solution (see Chapter 0). The illustration of ICG or a drug immobilized onto the SiO_2 surface of the Janus micromotor, followed by the drug release mechanism over time is shown in **Figure 6.11a**. To test if the cargo was successfully loaded onto the micromotor, a solution of $\sim 20 \mu\text{l}$ of ICG-loaded micromotors was injected into IPU tubing and HFUS and PA signals were recorded in static conditions, as shown in **Figure 6.11b**. An ROI was chosen to plot the PA spectrum of ICG-loaded micromotors. ICG-loaded micromotors exhibited a distinct absorption peak at around 880 nm as expected from its optical properties (**Figure 6.11c**, red curve). After a time-lapse of ca. 2 min, the same ROI was analyzed to get the PA signal of ICG-loaded micromotors, showing a decrease in PA amplitude without any distinct peak, indicating the complete release of ICG, which rapidly diffused in the surrounding after NIR light was turn on. This test highlights the advantages of the PA system to monitor known optical signatures of implemented materials/drugs for precise cargo-delivery inspection. Different drug release mechanisms can also be explored using this technique, as in a recently reported work, where the NIR light irradiation by PAI was sufficient to disintegrate the capsules to deliver the micromotors in the stomach of a mouse,⁵ or for triggering the drug release for treating sub-skin pathogenic bacterial infections via photothermal therapy (heating of a bacterial site up to 54 $^\circ\text{C}$).²⁰⁵

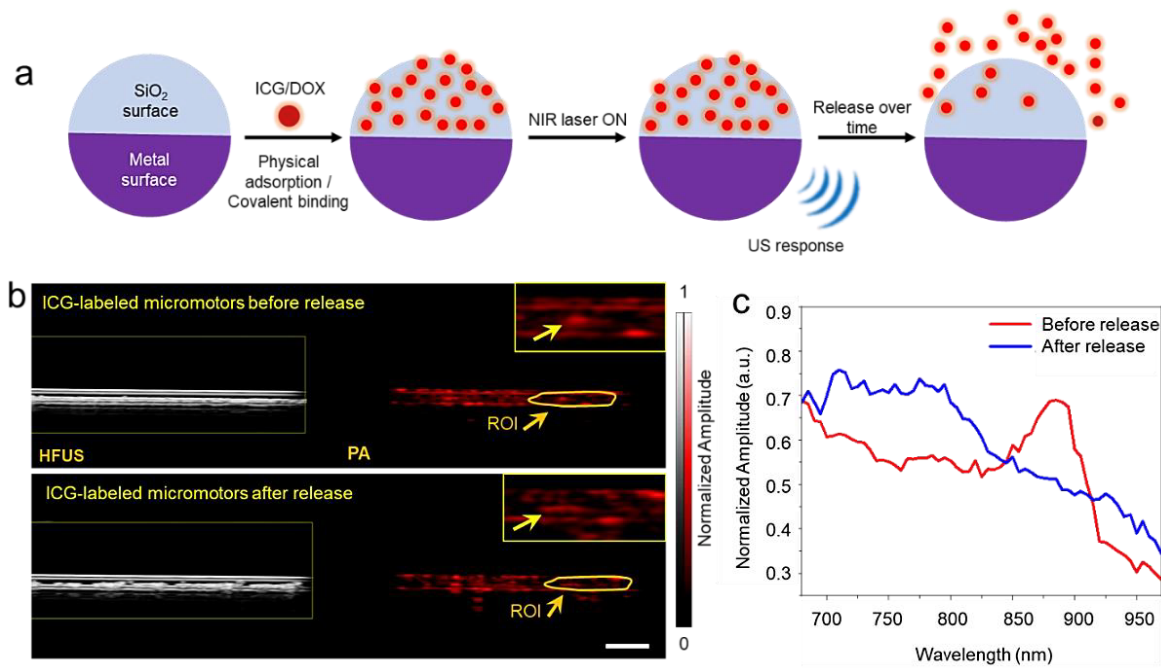


Figure 6.11. Application scenario of micromotors for drug delivery monitoring: a) Schematic showing the immobilization of a model drug on the Janus micromotor, followed by its release. b) ICG-coated micromotors injected into IPU tubing. Scale bar is 1 mm. c) PA spectral signal showing a distinct absorption peak at around 880 nm (red curve) before and after release, when analyzing a fix ROI where a few static micromotors were located.²⁰⁷

Disclaimer:

The results presented in this chapter are available online in bioRxiv pre-print version and reprinted from [A. Aziz, J. Holthof, S. Meyer, O. G. Schmidt, M. Medina-Sánchez, “In Vivo Imaging of Swimming Micromotors Using Hybrid High-Frequency Ultrasound and Photoacoustic Imaging” bioRxiv, 2020. doi: 10.1101/2020.06.15.148791].

7 SUMMARY AND PERSPECTIVES

7.1 Summary

In summary, this doctoral thesis presents reflection-based imaging, stand-alone photoacoustic and hybrid photoacoustic/ultrasound modalities for the tracking of single or swarm of moving micromotors in phantoms, *ex vivo* and *in vivo* scenarios (in mice bladder and uterus). It is clear that no single imaging technique works for all and can solve current medical microrobotics challenges and that each imaging modality has its own strengths and limitations. The X-ray and magnetic imaging techniques can penetrate deep in body tissues but carry low spatial resolution and requires expensive instruments. Apart from this, X-rays can also cause damage owing to its potential ionization and can eventually cause damage to the medical personnel/patient for prolonged exposures. In contrast, MRI enables deep tissue imaging without any contrast agent along with acceptable spatial and temporal resolution but requires strong magnetic fields and expensive infrastructure. On the other hand, the optical and US methods are somehow safe and cost-effective. US alone suffers from spatial resolution but provide real-time monitoring and deep tissue penetration together with low cost and high safety. Above all, the selection of imaging technique must be carried out according to the microrobots type, specific situation of patient or disease and exact imaging requirements. **Table 4** summarizes the main results and performances obtained with conventional and hybrid imaging techniques underlying their employment in imaging/tracking a single or swarm of MNRs *in vitro*, *ex vivo* or *in vivo* conditions. As underlined in the previous sections, most of the MNRs imaging and tracking works reported till now have demonstrated the potentialities of medical imaging in MNRs tracking and localization mainly *in vitro* or in tissue-mimicking phantoms. Just a few demonstrations combining *in vivo* localization and closed-loop imaging assisted position control have been reported.^{4,5,42,46,205} This state of the art reflects that, despite the potentialities, huge engineering efforts are still needed to progress towards clinic. Interesting perspectives are envisioned by hybrid techniques and multimodal imaging, which allow to combine the strength of different techniques and overcome their limitations by exploiting multiple physical principles as presented in Chapter 5 and 6 in this thesis.

Table 4. Summary of all imaging techniques for medical tracking of MNRs

MRI								
Micromotor type/propulsion	Label	Feature size	Tracking speed	Penetration depth	Safety	Cost	Ref.	Comments
Spirulina / magnetic propulsion and guidance	Fe ₃ O ₄ NPs	10000 spirulina structures (spot size: 3-5 mm)	1 frame / 7 min	<i>In vivo</i> (Mouse intragastric injection)	High	High	Yan <i>et al.</i> 2018 ⁴	Good spatial resolution Tissue imaging High penetration depth
X-rays								
Janus particle / X-ray propulsion	/	6 μm	Real-time	In Phantom (water chamber and glycerol)	Low	High	Xu <i>et al.</i> 2019 ⁵⁴	High penetration depth High resolution Tissue imaging
Bullet-shaped microrobots / magnetic propulsion	/	2 mm (diameter) – 15 mm (length)	Real-time	In vivo (living pig)			Jeong <i>et al.</i> 2016 ²¹¹	
PET-CT								
Catalytic / chemical propulsion and magnetic guidance	Iodine isotope	Swarm (10-20 structures; element size: 10μm)	7 frames / 15 min	In Phantom (tube containing turbid solution)	Low	High	Vilela <i>et al.</i> 2018 ⁵²	High penetration depth Low temporal resolution
SPECT								
Tubular microrobots / not propelled	^{99m} Tc Zinc colloids	100-500 μm	static	Ex vivo (mice subcutaneous injection)	Low	High - Medium	Iacovacci <i>et al.</i> 2019 ⁶⁴	High resolution High penetration depth Poor temporal resolution
Optical								
Magnetic Helices / magnetic propulsion and guidance	NIR-797 dye	Swarm (80000 ABFs; element size, ~16μm)	1 frame/ 1 min	In vivo Mouse peritoneal cavity	High-Medium	Low	Servant <i>et al.</i> 2015 ⁴⁶	Fluorescence Good sensitivity Poor spatial and temporal resolution
Spirulina/ magnetic propulsion and guidance	Autofluorescent	Swarm (spot size: 3-5 mm)	1 frame/ 5 min	In vivo Mouse subcutaneously			Yan <i>et al.</i> 2018 ⁴	
Reflective particles / magnetic propulsion and guidance	Metal layer	20 μm	Real-time (30 fps)	Ex vivo 160 μm deep mouse skull			*Aziz <i>et al.</i> 2019 ¹⁶⁵	Reflection High spatiotemporal resolution Poor penetration depth
US								
Spherical microparticle / magnetic propulsion	/	100 μm	Real-time (fps>100 Hz)	In vitro (2x2 cm water chamber)	High	Low-Medium	Khalil <i>et al.</i> 2014 ¹⁴⁷	Real-time Cheap Tissue imaging
Tumbling microrobot / magnetic propulsion	/	800 μm	Real-time (fps>100 Hz)	Ex vivo (<1cm, dissected colon)			Bi <i>et al.</i> 2019 ¹⁵⁰	Poor spatial resolution and contrast
Hybrid Techniques								
Magnetic microtubes / magnetic propulsion	AuNRs	Single (100 μm in length)	Real-time (10 fps)	Ex vivo (~1 cm deep)	High	Low-medium	*Aziz <i>et al.</i> 2019 ¹⁶⁶	PAI Real-time Improved resolution and penetration depth
Magnetic microparticles / magnetic propulsion	/	Single and swarm (100 μm in diameter)	Real-time PA (5-20 fps)	In vivo (mouse bladder and uterus)			*Aziz <i>et al.</i> 2020	Dual US/PAI Anatomical and functional imaging

*) The results have been presented in this thesis.

The optical imaging methods based on fluorescence or reflection carry high spatiotemporal resolution but have reduced tissue penetration which limits their application to sub-skin/superficial levels. Spatial resolution degrades significantly with depth due to pronounced light scattering as presented in first part of this thesis. On the contrary, small sized MNRs or the group of nanorobot with same size must be easy in tracking and imaging on sub-skin level thin tissues. But, to track small sized robot, an effective tracking and imaging way having higher resolution and penetration depth still needs to be developed. In this regard, PAI was suggested, by our group in 2017, as a promising tool to image single or few MNRs in deep tissues, in real-time³ and it appears as a favorable way for imaging MNRs inside human body. Fortunately, part of incident photons in deep tissue can be converted into US waves, which are scattered much less (~3 times less than photons).^{199,200} Absorption of photons thermoelastically induces pressure waves through the photoacoustic effect and images are reconstructed on-board by detecting the induced pressure waves.

In second part of this thesis, we reported, for the first time, the use of PAI for real-time tracking of a single magnetically-driven micromotor (100 μm in length) down to 1 cm depth in *ex vivo* chicken breast and phantoms. The localization of distinct micromotors was accomplished with an average error of ~100 μm in tissue-mimicking phantoms. We also presented real-time PAI of a single moving microtube in 3D. By coating the micromotors surface with gold nanorods (AuNRs) it was possible to enhance the contrast and the image quality thanks to the sharp and tunable absorption spectrum of AuNRs in the NIR region.

Until now, although a lot of advancement has been carried out in development of synthetic MNRs but these devices translation in the clinical applications is still obstructed due to the absence of *in vivo* imaging methods.³ Furthermore, the *in vivo* environments carry dynamic, heterogeneous and complex systems that are rich with biomechanical forces such as blood flow, body motion, heart beating or lung expansion.²¹² The accurate movement of such MNRs in a highly complex or dynamic environment followed by their tracking is highly challenging. Thus, efforts are required in development of imaging tools for such propelling MNRs in order to control their movement and localization in biological environments. Such control will lead to various medicinal applications including targeted drug delivery, transport, loading, tissue diagnosis and biomedical imaging at specific body site that has limited access.

To address one of these challenges, in last part of thesis, we present real-time imaging of single moving micromotor in *in vivo* is prerequisite for various biomedical applications. We implemented a hybrid HFUS and PA imaging system to carry out functional and structural imaging of swimming micromotors deep in the bladder and

uterus of a mice model. Single or few micromotors were successfully visualized in phantoms, *ex vivo*, and *in vivo* environments. US imaging showed clear boundaries among different types of organs and precisely identified the position of the catheter (with micromotors) in the body with real-time feedback, improving the accuracy of the procedure and avoiding tissue damaging during catheterization. In US images, internal structures like a bladder and uterus were visible to inject the micromotors while the PA images displayed the optical absorption characteristics of tissues and microstructures in mice.

Our results showed that the hybrid imaging mode provided from one side the volumetric US image and the PA distribution map of hemoglobins in the region of interest and resolved the micromotors from the signal of the surrounding tissues. HFUS was suitable for the real-time monitoring of the catheterization and localization of the target organ to deliver the micromotors, while PA allowed a reliable monitoring of the injected micromotors. The sensitivity of the hybrid system in the tissue enabled it to capture and discriminate the distinct optical contrast between endogenous chromophores and the micromotors, being of crucial importance when identifying MNRs position in a complex biological environment with poor contrast.

To translate this technology to humans and despite all the ethical discussions around the employment of medical microrobots which will arise in the next years, there are some technical limitations which need to be solved such as the penetration depth with micrometric resolution. Biodegradability is another prerequisite. There have been few attempts of biocompatible micromotors for *in vivo* drug-delivery applications^{4,5} and eventually, the micromotors should clear the body after performing an assigned task without any diverse effects. A preliminary study of micromotors using hybrid HFUS and PA system and an envisioned application in the field of supervised cargo-delivery is presented. This hybrid system is a powerful tool in addressing various imaging challenges of micromotors that require correlation with molecular and biological data, opening up a new horizon for imaging of medical microrobots in living organisms.

7.2 Future Perspectives

While addressing future research in this field, it is worth considering that swarm control somehow smooths the technical requirements needed for MNRs imaging. In real clinical settings and therapeutic paradigms, probably MNRs swarm or larger carriers transporting multiple cells will be likely employed to effectively deliver the required therapy to the target region. Due to their increased spot size, swarms of MNRs

relax the requirements for high spatial resolution. In addition, swarms can potentially enhance the contrast between MNRs and soft tissue and enable a more robust localization within the body. In fact, tissue intrinsic contrast and physiological motions (e.g. breathing, heart beating) pose an additional challenge in tracking moving MNRs *in vivo*, which calls for the development of novel and efficient contrast mechanisms to equip the MNRs with. This considered, swarm control appears as a promising strategy due to enhanced contrast to some imaging techniques, and for the easiness of embedding higher doses of the contrast agent within the swarm formations.

As highlighted in the previous sections, no single imaging technique that can outperform all the others. Instead, cleverly designed hybrid imaging techniques and innovative labels are being explored to move the technological borders and pave the way towards new exciting application areas. Such perspectives (labels for MNRs and imaging concepts) are presented in the last sub-section to conclude this thesis.

7.2.1 Contrats Enhancing Labels

One of the big difficulties and challenges for *in vivo* MNRs applications is performing non-invasive, real-time, deep-tissue, high-resolution and 3D imaging. Scientists are currently working to improve several imaging techniques and there is a need of suitable contrast agents that can significantly enhance imaging quality. Some of the limitations of current imaging techniques for the tracking of MNRs can be mitigated by incorporating novel and suitable contrast agents varying by imaging modality.

Optical imaging uses the first biological window with a wavelength range from 700 to 950 nm (NIR-I), and recent advances suggest the use of the second biological window (NIR-II, 1000-1400 nm) for deeper tissue penetration, reduced autofluorescence, minimum photon scattering and better SNR.^{69,213} Almost 16 years ago, simulations suggested it would be possible to improve SNR by 100-fold using fluorophores with emission peaks at around 1320 nm (NIR-II).²¹⁴ Since then, there was not much progress due to the lack of biocompatible fluorescent labels in that range. Early reports were mainly focused on II-VI (CdTe and HgTe),²¹⁵ IV-VI (PbS and PbSe)²¹⁶ and III-V (InAs)²¹⁷ QDs. However, the intrinsic toxic nature of Pb, Cd, and As made them unfit for prolonged *in vivo* applications. A recent class of biocompatible QDs, I-VI (Ag₂S and Ag₂Se) emitting in NIR-II is demonstrated as a promising fluorescent probe.^{218,219} Such QDs show good biocompatibility, high performance and no substantial toxicity. MNRs labelled with these QDs, can emit light in NIR-II and act as an asset for future deep tissue *in vivo* FI.

US imaging offers real-time monitoring and deep tissue penetration but lacks in high spatial resolution. To improve this, future research should focus on functionalizing MNRs with suitable contrast agents, e.g. microbubbles and/or gas vesicles, to discriminate them from the surrounding environment. Promising results in this direction were reported in a recent Nature paper.²²⁰ Clusters of micro-organisms (cells, bacteria, vesicles), at 0.1% volumetric concentrations, were labelled with acoustic reporter genes and visualized *in-vivo* in mammalian hosts with a resolution of 100 μm .

PAI is suitable to distinguish target MNRs (refer to Chapter 5 and 0) from the surrounding tissues (~1-2 cm depth) and is mainly utilizing conventional NIR-I window. One possibility is to shift the excitation light from traditional NIR-I to NIR-II window for deeper tissue penetration and improved contrast. Second, PA contrast agents are mostly composed of inorganic materials and the development of organic NIR-II agents can provide new opportunities for deep *in vivo* imaging of MNRs. An excellent PA contrast agent should possess NIR-II absorption peak, good photostability, high-molar extinction coefficient, low toxicity, high target affinity and biocompatibility.²²¹

7.2.2 Novel Imaging Concepts

Modern imaging techniques that take advantage of different physical principles to gain in both spatial resolution and penetration depths are nowadays in the pre-clinical stage (e.g. PAI). These hybrid techniques seem promising for testing MNRs *in vivo* while controlling their motion and therapeutic tasks performance. Scientists from different disciplines are working on manipulating light, sound, and magnetic fields to overcome the diffraction and scattering limitations of current techniques. This can be possible by employing new hybrid techniques or by functionalizing the MNRs with absorbers, emitters or reflectors thus paving the way towards improved sensitivity and contrast. In this context, novel or unexplored hybrid imaging concepts should be considered for the tracking of MNRs.

Acousto-optic imaging (AOI)^{222,223} is based on the acousto-optic effect²²⁴ and does not require any optical absorption (differently from PAI). US waves when propagating through an illuminated area, induce changes in the tissue refractive index and the objects' position, resulting in the formation of side-bands in scattered light. The AOI concept was first proposed by François Micheron and Daniel Dolphi in 1989. The technique employs a focused US beam to modulate light inside the target area. Focused US is generated by an external transducer and the modulated light from the

target is recorded outside the sample using interferometry-based approaches²²³ thus enabling the reconstruction of light intensity crossing the sample.

Magneto-optic imaging (MOI) is another hybrid imaging technique that combines an electromagnetic effect (eddy current or magnetic flux leakage) and the Faraday effect to generate a two-dimensional image. This technique was first proposed and developed by Fitzpatrick and Shih et al. in the 1990s.²²⁵ The propagation of light through a magnetic field is used to image target objects (e.g. defects or cracks in the surface of an object). So far, MOI has applications in detecting surface defects or cracks²²⁶ and was mainly dedicated to identify defects/cracks in thin films.²²⁷ By taking advantage of this, the MNRs can be designed with small cracks/defects during the fabrication process using various lithography techniques (e.g. photolithography, 3D lithography, e-beam lithography or stamp printers). Future study shall focus on imaging magnetic MNRs and fabricating suitable designs of such robots thus sufficient reflected polarized light is detected from the target robot for MOI visualization. Additionally, image processing methods should also be improved to enhance MOI system for better sensitivity and image resolution.

Magneto-acoustic tomography (MAI) employs high frequency (MHz range) pulsed magnetic fields to induce vibrations within tissues loaded with magnetic NPs. Particles vibrations produce mechanical waves which are registered through an external transducer and processed to reconstruct the magnetic material distribution. In MAI the transducer is only used as a receiver. This allows the MAI to have improved imaging bandwidth, limited mainly by the receiving bandwidth of the transducer, leading to better resolution. In addition, as compared to traditional US imaging, acoustic waves in MAI travel shorter paths and experience reduced attenuation in tissues, which leads to improved imaging depth.

Since optical techniques suffer from low penetration depth due to pronounced photon scattering, in this regard, **wavefront shaping** is an interesting concept which can be used in most optical methods to enhance their imaging depths. This method uses coherent light that scatters during propagation through tissues forms a speckle pattern. The random speckle pattern can be imaged as long as the scattering medium is static.²²⁸⁻²³² In this regard, spatial light modulators (SLMs) play a role which are pixelated devices that enable to manipulate or shape the phase of light. If an appropriate mask is displayed on the SLM, it is possible to remove the influence of a scattered field or to pre-shape the incident wavefront to achieve targeted delivery of a light-field distribution through thick scattering tissues.^{193,228,231-233} The huge technological and methodological progress of wavefront shaping techniques allows targeted light delivery deep into or through thick biological tissues. It was shown that

even entirely scattered light can be controlled and used for imaging or focusing through thick scattering tissues. The only pre-condition is that the mask that is displayed on the SLM is appropriate and fulfills the desired task. It is by far the greatest challenge to obtain information on this phase mask and many solutions like optical phase conjugation,^{233–236} iterative optimization wavefront shaping,^{237,238} and transmission matrix-based^{239,240} approaches have been used to achieve this task. This approach can be a promising tool that will surely lead to further unique microscopy techniques, enabling imaging in deep tissues.

Finally, interesting perspectives can be envisioned by the integration of functional materials such as magnetostrictive²⁴¹ or magnetoelectric²⁴² composites, which may enhance US signal or even produce unique signatures for the detection of MNRs. Furthermore, smart materials should be investigated to explore the use of these phenomena in microrobotics applications.

Disclaimer:

Parts of results presented in this chapter have been published in ACS Nano with the following permissions.

“Reprinted with permission from [A. Aziz, S. Pane, V. Iacovacci, N. Koukourakis, J. W. Czarske, A. Menciassi, M. Medina-Sánchez and O. G. Schmidt, “Medical Imaging of Microrobots: Toward In Vivo Applications” ACS Nano, 14 (9), 10865-10893, 2020]. Copyright [2019] American Chemical Society.”

8 REFERENCES

1. Feynman, R. There's plenty of room at the bottom. *Eng. Sci.* **23**, 22–36 (1960).
2. Bandari, V. K. *et al.* A flexible microsystem capable of controlled motion and actuation by wireless power transfer. *Nat. Electron.* **3**, 172–180 (2020).
3. Medina-Sánchez, M. & Schmidt, O. G. Medical microbots need better imaging and control. *Nature* **545**, 406–408 (2017).
4. Yan, X. *et al.* Multifunctional biohybrid magnetite microrobots for imaging-guided therapy. *Sci. Robot.* **2**, eaaq1155 (2017).
5. Wu, Z. *et al.* A microrobotic system guided by photoacoustic computed tomography for targeted navigation in intestines in vivo. *Sci. Robot.* **4**, eaax0613 (2019).
6. Solovev, A. A., Mei, Y., Ureña, E. B., Huang, G. & Schmidt, O. G. Catalytic microtubular jet engines self-propelled by accumulated gas bubbles. *Small* **5**, 1688–1692 (2009).
7. Sanchez, S., Soler, L. & Katuri, J. Chemically powered micro- and nanomotors. *Angew. Chemie - Int. Ed.* **54**, 1414–1444 (2015).
8. Sun, J., Mathesh, M., Li, W. & Wilson, D. A. Enzyme-Powered Nanomotors with Controlled Size for Biomedical Applications. *ACS Nano* **13**, 10191–10200 (2019).
9. Villa, K. *et al.* Cooperative Multifunctional Self-Propelled Paramagnetic Microrobots with Chemical Handles for Cell Manipulation and Drug Delivery. *Adv. Funct. Mater.* **28**, 1804343 (2018).
10. Zhou, M. *et al.* Self-Propelled and Targeted Drug Delivery of Poly(aspartic acid)/Iron–Zinc Microrocket in the Stomach. *ACS Nano* **13**, 1324–1332 (2019).
11. Chen, C., Soto, F., Karshalev, E., Li, J. & Wang, J. Hybrid Nanovehicles: One Machine, Two Engines. *Adv. Funct. Mater.* **29**, 1806290 (2019).
12. Llopis-Lorente, A. *et al.* Enzyme-Powered Gated Mesoporous Silica Nanomotors for On-Command Intracellular Payload Delivery. *ACS Nano* **13**, 12171–12183 (2019).
13. Srivastava, S. K., Medina-Sánchez, M. & Schmidt, O. G. Autonomously propelled microscavengers for precious metal recovery. *Chem. Commun.* **53**, 8140–8143 (2017).
14. Chen, X. Z. *et al.* Small-Scale Machines Driven by External Power Sources. *Adv. Mater.* **30**, 1–22 (2018).
15. Khalil, I. S. M., Dijkslag, H. C., Abelman, L. & Misra, S. MagnetoSperm: A microrobot that navigates using weak magnetic fields. *Appl. Phys. Lett.* **104**, (2014).

16. Medina-Sánchez, M., Schwarz, L., Meyer, A. K., Hebenstreit, F. & Schmidt, O. G. Cellular Cargo Delivery: Toward Assisted Fertilization by Sperm-Carrying Micromotors. *Nano Lett.* **16**, 555–561 (2016).
17. Srivastava, S. K., Medina-Sánchez, M., Koch, B. & Schmidt, O. G. Medibots: Dual-Action Biogenic Microdaggers for Single-Cell Surgery and Drug Release. *Adv. Mater.* **28**, 832–837 (2016).
18. Hu, W., Lum, G. Z., Mastrangeli, M. & Sitti, M. Small-scale soft-bodied robot with multimodal locomotion. *Nature* **554**, 81–85 (2018).
19. Schuerle, S. *et al.* Synthetic and living micropropellers for convection-enhanced nanoparticle transport. *Sci. Adv.* **5**, 1–11 (2019).
20. Wang, W. *et al.* Acoustic Propulsion of Nanorod Motors Inside Living Cells. *Angew. Chemie Int. Ed.* **53**, 3201–3204 (2014).
21. Ahmed, D., Dillinger, C., Hong, A. & Nelson, B. J. Artificial Acousto-Magnetic Soft Microswimmers. *Adv. Mater. Technol.* **2**, 1–5 (2017).
22. Ahmed, D. *et al.* Neutrophil-inspired propulsion in a combined acoustic and magnetic field. *Nat. Commun.* **8**, 1–8 (2017).
23. Liu, M., Zentgraf, T., Liu, Y., Bartal, G. & Zhang, X. Light-driven nanoscale plasmonic motors. *Nat. Nanotechnol.* **5**, 570 (2010).
24. Wu, Z. *et al.* Near-Infrared Light-Triggered “On/Off” Motion of Polymer Multilayer Rockets. *ACS Nano* **8**, 6097–6105 (2014).
25. Iacovacci, V. *et al.* Polydimethylsiloxane films doped with NdFeB powder: magnetic characterization and potential applications in biomedical engineering and microrobotics. *Biomed. Microdevices* **17**, (2015).
26. Magdanz, V., Sanchez, S. & Schmidt, O. G. Development of a sperm-flagella driven micro-bio-robot. *Adv. Mater.* **25**, 6581–6588 (2013).
27. Magdanz, V. *et al.* Spermatozoa as Functional Components of Robotic Microswimmers. *Adv. Mater.* **29**, 1–18 (2017).
28. Stanton, M. M., Simmchen, J., Ma, X., Miguel-López, A. & Sánchez, S. Biohybrid Janus Motors Driven by *Escherichia coli*. *Adv. Mater. Interfaces* **3**, (2016).
29. Erin, O., Gilbert, H. B., Tabak, A. F. & Sitti, M. Elevation and Azimuth Rotational Actuation of an Untethered Millirobot by MRI Gradient Coils. *IEEE Trans. Robot.* **35**, 1323–1337 (2019).
30. Park, B. W., Zhuang, J., Yasa, O. & Sitti, M. Multifunctional Bacteria-Driven Microswimmers for Targeted Active Drug Delivery. *ACS Nano* **11**, 8910–8923 (2017).

31. Schwarz, L., Medina-Sánchez, M. & Schmidt, O. G. Hybrid BioMicromotors. *Appl. Phys. Rev.* **4**, 031301 (2017).
32. Xu, H. *et al.* Sperm-Hybrid Micromotor for Targeted Drug Delivery. *ACS Nano* **12**, 327–337 (2018).
33. Xi, W. *et al.* Rolled-up magnetic microdrillers: towards remotely controlled minimally invasive surgery. *Nanoscale* **5**, 1294–7 (2013).
34. Wang, J., Dong, R., Wu, H., Cai, Y. & Ren, B. A Review on Artificial Micro/Nanomotors for Cancer-Targeted Delivery, Diagnosis, and Therapy. *Nano-Micro Lett.* **12**, (2020).
35. Medina-Sánchez, M., Xu, H. & Schmidt, O. G. Micro- and nano-motors: The new generation of drug carriers. *Ther. Deliv.* **9**, 303–316 (2018).
36. Nelson, B. J., Kaliakatsos, I. K. & Abbott, J. J. Microrobots for Minimally Invasive Medicine. *Annu. Rev. Biomed. Eng.* **12**, 55–85 (2010).
37. Guix, M., Weiz, S. M., Schmidt, O. G. & Medina-Sánchez, M. Self-Propelled Micro/Nanoparticle Motors. *Part. Part. Syst. Character.* **35**, 1–31 (2018).
38. Chałupniak, A., Morales-Narváez, E. & Merkoçi, A. Micro and nanomotors in diagnostics. *Adv. Drug Deliv. Rev.* **95**, 104–116 (2015).
39. Srivastava, S. K., Clergeaud, G., Andresen, T. L. & Boisen, A. Micromotors for drug delivery in vivo: The road ahead. *Adv. Drug Deliv. Rev.* **138**, 41–55 (2019).
40. Ricotti, L., Cafarelli, A., Iacovacci, V., Vannozzi, L. & Menciassi, A. Advanced Micro-Nano-Bio Systems for Future Targeted Therapies. *Curr. Nanosci.* **11**, 144–160 (2015).
41. Iacovacci, V. *et al.* Untethered magnetic millirobot for targeted drug delivery. *Biomed. Microdevices* **17**, 63 (2015).
42. Gao, W. *et al.* Artificial micromotors in the mouse’s stomach: A step toward in vivo use of synthetic motors. *ACS Nano* **9**, 117–123 (2015).
43. Ghost, A., Fischer, P., Ghosh, A. & Fischer, P. Controlled propulsion of artificial magnetic nanostructured propellers. *Nano Lett.* **9**, 2243–2245 (2009).
44. Zhang, L. *et al.* Artificial bacterial flagella: Fabrication and magnetic control. *Appl. Phys. Lett.* **94**, 64107 (2009).
45. Zhang, L., Peyer, K. E. & Nelson, B. J. Artificial bacterial flagella for micromanipulation. *Lab Chip* **10**, 2203–2215 (2010).
46. Servant, A., Qiu, F., Mazza, M., Kostarelos, K. & Nelson, B. J. Controlled in vivo swimming of a swarm of bacteria-like microrobotic flagella. *Adv. Mater.* **27**, 2981–2988 (2015).

47. Hess, H. & Bachand, G. D. Biomolecular motors. *Mater. Today* **8**, 22–29 (2005).
48. Martel, S., Mohammadi, M., Felfoul, O., Zhao Lu & Pouponneau, P. Flagellated magnetotactic bacteria as controlled MRI-trackable propulsion and steering systems for medical nanorobots operating in the human microvasculature. *Int. J. Rob. Res.* **28**, 571–582 (2009).
49. Magdanz, V., Sanchez, S. & Schmidt, O. G. Development of a sperm-flagella driven micro-bio-robot. *Adv. Mater.* **25**, 6581–6588 (2013).
50. Pouponneau, P., Leroux, J.-C., Soulez, G., Gaboury, L. & Martel, S. Co-encapsulation of magnetic nanoparticles and doxorubicin into biodegradable microcarriers for deep tissue targeting by vascular MRI navigation. *Biomaterials* **32**, 3481–3486 (2011).
51. Santhi, V., Acharjya, D. P. & Ezhilarasan, M. *Emerging Technologies in Intelligent Applications for Image and Video Processing*. (IGI Global, 2016).
52. Vilela, D. *et al.* Medical Imaging for the Tracking of Micromotors. *ACS Nano* **12**, 1220–1227 (2018).
53. Sánchez, A., Magdanz, V., Schmidt, O. G. & Misra, S. Magnetic control of self-propelled microjets under ultrasound image guidance. *Proc. IEEE RAS EMBS Int. Conf. Biomed. Robot. Biomechatronics* 169–174 (2014)
doi:10.1109/BIOROB.2014.6913771.
54. Xu, Z. *et al.* X-ray Powered Micromotors. *ACS Appl. Mater. Interfaces* (2019)
doi:10.1021/acsami.9b00174.
55. Li, J. *et al.* Enteric Micromotor Can Selectively Position and Spontaneously Propel in the Gastrointestinal Tract. *ACS Nano* **10**, 9536–9542 (2016).
56. de Ávila, B. E.-F. *et al.* Micromotor-enabled active drug delivery for in vivo treatment of stomach infection. *Nat. Commun.* **8**, 272 (2017).
57. Ongaro, F., Niehoff, D., Mohanty, S. & Misra, S. A Contactless and Biocompatible Approach for 3D Active Microrobotic Targeted Drug Delivery. *Micromachines* **10**, 504 (2019).
58. Yu, J. *et al.* Active generation and magnetic actuation of microrobotic swarms in bio-fluids. *Nat. Commun.* **10**, 5631 (2019).
59. Felfoul, O. *et al.* Magneto-aerotactic bacteria deliver drug-containing nanoliposomes to tumour hypoxic regions. *Nat. Nanotechnol.* **11**, 941–947 (2016).
60. Martel, S. *et al.* Automatic navigation of an untethered device in the artery of a living animal using a conventional clinical magnetic resonance imaging system. *Appl. Phys. Lett.* **90**, (2007).

61. Martel, S. *et al.* MRI-based medical nanorobotic platform for the control of magnetic nanoparticles and flagellated bacteria for target interventions in human capillaries. *Int. J. Rob. Res.* **28**, 1169–1182 (2009).
62. Paulus, M. J., Gleason, S. S., Kennel, S. J., Hunsicker, P. R. & Johnson, D. K. High resolution X-ray computed tomography: an emerging tool for small animal cancer research. *Neoplasia* **2**, 62–70 (2000).
63. Convert, L. *et al.* Real-Time Microfluidic Blood-Counting System for PET and SPECT Preclinical Pharmacokinetic Studies. *J. Nucl. Med.* **57**, 1460–6 (2016).
64. Iacovacci, V. *et al.* High-Resolution SPECT Imaging of Stimuli-Responsive Soft Microrobots. *Small* **15**, (2019).
65. Gigan, S. Optical microscopy aims deep. *Nat. Photonics* **11**, 14–16 (2017).
66. Ntziachristos, V. Going deeper than microscopy: the optical imaging frontier in biology. *Nat. Methods* **7**, 603–614 (2010).
67. Li, D. *et al.* Automated in vivo Navigation of Magnetic-driven Microrobots Using OCT Imaging Feedback. *IEEE Trans. Biomed. Eng.* **67**, 2349–2358 (2019).
68. Zhang, J., Liu, J., Wang, L. M., Li, Z. Y. & Yuan, Z. Retroreflective-type Janus microspheres as a novel contrast agent for enhanced optical coherence tomography. *J. Biophotonics* **10**, 878–886 (2017).
69. Smith, A. M., Mancini, M. C. & Nie, S. Bioimaging: second window for in vivo imaging. *Nat. Nanotechnol.* **4**, 710–711 (2009).
70. Loebich, O. The optical properties of gold. *Gold Bull.* **5**, 2–10 (1972).
71. White, J. G. & Amos, W. B. Confocal microscopy comes of age. *Nature* **328**, 183–184 (1987).
72. Koukourakis, N. *et al.* Axial scanning in confocal microscopy employing adaptive lenses (CAL). *Opt. Express* **22**, 6025 (2014).
73. Huang, D. *et al.* Optical Coherence Tomography. *Science (80-.)*. **254**, 1178–1181 (1991).
74. Chong, S. P. *et al.* Noninvasive, in vivo imaging of subcortical mouse brain regions with 17 μm optical coherence tomography. *Opt. Lett.* **40**, 4911 (2015).
75. Li, B. *et al.* Impact of temporal resolution on estimating capillary RBC-flux with optical coherence tomography. *Journal of biomedical optics* vol. 22 16014 (2017).
76. Yaqoob, Z., Wu, J. & Yang, C. Spectral domain optical coherence tomography: a better OCT imaging strategy. *Biotechniques* **39**, S6–S13 (2005).
77. Han, Y. D. *et al.* Retroreflective Janus Microparticle as a Nonspectroscopic Optical Immunosensing Probe. *ACS Appl. Mater. Interfaces* **8**, 10767–10774 (2016).

78. Ullrich, F. *et al.* Mobility Experiments With Microrobots for Minimally Invasive Intraocular Surgery. *Invest. Ophthalmol. Vis. Sci.* **54**, 2853–2863 (2013).
79. Jabłoński, A. Efficiency of Anti-Stokes Fluorescence in Dyes. *Nature* **131**, 839–840 (1993).
80. Helmchen, F. & Denk, W. Deep tissue two-photon microscopy. *Nat. Methods* **2**, 932–940 (2005).
81. ICNIRP. Icnirp guidelines on limits of exposure to incoherent visible and infrared radiation. *Health Phys.* **71**, 804–819 (2013).
82. Steager, E. B. *et al.* Automated biomanipulation of single cells using magnetic microrobots. *Int. J. Rob. Res.* **32**, 346–359 (2013).
83. Nat, A. Y., Ueno, T. & Nagano, T. Fluorescent probes for sensing and imaging. *Nat. Publ. Gr.* **8**, 642–645 (2011).
84. Schnermann, M. J. Organic dyes for deep bioimaging. *Nature* **551**, 176 (2017).
85. Walling, M. A., Novak, J. A. & Shepard, J. R. E. Quantum dots for live cell and in vivo imaging. *International Journal of Molecular Sciences* vol. 10 441–491 (2009).
86. Alivisatos, A. P. Semiconductor Clusters, Nanocrystals, and Quantum Dots. *Science (80-.)*. **271**, 933–937 (1996).
87. Fernandez-Bravo, A. *et al.* Continuous-wave upconverting nanoparticle microlasers. *Nat. Nanotechnol.* **13**, 572–577 (2018).
88. Ashoori, R. C. Electrons in artificial atoms. *Nature* **379**, 413–419 (1996).
89. Bruchez, M., Moronne, M., Gin, P., Weiss, S. & Alivisatos, A. P. Semiconductor Nanocrystals as Fluorescent Biological Labels. *Science (80-.)*. **281**, 2013–2016 (1998).
90. Pai, J.-H. *et al.* Photoresist with Low Fluorescence for Bioanalytical Applications. *Anal. Chem.* **79**, 8774–8780 (2007).
91. Jurado-Sanchez, B., Pacheco, M., Rojo, J. & Escarpa, A. Magnetocatalytic Graphene Quantum Dots Janus Micromotors for Bacterial Endotoxin Detection. *Angew. Chem. Int. Ed. Engl.* **56**, 6957–6961 (2017).
92. Niemz, M. H. *Laser-Tissue Interactions*. (Springer, Cham, 2019). doi:<https://doi.org/10.1007/978-3-030-11917-1>.
93. Keiser G. Light-Tissue Interactions. in *In: Biophotonics. Graduate Texts in Physics*. Springer, Singapore (2016). doi:https://doi.org/10.1007/978-981-10-0945-7_6.
94. Beauvoit, B., Evans, S. M., Jenkins, T. W., Miller, E. E. & Chance, B. Correlation between the light scattering and the mitochondrial content of normal tissues and

- transplantable rodent tumors. *Anal. Biochem.* **226**, 167–174 (1995).
95. Rayleigh, Lord. On the electromagnetic theory of light. *London, Edinburgh, Dublin Philos. Mag. J. Sci.* **12**, 81–101 (1881).
 96. Strutt, J. W. On the scattering of light by small particles. *London, Edinburgh, Dublin Philos. Mag. J. Sci.* **41**, 447–454 (1871).
 97. Mie, G. Beiträge zur Optik trüber Medien, speziell kolloidaler Metallösungen. *Ann. Phys.* **330**, 377–445 (1908).
 98. Bohren, C. F. and Huffman, D. R. Absorption and Scattering of Light by Small Particles. *A Wiley Interscience Publication, John Wiley & Sons, Inc.* 57–81 (1983) doi:doi:10.1002/9783527618156.ch3.
 99. Taruttis, A. & Ntziachristos, V. Advances in real-time multispectral optoacoustic imaging and its applications. *Nat. Photonics* **9**, 219–227 (2015).
 100. Omar, M., Aguirre, J. & Ntziachristos, V. Optoacoustic mesoscopy for biomedicine. *Nat. Biomed. Eng.* **3**, 354–370 (2019).
 101. Zhao, T., Desjardins, A. E., Ourselin, S., Vercauteren, T. & Xia, W. Minimally invasive photoacoustic imaging: current status and future perspectives. *Photoacoustics* **16**, 100146 (2019).
 102. Beard, P. Biomedical photoacoustic imaging. *Interface Focus* **1**, 602–631 (2011).
 103. Alexander Graham Bell. THE PRODUCTION OF SOUND BY RADIANT ENERGY. *Am. Assos.* 598 (1880).
 104. Upputuri, P. K. & Pramanik, M. Recent advances toward preclinical and clinical translation of photoacoustic tomography: a review. *J. Biomed. Opt.* **22**, 41006 (2017).
 105. Zhou, Y., Yao, J. & Wang, L. V. Tutorial on photoacoustic tomography. *J. Biomed. Opt.* **21**, 61007 (2016).
 106. Cerussi, A. E. *et al.* Sources of absorption and scattering contrast for near-infrared optical mammography. *Acad. Radiol.* **8**, 211–218 (2001).
 107. Attia, A. B. E. *et al.* Noninvasive real-time characterization of non-melanoma skin cancers with handheld optoacoustic probes. *Photoacoustics* **7**, 20–26 (2017).
 108. Zhou, Y. *et al.* Noninvasive Determination of Melanoma Depth using a Handheld Photoacoustic Probe. *J. Invest. Dermatol.* **137**, 1370–1372 (2017).
 109. Wu, D., Huang, L., Jiang, M. S. & Jiang, H. Contrast agents for photoacoustic and thermoacoustic imaging: A review. *Int. J. Mol. Sci.* **15**, 23616–23639 (2014).
 110. Oraevsky, A. A. ‘Contrast agents for optoacoustic imaging: Design and biomedical applications’. *Photoacoustics* **3**, 1–2 (2015).

111. Xu, M. & Wang, L. V. Universal back-projection algorithm for photoacoustic computed tomography. *Phys. Rev. E - Stat. Nonlinear, Soft Matter Phys.* (2005) doi:10.1103/PhysRevE.71.016706.
112. Lutzweiler, C., Deán-Ben, X. L. & Razansky, D. Expediting model-based optoacoustic reconstructions with tomographic symmetries. *Med. Phys.* (2014) doi:10.1118/1.4846055.
113. Razansky, D. *et al.* Multispectral opto-acoustic tomography of deep-seated fluorescent proteins in vivo. *Nat. Photonics* (2009) doi:10.1038/nphoton.2009.98.
114. Ntziachristos, V. & Razansky, D. Molecular imaging by means of multispectral optoacoustic tomography (MSOT). *Chem. Rev.* **110**, 2783–2794 (2010).
115. Merčep, E., Deán-Ben, X. L. & Razansky, D. Imaging of blood flow and oxygen state with a multi-segment optoacoustic ultrasound array. *Photoacoustics* **10**, 48–53 (2018).
116. Prakash, J., Raju, A. S., Shaw, C. B., Pramanik, M. & Yalavarthy, P. K. Basis pursuit deconvolution for improving model-based reconstructed images in photoacoustic tomography. *Biomed. Opt. Express* **5**, 1363–1377 (2014).
117. Kruger, R. A., Reinecke, D. R. & Kruger, G. A. Thermoacoustic computed tomography-technical considerations. *Med. Phys.* **26**, 1832–1837 (1999).
118. Huang, H., Bustamante, G., Peterson, R. & Ye, J. Y. An adaptive filtered back-projection for photoacoustic image reconstruction. *Med. Phys.* **42**, 2169–2178 (2015).
119. Haltmeier, M., Neumann, L. & Rabanser, S. Single-stage reconstruction algorithm for quantitative photoacoustic tomography. *Inverse Probl.* (2015) doi:10.1088/0266-5611/31/6/065005.
120. Dean-Ben, X. L. *et al.* Volumetric hand-held optoacoustic angiography as a tool for real-time screening of dense breast. *J. Biophotonics* **9**, 253–259 (2016).
121. Favazza, C. P., Wang, L. V & Cornelius, L. A. In vivo functional photoacoustic microscopy of cutaneous microvasculature in human skin. *J. Biomed. Opt.* **16**, 1–5 (2011).
122. Taruttis, A., Herzog, E., Razansky, D. & Ntziachristos, V. Real-time imaging of cardiovascular dynamics and circulating gold nanorods with multispectral optoacoustic tomography. *Opt. Express* **18**, 19592–19602 (2010).
123. Nasiriavanaki, M. *et al.* High-resolution photoacoustic tomography of resting-state functional connectivity in the mouse brain. *Proc. Natl. Acad. Sci.* **111**, 21–26 (2014).
124. Cui, H. & Yang, X. In vivo imaging and treatment of solid tumor using integrated

- photoacoustic imaging and high intensity focused ultrasound system. *Med. Phys.* **37**, 4777–4781 (2010).
125. Taruttis, A. *et al.* Optoacoustic Imaging of Human Vasculature: Feasibility by Using a Handheld Probe. *Radiology* **281**, 256–263 (2016).
 126. Deán-Ben, X. L., Bay, E. & Razansky, D. Functional optoacoustic imaging of moving objects using microsecond-delay acquisition of multispectral three-dimensional tomographic data. *Sci. Rep.* **4**, 1–6 (2014).
 127. Buehler, A., Diot, G., Volz, T., Kohlmeyer, J. & Ntziachristos, V. Imaging of fatty tumors: appearance of subcutaneous lipomas in optoacoustic images. *J. Biophotonics* **10**, 983–989 (2017).
 128. Xiang, L., Ahmad, M., Hu, X., Cheng, Z. & Xing, L. Label-Free Photoacoustic Cell-Tracking In Real-Time. *X-Acoustics Imaging Sens.* **1**, 18–22 (2014).
 129. Knieling, F. *et al.* Multispectral Optoacoustic Tomography for Assessment of Crohn's Disease Activity. *The New England journal of medicine* vol. 376 1292–1294 (2017).
 130. Lutzweiler, C. & Razansky, D. Optoacoustic imaging and tomography: Reconstruction approaches and outstanding challenges in image performance and quantification. *Sensors (Switzerland)* **13**, 7345–7384 (2013).
 131. Mallidi, S., Luke, G. P. & Emelianov, S. Photoacoustic Imaging in Cancer Detection, Diagnosis, and Treatment Guidance. *Trends Biotechnol.* **29**, 213–221 (2011).
 132. Manohar, S. & Razansky, D. Photoacoustics : a historical review Photoacoustics : a historical review. *Adv. Opt. Photonics* **8**, 586–617 (2016).
 133. Manohar, S., Ungureanu, C. & Van Leeuwen, T. G. Gold nanorods as molecular contrast agents in photoacoustic imaging: The promises and the caveats. *Contrast Media Mol. Imaging* **6**, 389–400 (2011).
 134. Hu, M. *et al.* Gold nanostructures: engineering their plasmonic properties for biomedical applications. *Chem. Soc. Rev.* **35**, 1084–1094 (2006).
 135. Weissleder, R. A clearer vision for in vivo imaging. *Nat. Biotechnol.* **19**, 316–317 (2001).
 136. Comenge, J. *et al.* Preventing Plasmon Coupling between Gold Nanorods Improves the Sensitivity of Photoacoustic Detection of Labeled Stem Cells in Vivo. *ACS Nano* **10**, 7106–7116 (2016).
 137. Jokerst, J. V., Cole, A. J., Van De Sompel, D. & Gambhir, S. S. Gold nanorods for ovarian cancer detection with photoacoustic imaging and resection guidance via Raman imaging in living mice. *ACS Nano* (2012) doi:10.1021/nn304347g.

138. Laufer, J. *et al.* In vivo preclinical photoacoustic imaging of tumor vasculature development and therapy. *J. Biomed. Opt.* **17**, 056016 (2012).
139. Park, S., Jang, J., Kim, J., Kim, Y. S. & Kim, C. Real-time Triple-modal Photoacoustic, Ultrasound, and Magnetic Resonance Fusion Imaging of Humans. *IEEE Trans. Med. Imaging* **36**, 1912–1921 (2017).
140. Lee, D. *et al.* In Vivo Near Infrared Virtual Intraoperative Surgical Photoacoustic Optical Coherence Tomography. *Sci. Rep.* **6**, (2016).
141. Kremkau, F. W. *Diagnostic ultrasound: principles and instruments.* (WB Saunders Philadelphia, 1998).
142. Calliada, F., Campani, R., Bottinelli, O., Bozzini, A. & Sommaruga, M. G. Ultrasound contrast agents: Basic principles. *Eur. J. Radiol.* **27**, S157–S160 (1998).
143. Nasoni, R. L. Temperature corrected speed of sound for use in soft tissue imaging. *Med. Phys.* **8**, 513–515 (1981).
144. Liebgott, H., Rodriguez-Molares, A., Cervenansky, F., Jensen, J. A. & Bernard, O. Plane-Wave Imaging Challenge in Medical Ultrasound. *IEEE Int. Ultrason. Symp. IUS 2016-Novem*, (2016).
145. Azhari, H. *Basics of biomedical ultrasound for engineers.* (John Wiley & Sons, 2010).
146. Hunt, J. W., Arditi, M. & Foster, F. S. Ultrasound Transducers for Pulse-Echo Medical Imaging. *IEEE Trans. Biomed. Eng.* **BME-30**, 453–481 (1983).
147. Khalil, I. S. M. M. *et al.* Magnetic-based closed-loop control of paramagnetic microparticles using ultrasound feedback. *IEEE Int. Conf. Robot. Autom.* 3807–3812 (2014) doi:10.1109/ICRA.2014.6907411.
148. Scheggi, S., Yoon, C. K., Ghosh, A., Gracias, D. H. & Misra, S. A GPU-accelerated model-based tracker for untethered submillimeter grippers. *Rob. Auton. Syst.* **103**, 111–121 (2018).
149. Dandan Li, Moonkwang Jeong, Eran Oren, Tingting Yu, T. Q. A Helical Microrobot with an Optimized Propeller-Shape for Propulsion in Viscoelastic Biological Media. *MDPI, Robot.* (2019).
150. Bi, C. *et al.* Tumbling magnetic microrobots for biomedical applications. in *Proceedings of MARSS 2019: 4th International Conference on Manipulation, Automation, and Robotics at Small Scales* 1–6 (2019). doi:10.1109/MARSS.2019.8860956.
151. Xie, H. *et al.* Reconfigurable magnetic microrobot swarm: Multimode transformation, locomotion, and manipulation. *Microrobots* 1–15 (2019).

152. Yigit, B., Alapan, Y. & Sitti, M. Programmable collective behavior in dynamically self-assembled mobile microrobotic swarms. *Adv. Sci.* **1801837**, (2019).
153. Yu, J., Wang, B., Du, X., Wang, Q. & Zhang, L. Ultra-extensible ribbon-like magnetic microswarm. *Nat. Commun.* **9**, 1–9 (2018).
154. Wang, Q., Yang, L., Yu, J., Wai, P. & Chiu, Y. Magnetic Navigation of a Rotating Colloidal Swarm Using Ultrasound Images. *IEEE* (2018).
155. Yu, J. *et al.* Characterizing Nanoparticle Swarms With Tuneable Concentrations for Enhanced Imaging Contrast. *IEEE Robot. Autom. Lett.* **4**, 2942–2949 (2019).
156. Qianqian Wang, Jiangfan Yu, K. Y. Disassembly and spreading of magnetic nanoparticle clusters on uneven surfaces. *Appl. Mater. Today* **1**, 1–6 (2019).
157. Magdanz, V. *et al.* IRONSperm: Sperm-templated soft magnetic microrobots. *Sci. Adv.* **6**, eaba5855 (2020).
158. Xing, J.-F., Zheng, M.-L. & Duan, X.-M. Two-photon polymerization microfabrication of hydrogels: an advanced 3D printing technology for tissue engineering and drug delivery. *Chem. Soc. Rev.* **44**, 5031–5039 (2015).
159. Göppert-Mayer, M. Über Elementarakte mit zwei Quantensprüngen. *Ann. Phys.* **401**, 273–294 (1931).
160. Kaiser, W. & Garrett, C. G. B. Two-Photon Excitation in CaF₂: Eu²⁺. *Phys. Rev. Lett.* **7**, 229–231 (1961).
161. Rumi, M. & Perry, J. W. Two-photon absorption: an overview of measurements and principles. *Adv. Opt. Photon.* **2**, 451–518 (2010).
162. K. S. S Harsha. *Principles of Physical Vapor Deposition of Thin Films (Elsevier, Great Britain, 2006)*. (2006).
163. S. Schiller and G. Jäsch. No Title. *Thin Solid Films* **54**, 9–21 (1978).
164. Giedrius LAUKAITIS, Julius DUDONIS, D. M. Deposition of YSZ Thin Films Using Electron Beam Evaporation Technique. *Mater. Sci.* **11**, 268–271 (2005).
165. Aziz, A. *et al.* Real-Time IR Tracking of Single Reflective Micromotors through Scattering Tissues. *Adv. Funct. Mater.* **29**, (2019).
166. Aziz, A., Medina-Sánchez, M., Claussen, J. & Schmidt, O. G. Real-Time Optoacoustic Tracking of Single Moving Micro-objects in Deep Phantom and Ex Vivo Tissues. *Nano Lett.* **19**, 6612–6620 (2019).
167. Wu, R. H. *et al.* A Facile Route to Tailoring Peptide-Stabilized Gold Nanoparticles Using Glutathione as a Synthon. 6754–6775 (2014)
doi:10.3390/molecules19056754.
168. Hadi, M., Amani, H., Akbar, A., Pazoki-toroudi, H. & Sedighimoghaddam, B.

- Sensing and Bio-Sensing Research Various methods of gold nanoparticles (GNPs) conjugation to antibodies. *SBSR* **9**, 17–22 (2016).
169. Sperling, R. A. & Parak, W. J. Surface modification, functionalization and bioconjugation of colloidal inorganic nanoparticles. *Philos. Trans. R. Soc. A Math. Phys. Eng. Sci.* **368**, 1333 LP – 1383 (2010).
 170. Conde, J. *et al.* Revisiting 30 years of biofunctionalization and surface chemistry of inorganic nanoparticles for nanomedicine. *Front. Chem.* **2**, 48 (2014).
 171. Wróbel, M. S., Popov, A. P., Bykov, A. V & Tuchin, V. V. Nanoparticle-free tissue-mimicking phantoms with intrinsic scattering. **7**, 2088–2094 (2016).
 172. Earle, M., Portu, G. De & Devos, E. African Federation for Emergency Medicine African Journal of Emergency Medicine Agar ultrasound phantoms for low-cost training without refrigeration Fanto^mes d ' e ^ chographie utilisant l ' agar-agar pour une formation a ` faible cou^t , sans re ^ frige. *African J. Emerg. Med.* **6**, 18–23 (2016).
 173. Haga, H. & Sasaki, S. Standard operating procedure to prepare agar phantoms. 6–11 (2016) doi:10.1088/1742-6596/733/1/012044.
 174. Jaime, R. A. O. *et al.* Fabrication methods of phantoms simulating optical and thermal properties. *Procedia Eng.* **59**, 30–36 (2013).
 175. Xia, Y. & Whitesides, G. M. Soft Lithography. *Annu. Rev. Mater. Sci.* **28**, 153–184 (1998).
 176. McMullan, D. Scanning electron microscopy 1928–1965. *Scanning* **17**, 175–185 (1995).
 177. Hitachi. World's Highest Resolution FE-SEM. (2011).
 178. Lownes Urbano, R. & Morss Clyne, A. An inverted dielectrophoretic device for analysis of attached single cell mechanics. *Lab Chip* **16**, 561–573 (2016).
 179. Wang, X. *et al.* Magnetic Measurement and Stimulation of Cellular and Intracellular Structures. *ACS Nano* **14**, 3805–3821 (2020).
 180. Demann, E. T. K., Stein, P. S. & Haubenreich, J. E. Gold as an implant in medicine and dentistry. *J. Long. Term. Eff. Med. Implants* **15**, 687–698 (2005).
 181. Shukla, R. *et al.* Biocompatibility of Gold Nanoparticles and Their Endocytotic Fate Inside the Cellular Compartment : A Microscopic Overview. 10644–10654 (2005) doi:10.1021/la0513712.
 182. Zingler, S., Erber, R., Lux, C. J., Seeberger, R. & Bister, D. Biocompatibility of gold and stainless steel chains used for forced eruption of impacted teeth e an in vitro investigation. *Oral Surgery, Oral Med. Oral Pathol. Oral Radiol.* **116**, 159–168

- (2013).
183. Fan, J. H., Hung, W. I., Li, W. T. & Yeh, J. M. *Biocompatibility Study of Gold Nanoparticles to Human Cells. IFMBE Proceedings* vol. 23 870–873 (2009).
 184. Stoudt, M. D. & Vedam, K. Retroreflection from spherical glass beads in highway pavement markings. 1: Specular reflection. *Appl. Opt.* **17**, 1855–1858 (1978).
 185. Mattsson, J. O.; Cavallin, C. Retroreflection of Light from Drop- Covered Surfaces and an Image-Producing Device for Registration of This Light. *Oikos. Oikos* **23**, 285–294 (1972).
 186. Steyerl, A., Malik, S. S. & Iyengar, L. R. Specular and diffuse reflection and refraction at surfaces. *Phys. B Phys. Condens. Matter* **173**, 47–64 (1991).
 187. Jacques, S. L. Optical properties of biological tissues: A review. *Phys. Med. Biol.* **58**, (2013).
 188. Qiu, T., Schamel, D., Mark, A. G. & Fischer, P. Active microrheology of the vitreous of the eye applied to nanorobot propulsion. in *Proceedings - IEEE International Conference on Robotics and Automation* 3801–3806 (Institute of Electrical and Electronics Engineers Inc., 2014). doi:10.1109/ICRA.2014.6907410.
 189. Wu, Z. *et al.* A swarm of slippery micropropellers penetrates the vitreous body of the eye. *Sci. Adv.* **4**, (2018).
 190. Chen, G. *et al.* Regulation of blood viscosity in disease prevention and treatment. *Chinese Sci. Bull.* **57**, 1946–1952 (2012).
 191. Tacar, O., Sriamornsak, P. & Dass, C. R. Doxorubicin: an update on anticancer molecular action, toxicity and novel drug delivery systems. *J. Pharm. Pharmacol.* **65**, 157–170 (2013).
 192. Song, M., Li, Y., Ning, A., Fang, S. & Cui, B. Silica nanoparticles as a carrier in the controlled release of florfenicol. *J. Drug Deliv. Sci. Technol.* **20**, 349–352 (2010).
 193. Koukourakis, N., Fregin, B., König, J., Büttner, L. & Czarske, J. W. Wavefront shaping for imaging-based flow velocity measurements through distortions using a Fresnel guide star. *Opt. Express* **24**, 22074–22087 (2016).
 194. Kuschmierz, R., Scharf, E., Koukourakis, N. & Czarske, J. W. Self-calibration of lensless holographic endoscope using programmable guide stars. *Opt. Lett.* **43**, 2997–3000 (2018).
 195. Stoffels, I. *et al.* Metastatic status of sentinel lymph nodes in melanoma determined noninvasively with multispectral optoacoustic imaging. *Sci. Transl. Med.* **7**, 317ra199--317ra199 (2015).
 196. Ho, C. J. H. *et al.* Multifunctional Photosensitizer-Based Contrast Agents for

- Photoacoustic Imaging. *Sci. Rep.* **4**, 5342 (2014).
197. Wang, L. V & Gao, L. Photoacoustic microscopy and computed tomography: from bench to bedside. *Annu. Rev. Biomed. Eng.* **16**, 155–185 (2014).
 198. Medina-Sánchez, M. *et al.* Rapid 3D printing of complex polymeric tubular catalytic micromotors. *2016 Int. Conf. Manip. Autom. Robot. Small Scales, MARSS 2016* 1–6 (2016) doi:10.1109/MARSS.2016.7561721.
 199. Wang, L. V & Hu, S. Photoacoustic Tomography: In Vivo Imaging from Organelles to Organs. *Science (80-.)*. **335**, 1458–1462 (2012).
 200. Lengsfelder, B. *et al.* Remote photoacoustic sensing using speckle-analysis. *Sci. Rep.* **9**, 1057 (2019).
 201. Aziz, A., Medina-Sánchez, M., Claussen, J. & Schmidt, O. G. Optoacoustic detection of 3D microstructures in deep tissue-mimicking phantoms. in *Proceedings of MARSS 2019: 4th International Conference on Manipulation, Automation, and Robotics at Small Scales* 1–6 (Institute of Electrical and Electronics Engineers Inc., 2019). doi:10.1109/MARSS.2019.8860943.
 202. Deán-Ben, X. L. & Razansky, D. Portable spherical array probe for volumetric real-time optoacoustic imaging at centimeter-scale depths. *Opt. Express* **21**, 28062 (2013).
 203. Culjat, M. O., Goldenberg, D., Tewari, P. & Singh, R. S. A review of tissue substitutes for ultrasound imaging. *Ultrasound Med. Biol.* **36**, 861–873 (2010).
 204. Aziz, A., Medina-Sánchez, M., Claussen, J. & Schmidt, O. G. Real-time optoacoustic tracking of single moving micro-objects in deep tissue-mimicking phantoms. *arXiv:1907.09264* (2019) doi:10.1021/acs.nanolett.9b02869.
 205. Xie, L. *et al.* Photoacoustic Imaging-Trackable Magnetic Microswimmers for Pathogenic Bacterial Infection Treatment. *ACS Nano* **14**, 2880–2893 (2020).
 206. Park, S. *et al.* Synergy and Applications of Combined Ultrasound, Elasticity, and Photoacoustic Imaging (Invited). in *2006 IEEE Ultrasonics Symposium* 405–415 (2006). doi:10.1109/ULTSYM.2006.114.
 207. Aziz, A., Holthof, J., Meyer, S., Schmidt, O. G. & Medina-Sánchez, M. In vivo imaging of swimming micromotors using hybrid high-frequency ultrasound and photoacoustic imaging. *bioRxiv* 2020.06.15.148791 (2020) doi:10.1101/2020.06.15.148791.
 208. Yunker, B. E. *et al.* An investigation of industrial molding compounds for use in 3D ultrasound, MRI, and CT imaging phantoms. *Med. Phys.* **40**, 52905 (2013).
 209. Oliveira, P. A. *et al.* Technical report: Technique of bladder catheterization in female mice and rats for intravesical instillation in models of bladder cancer.

- Scand. J. Lab. Anim. Sci.* **36**, 5–9 (2009).
210. Hortelão, A. C., Patiño, T., Perez-Jiménez, A., Blanco, À. & Sánchez, S. Enzyme-Powered Nanobots Enhance Anticancer Drug Delivery. *Adv. Funct. Mater.* **28**, 1705086 (2018).
211. Jeong, S. *et al.* Penetration of an artificial arterial thromboembolism in a live animal using an intravascular therapeutic microrobot system. *Med. Eng. Phys.* **38**, 403–410 (2016).
212. Cai, P. *et al.* Biomechano-Interactive Materials and Interfaces. *Adv. Mater.* **30**, e1800572 (2018).
213. Hong, G. *et al.* Multifunctional in vivo vascular imaging using near-infrared II fluorescence. *Nat. Med.* **18**, 1841–6 (2012).
214. Lim, Y. T. *et al.* Selection of quantum dot wavelengths for biomedical assays and imaging. *Mol. Imaging* **2**, 50–64 (2003).
215. He, Y. *et al.* Water-Dispersed Near-Infrared-Emitting Quantum Dots of Ultrasmall Sizes for In Vitro and In Vivo Imaging. *Angew. Chemie Int. Ed.* **50**, 5695–5698 (2011).
216. Hines, M. A. & Scholes, G. D. Colloidal PbS Nanocrystals with Size-Tunable Near-Infrared Emission: Observation of Post-Synthesis Self-Narrowing of the Particle Size Distribution. *Adv. Mater.* **15**, 1844–1849 (2003).
217. Cao & Banin, U. Growth and Properties of Semiconductor Core/Shell Nanocrystals with InAs Cores. *J. Am. Chem. Soc.* **122**, 9692–9702 (2000).
218. Gui, R., Sun, J., Liu, D., Wang, Y. & Jin, H. A facile cation exchange-based aqueous synthesis of highly stable and biocompatible Ag₂S quantum dots emitting in the second near-infrared biological window. *Dalt. Trans.* **43**, 16690–16697 (2014).
219. Gu, Y.-P., Cui, R., Zhang, Z.-L., Xie, Z.-X. & Pang, D.-W. Ultrasmall near-infrared Ag₂Se quantum dots with tunable fluorescence for in vivo imaging. *J. Am. Chem. Soc.* **134**, 79–82 (2012).
220. Bourdeau, R. *et al.* Acoustic reporter genes for non-invasive imaging of microbes in mammalian hosts. *Nat. Publ. Gr.* **553**, 86–90 (2018).
221. Weber, J., Beard, P. C. & Bohndiek, S. E. Contrast agents for molecular photoacoustic imaging. *Nat. Methods* **13**, 639–650 (2016).
222. Wang, L. V. Ultrasound-Mediated Biophotonic Imaging: A Review of Acousto-Optical Tomography and Photo-Acoustic Tomography. *Dis. Markers* **19**, 478079 (2004).

223. Resink, S. G., Steenbergen, W. & Boccara, A. C. State-of-the art of acoust-optic sensing and imaging of turbid media. *J. Biomed. Opt.* **17**, 1–11 (2012).
224. Debye, P. & Sears, F. W. On the Scattering of Light by Supersonic Waves. *Proc. Natl. Acad. Sci.* **18**, 409–414 (1932).
225. Radtke, U., Zielke, R., Rademacher, H.-G., Crostack, H.-A. & Hergt, R. Application of magneto-optical method for real-time visualization of eddy currents with high spatial resolution for nondestructive testing. *Opt. Lasers Eng.* **36**, 251–268 (2001).
226. Zhou, Z.-F. & Cheng, Y.-H. Magneto-optic microscope for visually detecting subsurface defects. *Appl. Opt.* **47**, 3463–3466 (2008).
227. Cheng, Y., Deng, Y., Bai, L. & Chen, K. Enhanced Laser-Based Magneto-Optic Imaging System for Nondestructive Evaluation Applications. *IEEE Trans. Instrum. Meas.* **62**, 1192–1198 (2013).
228. Vellekoop, I. M. Feedback-based wavefront shaping. *Opt. Express* **23**, 12189 (2015).
229. Park, J. H., Yu, Z., Lee, K. R., Lai, P. & Park, Y. K. Perspective: Wavefront shaping techniques for controlling multiple light scattering in biological tissues: Toward in vivo applications. *APL Photonics* **3**, 100901 (2018).
230. Ahn, C. *et al.* Overcoming the penetration depth limit in optical microscopy: Adaptive optics and wavefront shaping. *J. Innov. Opt. Health Sci.* **12**, 1–18 (2019).
231. Horstmeyer, R., Ruan, H. & Yang, C. Guidestar-assisted wavefront-shaping methods for focusing light into biological tissue. *Nat. Photonics* **9**, 563–571 (2015).
232. Mosk, A. P., Lagendijk, A., Leroosey, G. & Fink, M. Controlling waves in space and time for imaging and focusing in complex media. *Nat. Photonics* **6**, 283–292 (2012).
233. Vellekoop, I. M., Cui, M. & Yang, C. Digital optical phase conjugation of fluorescence in turbid tissue. *Appl. Phys. Lett.* **101**, 1–5 (2012).
234. Papadopoulos, I. N., Jouhanneau, J. S., Poulet, J. F. A. & Judkewitz, B. Scattering compensation by focus scanning holographic aberration probing (F-SHARP). *Nat. Photonics* **11**, 116–123 (2017).
235. Wang, Y. M., Judkewitz, B., Dimarzio, C. A. & Yang, C. Deep-tissue focal fluorescence imaging with digitally time-reversed ultrasound-encoded light. *Nat. Commun.* **3**, 928 (2012).
236. Judkewitz, B., Wang, Y. M., Horstmeyer, R., Mathy, A. & Yang, C. Speckle-scale focusing in the diffusive regime with time reversal of variance-encoded light (TROVE). *Nat. Photonics* **7**, 300–305 (2013).
237. Kong, L. & Cui, M. In vivo neuroimaging through the highly scattering tissue via

- iterative multi-photon adaptive compensation technique. *Opt. Express* **23**, 6145 (2015).
238. Osnabrugge, G., Amitonova, L. V. & Vellekoop, I. M. Blind focusing through strongly scattering media using wavefront shaping with nonlinear feedback. *Opt. Express* **27**, 11673 (2019).
239. Yoon, J., Lee, K., Park, J. & Park, Y. Measuring optical transmission matrices by wavefront shaping. *Opt. Express* **23**, 10158 (2015).
240. Conkey, D. B., Caravaca-Aguirre, A. M. & Piestun, R. High-speed scattering medium characterization with application to focusing light through turbid media. *Opt. Express* **20**, 1733 (2012).
241. Podaru, G. V., Chikan, V. & Prakash, P. Magnetic Field Induced Ultrasound from Colloidal Superparamagnetic Nanoparticles. *J. Phys. Chem. C* **120**, 2386–2391 (2016).
242. Dong, M. *et al.* 3D-Printed Soft Magnetolectric Microswimmers for Delivery and Differentiation of Neuron-Like Cells. *Adv. Funct. Mater.* **n/a**, 1910323 (2020).

9 APPENDIX

List of Figures

Figure 1.1. Opportunities and challenges of MNRs in their biomedical applications...	6
Figure 1.2. Medical MNRs swimming in living organism.....	8
Figure 1.3. An overview of most widespread biomedical imaging techniques.....	10
Figure 2.1. Basic principle of optical imaging techniques; a) Fluorescence	16
Figure 2.2: Light-tissue interaction resulting from incident light (orange).....	20
Figure 2.3. Schematic of Rayleigh scattering and Mie scattering, where	22
Figure 2.4: The basic principle of photoacoustic imaging. When an absorber	24
Figure 2.5: Basic principle of US imaging.....	27
Figure 3.1. 3D laser writing with two-photon absorption.....	31
Figure 3.2. Fabrication process of reflective micromotors	32
Figure 3.3. a) Bright-field microscopy image of monolayer of metal	33
Figure 3.4. a) SEM images of 3D printed microtubes before functionalization.....	34
Figure 3.5. a) Absorption spectrum of water, agarose and PDMS-glycerol.....	35
Figure 3.6. <i>Ex vivo</i> chicken breast tissue platform for different imaging systems	36
Figure 3.7. <i>Ex vivo</i> mice skull tissues preserved in agarose gel.....	37
Figure 3.8: a) Microfluidic channel platform b) Schematic of a PDMS	38
Figure 3.9. a) The magnetic field gradient was measured using Hall sensor.....	41
Figure 4.1. Concept of the reflective micromotor fabricated by half-coating	43
Figure 4.2. a) Schematic of reflective micromotor at different angles.....	44
Figure 4.3. a) Bright-field microscopy image of monolayer of metal coated	45
Figure 4.4. a) Schematic of IR imaging setup. b) Flow diagram.....	46
Figure 4.5. Time-lapse images of a single micromotor (100 μm in diameter)	46
Figure 4.6: Tracking of a single micromotor beneath varying thicknesses.....	48
Figure 4.7. Micromotors beneath different phantom thicknesses.....	49
Figure 4.8. <i>Ex vivo</i> tracking of single micromotors under mice skull tissues.....	51
Figure 4.9. a) Schematic of a PDMS microchannel and movement.....	52
Figure 4.10. a) Bright-field, control, and fluorescence images.....	53
Figure 5.1. Absorbance spectrum of agarose phantom (blue curve)	56
Figure 5.2. a) SEM images of an array of 3D printed micromotors.....	57
Figure 5.3. PA signal intensity of the AuNRs-coated micromotors.....	58
Figure 5.4. PA imaging system, illustrating the position of the phantom.....	59

Figure 5.5. Principle of PAI. The micromotors within the phantom	60
Figure 5.6. PA imaging of swarm of 25 μm long micromotors	61
Figure 5.7. a) Schematic representation of phantom preparation.	61
Figure 5.8. PA signal of fully embedded micromotors (top)	62
Figure 5.9. Comparison of the measured distance between two micromotors	63
Figure 5.10. a) Schematic of 3D hand-held detector for real time tracking.....	65
Figure 5.11. a) Tracking of micromotors labelled with AuNRs.....	66
Figure 6.1. Schematic showing the working principle of the employed.....	68
Figure 6.2. a) Optical and SEM images of spherical micromotors.	69
Figure 6.3. Tracking of single micromotors in phantom a.....	70
Figure 6.4. a) Micromotors inserted in IPU tubing which is then sandwiched	71
Figure 6.5. <i>In vivo</i> HFUS and PA imaging of micromotor	73
Figure 6.6: Hybrid HFUS and PA time-lapse images of swimming.....	73
Figure 6.7. A swarm of swimming micromotors under the actuation	74
Figure 6.8. HFUS and PA imaging of micromotors moving in the uterus.....	75
Figure 6.9. a) Time-lapse images of single moving micromotors.....	75
Figure 6.10. 3D multiplexing <i>in vivo</i> : a) Injection of micromotors.	77
Figure 6.11. Application scenario of micromotors for drug delivery.....	79

List of Tables

Table 1. Comparison of scattering medium in tissues (phantoms and skull).....	50
Table 2: PA imaging parameters for visualization of micromotors	59
Table 3. Imaging parameters for Hybrid HFUS and PA system	68
Table 4. Summary of all imaging techniques for medical tracking of MNRs.....	81

Abbreviations

MNRs	Micro- and nanorobots
FoV	Field of view
NPs	Nanoparticles
PAI	Photoacoustic imaging
US	Ultrasound
MRI	Magnetic Resonance Imaging
MPI	Magnetic Particle Imaging
RI	Reflection-based Imaging
FI	Fluorescence Imaging
PET	Positron Emission Tomography
SPECT	Single Photon Emission Computed Tomography
CT	Computed Tomography
MMUS	Magnetomotive Ultrasound
OCT	Optical Coherence Tomography
ULM	Ultrasound Localization Microscopy
TPA	Two-photon absorption
PRF	Pulse Repetition Frequency
MFP	Mean Free Path
TMFP	Transport Mean Free Path
SNR	Signal to Noise Ratio
NIR	Near infrared
NIR-I	First Biological Window (700-950)
NIR-II	Second Biological Window (1000-1400 nm)
IR	Infrared
QDs	Quantum Dots
ABFs	Artificial Bacterial Flagella
AuNRs	Gold Nanorods
PDA	Polydopamine
HFUS and PA	High-frequency Ultrasound and Photoacoustics
B-mode	Brightness Mode
SLMs	Spatial Light Modulators
QRE	Quadrupole Relaxation Enhancement
AOI	Acousto-Optic Imaging
MOI	Magneto-Optic Imaging
MAT	Magneto-Acoustic Imaging

List of Publications

Scientific Journal Publications

1. **A. Aziz**, M. Medina-Sánchez, J. Claussen, and O. G. Schmidt, “Real-Time Optoacoustic Tracking of Single Moving Micro-objects in Deep Phantom and Ex Vivo Tissues” **Nano Lett.**, 19 (9), 6612–6620, 2019.
2. **A. Aziz**, M. Medina-Sánchez, N. Koukourakis, J. Wang, R. Kuschmierz, H. Radner, J. W. Czarske and O. G. Schmidt, “Real-time IR tracking of single reflective micromotors through scattering tissues” **Adv. Funct. Mater.**, 29 (51) 2019.
3. V. Magdanz, I. S. M. Khalil, J. Simmchen, G. P. Furtado, S. Mohanty, J. Gebauer, H. Xu, A. Klingner, **A. Aziz**, M. Medina-Sánchez, O. G. Schmidt, S. Misra, “IRONsperm: Sperm-templated soft magnetic microrobots” **Sci. Adv.** 6, eaba5855 (2020).
4. **A. Aziz**, S. Pane, V. Iacovacci, N. Koukourakis, J. W. Czarske, A. Menciassi, M. Medina-Sánchez and O. G. Schmidt, “Medical Imaging of Microrobots: Toward In Vivo Applications” **ACS Nano**, 14 (9), 10865-10893, 2020.
5. **A. Aziz**, J. Holthof, S. Meyer, O. G. Schmidt, M. Medina-Sánchez, “In Vivo Imaging of Swimming Micromotors Using Hybrid High-Frequency Ultrasound and Photoacoustic Imaging” **bioRxiv**, 2020. doi: 10.1101/2020.06.15.148791.

Conference Proceedings

- **A. Aziz**, M. Medina-Sánchez, J. Claussen, and O. G. Schmidt, “Optoacoustic detection of 3D microstructures in deep tissue-mimicking phantoms” Int. Conf. Manip. Autom. Robot. Small Scales (MARSS), July 1-5, 2019, Helsinki/Finland, 2019.

Conference Talks

- **A. Aziz**, M. Medina-Sánchez, J. Claussen, and O. G. Schmidt, “Multispectral optoacoustic tomography (MSOT) of 3D microstructures” Int. Conf. Manip. Autom. Robot. Small Scales (MARSS), July 1-5, 2019, Helsinki/Finland, 2019.

Poster Contributions

- H. Xu, **A. Aziz**, M. Medina-Sánchez, J. Claussen, and O. G. Schmidt, “Steps further to the clinic: human based materials and in vivo real-time tracking” Proceedings of the ICMNM 2019 International Conference on Micro/Nanomachines (**ICMNM 2019**), August 25-28, 2019, Harbin, China.
- **A. Aziz**, F. Striggow, Raffael Herzer, L. Schwarz, M. Medina-Sánchez, J. Claussen, and O. G. Schmidt, “Sensing and actuation on cell-material interfaces in biohybrid microsystems: Engineered cell differentiation, motorization, and imaging” 5th condensed matter IFW Summer School, **September 25-27, 2019, Szczecin, Poland.**

Acknowledgements

I would like to thank a number of people for their support in many ways during four years of my PhD. First of all, Prof. Dr. Oliver G. Schmidt for giving me this exciting PhD topic and letting me explore the imaging field and his continuously valuable feedback and guidance. I thank Prof. Dr. Jürgen W. Czarske (TU Dresden) for agreeing to be the second supervisor of my PhD thesis. I am grateful to Dr. Mariana Medina-Sánchez who gave me full support and guidance during the time of my PhD with her mentorship and her kind attitude. She was always there whenever I had some issues in experiments and she always gave nice ideas and suggestions to solve many complicated problems.

I would also like to thank Dr. Daniil Karnaushenko, Dr. Libo Ma and Dr. Jiawei Wang for their valuable suggestions, guidance and help including preliminary experiments in their lab during the first year of my PhD. I thank Dr. Dmitriy Karnaushenko for his simulations, Dr. Stefan Baunack for his great help in capturing SEM images and also Dr. Volker Neu for doing magnetization measurements. I am thankful to Dr. Nektarios Koukourakis (TU Dresden) for the fruitful collaboration and being so nice and helpful in accomplishing part of my PhD and providing many nice suggestions. Also, Hannes Radner and Robert Kuschmierz for helping in algorithm implementation. I am also grateful to Prof. Sarthak Misra and Dr. Islam Khalil (University of Twente), Visualsonics, Amsterdam (Joost Holthof, Sandra Meyer) and iThera Medical, Munich (Jing Claussen and Neal Burton) for their kind collaboration.

I would also like to thank my former and present group members. Former members are: Dr. Veronika Magdanz, Sonja Weiz, Lukas Schwarz and Yan Chen. My current group members are: Haifeng Xu, Raffael Herzer, Franziska Hebenstreit, Aleksandr Egunov, Friedrich Striggow, Farzin Akbar, Boris Rivkin, Raphael Doineau, Fatemeh Rajabasadi, David Castellanos Robles, Cornelia Geringswald, Eashika Ghosh and Yara Tarek Mahmood Abdelaal for simply being great and helpful. Franziska Hebenstreit for bringing cow blood from slaughter house and taking good care of the labs. Many thanks to our cleanroom and technical staff including Ronny Engelhardt, Sandra Nestler, Martin Bauer and Carol Schmidt for providing excellent assistance with deposition machines and clean room equipment.

Last but not the least I thank my family for supporting me in my work. My Mother for always encouraging me to continue and my late Father for his appreciation. I am grateful for my wife for her continuous support and sacrifices during the last years. I thank everyone that has stirred my passion for this research.

Selbstständigkeitserklärung

Ich erkläre, dass ich die vorliegende Arbeit selbstständig und nur unter Verwendung der angegebenen Literatur und Hilfsmittel angefertigt habe. Ich erkläre, nicht bereits früher oder gleichzeitig bei anderen Hochschulen oder an dieser Universität ein Promotionsverfahren beantragt zu haben.

Ort, Datum

Unterschrift

Curriculum Vitae

Personal Information

Name : Aziz
 First Name : Azaam
 Date of Birth : December 10, 1988
 Place of Birth : Gujrat, Pakistan
 Nationality: Pakistani

Education

September 2016 - present

PhD candidate

Leibniz-IFW Dresden, Institute for Integrative Nanosciences and Technische Universität Chemnitz, Chemnitz, Germany

Supervisors: Prof. Dr. Oliver G. Schmidt and Dr. Mariana Medina-Sánchez

2012 – 2015

Master of Science (M.Sc.)

SciTec, University of applied sciences, Jena, Germany

2006 – 2010

Bachelor of Science (B.Sc.)

Department of Physics, University of the Punjab, Lahore, Pakistan

Experience

September 2016 - present

Researcher at Leibniz-IFW Dresden, Institute for Integrative Nanosciences and Technische Universität Chemnitz, Chemnitz, Germany

2015

Master Thesis at Max-Planck-Institute for Intelligent Systems (IS) Stuttgart, Germany

2014

Research Internship at Institute of Material Sciences, University of Stuttgart, Germany

2009-2011

Physics Tutor (Grade 11-12th) at Al-Hamd School of Sciences, Lahore, Pakistan